

Fermi Surface Studies
on the Organic Superconductor
 κ -(BEDT-TTF)₂Cu[N(CN)₂]Br and
on the Alkaline Earth Subnitride NaBa₃N
by means of Magneto-Quantum
Oscillations

Dissertation
zur Erlangung des akademischen Grades eines
Doktors der Naturwissenschaften
an der Universität Konstanz
Fachbereich Physik

vorgelegt von

Herbert Dieter Weiß
geboren in München

Tag der mündlichen Prüfung: 30.01.2001

Referent: Prof. Dr. P. Wyder (Grenoble)

Referent: Prof. Dr. G. Schatz

Contents

1	Introduction	1
2	Theory of Magneto-Quantum Oscillations	5
2.1	Onsager Relation	5
2.2	de Haas-van Alphen Effect	7
2.2.1	Damping Factors	8
2.2.2	Magnetic Breakdown	11
2.3	Shubnikov-de Haas Effect	12
2.4	Magneto-Quantum Oscillations in 2D Electronic Systems	14
3	Experiment	16
3.1	High Steady Magnetic Fields	16
3.2	Cryogenic System	17
3.3	Temperature Measurement and Control	19
3.4	Detection Methods	19
3.4.1	Torque Method	20
3.4.2	Four-Probe Technique	22
3.4.3	Simultaneous Torque and Transport Measurement	24
3.5	Pressure Cell	24
4	Magneto-Quantum Oscillations	
	in κ-(BEDT-TTF)₂Cu[N(CN)₂]Br	27
4.1	The Organic Superconductor κ -(BEDT-TTF) ₂ Cu[N(CN) ₂]Br	27
4.1.1	Synthesis	30
4.1.2	Crystal Structure	31
4.1.3	Electronic Structure	34
4.2	de Haas-van Alphen Measurements	37
4.2.1	dHvA Oscillation Frequencies	37
4.2.2	Angular Dependence of dHvA Oscillation Frequencies - Beating Effect	41
4.2.3	Effective Cyclotron Masses	45
4.2.4	Angular Dependence of the dHvA Oscillation Amplitudes	47
4.2.5	Dingle Temperature	50
4.3	Shubnikov-de Haas Measurements	52

4.3.1	SdH Oscillation Frequencies	52
4.3.2	Effective Cyclotron Masses	55
4.3.3	Angular Dependences of Electronic Properties	55
4.4	Simultaneous de Haas-van Alphen and Shubnikov-de Haas Measurements	56
4.4.1	Relative Oscillation Amplitude $\Delta R_\alpha/\Delta R_\beta$	56
4.4.2	Beating Effect	60
4.5	Thermal History	65
4.6	Shubnikov-de Haas Measurements under Pressure	69
4.6.1	Changes with Pressure - General Features	69
4.6.2	SdH Oscillation Frequencies	71
4.6.3	Pressure Dependences	78
4.6.4	Beating Effect	88
5	de Haas-van Alphen Oscillations in NaBa₃N	91
5.1	The Sample	91
5.1.1	The Alkaline Earth Metal Subnitride NaBa ₃ N	91
5.1.2	Synthesis and Crystal Structure	93
5.1.3	Electronic Structure	94
5.2	Experimental Results and Discussion	98
5.2.1	dHvA Oscillation Frequencies - Fermi Surface Topology	98
5.2.2	Effective Cyclotron Masses	105
5.2.3	Dingle Temperature	106
6	Summary	108
	Zusammenfassung	111
	Bibliography	115

Chapter 1

Introduction

The fundamental Pauli exclusion principle states that two elementary particles of half-integral spin cannot simultaneously occupy the same quantum or energy state of a system. As a consequence, the allowed energy states of electrons in a metal are distributed according to the Fermi function. At absolute zero temperature, this distribution function ends abruptly at the highest state, at the Fermi energy. In momentum space this characteristic energy gives a surface of highest occupied levels, the so-called Fermi surface (FS).

The FS is of tremendous importance in solid-state physics. Besides characterizing the ground state of a metallic system and determining its transport, magnetic, and optical properties, a wealth of other phenomena are thought to be FS-driven. The principal reason for its importance lies in the fact that it is only those electrons at the FS that can respond to external fields by absorbing energy in small quantities. Those electrons deep in the ‘Fermi sea’ are prevented from doing so as the final states required are already occupied.

In general, the FS of a metallic system is not a simple sphere, as in the case of free electrons, and the determination of its often complicated topology remains an important challenge for solid-state physicists. In systems where more than one energy band crosses the Fermi energy, the FS consists of several sheets owing to each of these bands.

For experimental Fermi surface studies information can be derived from various kinds of measurements such as electron-positron annihilation, angle-resolved photoemission, and cyclotron resonance.

From the very first attempts to get information about the FS topology and associated electronic properties, those methods based on the observation of magneto-quantum oscillations played an outstanding role. The discovery of magneto-quantum oscillations in the electrical resistance and magnetization of bismuth, named after their authors Shubnikov-de Haas (SdH) effect [1] and de Haas-van Alphen (dHvA) effect [2], respectively, dates back to the year 1930. By a rather remarkable coincidence, Landau had predicted an oscillatory behavior of the magnetization of a metal in a varying magnetic field due to the orbital quantization of the electron motion one or two months before [3], but the relevance of this theoretical prediction to the experimental observation had not been noticed. It took another five years

until both findings were finally related to each other. Moreover, the importance of this effect as an invaluable tool for FS investigations was not realized before 1950 when Lifshitz [4] and Onsager [5] pointed out that the quantum oscillation frequency of the dHvA effect and of related phenomena is directly proportional to the extremal cross-sectional area of the FS. Soon afterwards, a rather comprehensive theory was worked out involving not only the frequency but also the amplitude and phase of magneto-quantum oscillations of the magnetization of an isotropic three-dimensional system [6].

Owing to significant technological advances, the basic requirements for the observation of magnetic quantum effects, namely the production of high magnetic fields and low temperatures, as well as the growth of pure and more perfect single crystals, have been greatly improved since the first magneto-quantum oscillation experiments. Hence, various effects similar to the SdH and dHvA effects have been found and the techniques for their detection have been refined. By and large, properties of a metal that oscillate in a varying magnetic field can be categorized into thermodynamic and non-equilibrium properties. The former comprise magnetic (such as the magnetization on which the dHvA effect is based on), thermal, and mechanical properties, whereas the latter include transport (such as the electrical conductivity which exhibits the SdH effect), optical, and acoustic properties.¹ However, already at an early stage of research in this field, it became clear that of all the methods associated with magneto-quantum oscillations that based on the dHvA effect would be the most versatile and accurate tool for the determination of FS's [7]. While the first dHvA experiment [2] employed the mechanical force acting on a magnetic moment in an inhomogeneous magnetic field, more convenient techniques are available today. Two distinct principles, dynamic and static, are used. Dynamical methods make the magnetization vary with time and examine the thereby induced electromagnetic field in a pick-up coil. Therefore, the sample may be either subjected to a steadily varying pulsed magnetic field or to a steady magnetic field along with a superimposed small periodically varying field. The latter method is more advantageous since it allows for a phase sensitive detection of the magnetization. However, dynamical methods involve the problem of eddy current induction and are poorly favorable to the detection of low magneto-quantum oscillation frequencies. The most widely used technique among the static ones is the torque method which measures the torque acting onto a magnetic moment subject to a magnetic field. Devices used for the torque technique can be generally designed as very simple and robust constructions that allow for rather high resolution measurements. This method thus successfully rivals the well established field modulation method.

It was not without reason that magneto-quantum oscillations had been first discovered in the electrical resistance [1]. Electrical transport measurements had always been one of the most commonly used tools for the characterization of conducting materials. Although the electrical resistance involves non-equilibrium phenomena and thus requires far more complicated considerations for a detailed theoretical

¹It should be mentioned that several other magneto-oscillatory effects exist whose periodicities are not directly linked with the FS cross-sectional area.

description than thermodynamic properties, it is still greatly appreciated for the observation of magneto-quantum oscillations for it is very easily accessible experimentally.

In the present work, the dHvA and the SdH effects are employed for the investigation of two different systems that are both characterized by peculiar crystal structures: The first part of this thesis is devoted to the study of the organic superconductor κ -(BEDT-TTF)₂Cu[N(CN)₂]Br² which consists of a layered structure that leads to a strongly two-dimensional character of conduction. Subject of the second part is the earth alkaline subnitride NaBa₃N which is believed to exhibit a novel chain structure where quasi-one-dimensional tubes, strongly held together by ionic bonding, are embedded into a metallic matrix. This unusual structure leads to a confinement of the conduction electrons to the atomic scale regions between the tubes.

The focus of the study of κ -(BEDT-TTF)₂Cu[N(CN)₂]Br is not only the exact characterization of its FS and electronic ground state but also the investigation of its electronic properties under pressure. The latter objective is particularly intriguing for organic superconductors since they exhibit a wealth of ground states ranging from metallic to superconducting and antiferromagnetic insulating. In contrast to high- T_c superconductors, it is not the change in the degree of doping but the variation of pressure which drives the system through different states. Of particular note is the direct vicinity of the superconducting to the antiferromagnetic phase. Within the BEDT-TTF family, the ground state of the κ -(BEDT-TTF)₂Cu[N(CN)₂]Br compound lies closest to the boundary between these two phases and is therefore a promising candidate for the study of the interplay between structural and electronic properties in this region of the pressure dependent phase diagram. Detailed information about the ground state near the metal/superconductor-insulator transition is especially desirable to shed light onto the coupling mechanism which drives the superconductivity in quasi-two-dimensional organic superconductors.

Organic superconductors in the metallic state are generally ‘bad metals’ since they exhibit charge carrier densities much lower than those of conventional metals. Nevertheless, the highly symmetric shape of the FS characteristic for two-dimensional electron systems as well as the usually very small number of different FS sheets is often much in favor of the successful observation of magneto-quantum oscillations. Due to the strongly anisotropic electronic structure, however, these systems are beyond the absolute validity of the standard theory available for the dHvA effect. None the less, in many cases this theory gives a sufficient description of the experimental observations. Most magneto-quantum oscillation studies on organic conductors have been carried out using the SdH effect, in the assumption that it should in principle reveal the same behavior as the dHvA effect. A special interest of this thesis is devoted to the comparison of the results obtained by thermodynamic (dHvA) and transport (SdH) measurements.

The investigation of the earth alkaline subnitride NaBa₃N aims mainly at the classical target of FS determination. This work represents the first experimental

²BEDT-TTF stands for bis-(ethylenedithio)-tetrathiafulvalene, C₁₀H₈S₈, and is often also abbreviated as ET.

attempt of the characterization of the electronic structure of this compound and proceeds directly along with theoretical band structure calculations. To date, the NaBa_3N is the only compound among the class of metals that are believed to be interspersed by regions repulsive to conduction electrons which may be suitably prepared for magneto-quantum oscillation experiments. It is thus challenging to search for this effect in this material, also with the aim to obtain some hints that would allow to corroborate the present view of the peculiar bonding situation.

Chapter 2

Theory of Magneto-Quantum Oscillations

In the first part of this chapter, the mechanism which underlies most magneto-oscillatory effects is briefly outlined using the Bohr-Sommerfeld quantization condition for non-interacting Bloch electrons, as it was first done by Onsager [5]. The subsequent sections then provide the theory for the quantitative analysis of magneto-quantum oscillations in the magnetization [6, 8, 9], i.e., the de Haas-van Alphen (dHvA) effect, and in the electrical conductivity [10], i.e., the Shubnikov-de Haas (SdH) effect. Since they are both relatively easily accessible experimentally, these effects are the bases of the most powerful techniques for the observation of magneto-quantum oscillations.

2.1 Onsager Relation

The motion of free electrons in the presence of a magnetic field \mathbf{B} is determined by the Lorentz force. Considering the electrons to be independent particles it is described by the basic equation:

$$\hbar \cdot \frac{d\mathbf{k}}{dt} = -e(\mathbf{v} \times \mathbf{B}). \quad (2.1)$$

where $-e$ is the elementary charge, $\hbar\mathbf{k}$ the momentum and \mathbf{v} the group velocity of an electron wave packet. By integrating Eq. (2.1) with respect to time we obtain a direct relation between the trajectory in the real space and that in the momentum space (hereafter referred to as \mathbf{k} -space),

$$\hbar(\mathbf{k} - \mathbf{k}_0) = -e(\mathbf{r} - \mathbf{r}_0) \times \mathbf{B}. \quad (2.2)$$

For closed electron trajectories, the Bohr-Sommerfeld quantization rule can be applied:

$$\oint \mathbf{p} \cdot d\mathbf{q} = (n + \gamma)2\pi\hbar, \quad (2.3)$$

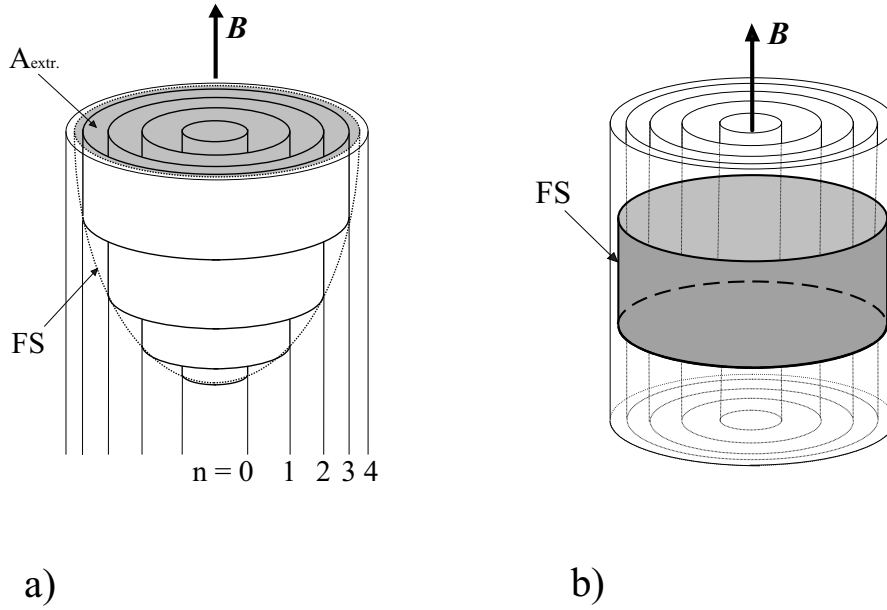


Figure 2.1: Fermi surface and Landau tubes for the three-dimensional (a) and two-dimensional (b) cases.

where \mathbf{p} and \mathbf{q} are canonically conjugate momentum and position variables, n is an integer and $\gamma = \gamma(n)$ is a slowly varying phase function known to be $1/2$ for free-electron orbits. Eq. (2.3) can be transformed so as to give the magnetic flux $\Phi = \mathbf{B}a(\mathbf{r})$ through the area $a(\mathbf{r})$ enclosed by the real space orbit:

$$\Phi = (n + \gamma)2\pi\hbar/e. \quad (2.4)$$

Employing Eq. (2.2) we come to the *Onsager relation* which gives the corresponding area in \mathbf{k} -space,

$$a_{kn} = (n + \gamma) \frac{2\pi eB}{\hbar}. \quad (2.5)$$

Hence, the motion is quantized according to a quantization of the area enclosed in the projection of the electron orbit onto the plane perpendicular to the magnetic field. The motion in k_{\parallel} direction, i.e. parallel to \mathbf{B} , is not affected. The permitted electronic states, uniformly distributed in the zero field case, thus become degenerate in field and condense onto a series of so-called Landau tubes with energies ϵ_n (Fig. 2.1). Each Landau tube can accommodate as many electron states as would lie within the annular cross-sectional area $\Delta A = 2\pi eB/\hbar$ between neighboring Landau levels at zero magnetic field. ΔA and a_n both grow with increasing magnetic field, that leads to an increase of the degeneracy of each Landau level ϵ_n and hence to an increase of the free energy of the whole system. As soon as the outermost Landau tube overlaps the boundary of the extremal FS cross-sectional area A_{extr} perpendicular to \mathbf{B} , the free energy has reached its maximum and a singularity of the density of states at the Fermi energy occurs. The further increase

of the magnetic field results in a redistribution of the electrons down to the next lower Landau level ($n-1$) lying within the FS and by that entails a lowering of the free energy. With growing in its cross-sectional area, the Landau tube ($n-1$) in turn undergoes the same process as the tube n . For large n the difference between the fields at which the n -th and the $(n-1)$ -th Landau tubes cross the boundary of the extremal FS cross-section is obtained according to the relation (2.5),

$$\frac{1}{B} - \frac{1}{B_{n-1}} = \Delta \frac{1}{B} = \frac{2\pi e}{\hbar A_{extr}}. \quad (2.6)$$

The crossing occurs periodically in the inverse magnetic field scale giving rise to an oscillatory behavior of the free energy as well as of the density of states at the Fermi energy. A Fourier analysis gives the oscillation frequency in units of magnetic induction,

$$F = \frac{1}{\Delta \frac{1}{B}} = \frac{\hbar}{2\pi e} A_{extr}. \quad (2.7)$$

This result represents a remarkably simple relation between the frequency which is observed in quantum oscillation experiments and the extremal cross-sectional area of the FS in a plane normal to the magnetic field.

Since Eq. (2.7) is valid for any magnetic field direction, all extremal areas of an arbitrary FS can in principle be mapped out. Yet, as the oscillation frequency provides information only about FS *cross-sectional* areas, the exact determination of the FS shape by investigating the frequency spectrum as a function of the crystallographic orientation is not unambiguous. It is rather an empirical procedure, based on the preliminary information from band structure calculations or other appropriate experimental techniques of what kind of FS might be expected.

2.2 de Haas-van Alphen Effect

In 1956, Lifshitz and Kosevich [6] developed a quantitative description of the oscillating magnetization in a varying magnetic field. This theory is still the basis for the analysis of the dHvA effect. The main result, the so-called Lifshitz-Kosevich (LK) formula, is obtained by calculating the gradient of the thermodynamic potential, Ω , with respect to the magnetic field, keeping the chemical potential, μ , constant: $\mathbf{M} = -(\nabla_{\mathbf{B}}\Omega)_{\mu}$. For a system which obeys the Fermi-Dirac statistic, Ω is given by a summation over the possible energy states,

$$\Omega = -k_B T \sum_{\epsilon} \ln \left[1 + \exp \left(\frac{\mu - \epsilon}{k_B T} \right) \right], \quad (2.8)$$

where k_B is the Boltzmann constant. Regarding the contribution of only a two-dimensional slab in \mathbf{k} -space normal to the magnetic field and taking into account the degeneracy of each Landau level, the summation can be carried out by use of

the Poisson summation formula [11] or the Euler-Maclaurin formula [3]. The subsequent integration over k_{\parallel} , i.e., the \mathbf{k} component parallel to \mathbf{B} , effectively considers only the fraction of the extremal cross-sectional areas (i.e., enclosed by maximum or minimum orbits) of the FS. These orbits contribute coherently, whereas the remaining orbits cancel each other out owing to destructive interference. Taking into account the corrections for finite temperature (represented by the correction factor R_T), electron scattering (R_D), and the effect of the electron spin (R_S), we find the contribution of one extremal area to the oscillatory part of the magnetization parallel ($\widetilde{M}_{\parallel}$) and perpendicular (\widetilde{M}_{\perp}) to the magnetic field:

$$\widetilde{M}_{\parallel} = -\sqrt{\frac{e^5}{2\pi^5\hbar}} \frac{F\sqrt{B}}{m^* \sqrt{|A''_{extr}|}} \sum_{p=1}^{\infty} \frac{R_T(p) \cdot R_D(p) \cdot R_S(p)}{p^{3/2}} \sin \left[2\pi p \left(\frac{F}{B} - \gamma \right) \pm \frac{\pi}{4} \right] \quad (2.9)$$

$$\widetilde{M}_{\perp} = -\frac{1}{F} \frac{dF}{d\theta} \widetilde{M}_{\parallel} \quad (2.10)$$

This result is known as the Lifshitz-Kosevich formula for the dHvA effect. The summation is carried out over all harmonics, p , in the Fourier spectrum of the oscillations. In the prefactors we have introduced m^* and A''_{extr} . The former is the effective cyclotron mass which, in the absence of carrier-carrier and carrier-phonon interactions,¹ equals the band structure effective mass, $m_{band} = \hbar^2/2\pi \cdot (\partial A/\partial \epsilon)_{k_{\parallel}=k_0}$. A''_{extr} represents the local curvature of the FS at an extremal cross-sectional area perpendicular to the magnetic field direction, $A''_{extr} = \left(\partial^2 A_{extr}/\partial k_{\parallel}^2 \right)_{k_{\parallel}=k_0}$. The phase factor $\pi/4$ takes account of whether the extremal cross-sectional FS area is a maximum or minimum. In the case of a maximum the factor is negative whereas for a minimum it is positive. In polyvalent metals the Fermi surface generally exhibits more than one extremal cross-sectional area. In that case, the total oscillatory part of the magnetization is simply the sum over all contributions, each of them having the form (2.9)/(2.10), but with different parameters F , m^* , A''_{extr} , and R_T , R_D , R_S .

2.2.1 Damping Factors

The factors R_T , R_D , and R_S stand for the main effects that may reduce the magneto-quantum oscillation amplitude. They represent the actual virtue of the LK formula since they can be treated independently and thus allow to extract electronic properties characteristic for the investigated system as fitting parameters of the temperature-, field-, and angular dependence of the oscillation amplitude.

¹The LK formula is calculated for independent quasi-particles and does not take account of many-body interactions. Yet, if the deviations from the free electron case are not too strong, it retains its validity, provided that the parameters entering the formula are appropriately modified or renormalized [12].

Effect of Finite Temperature, R_T

The energy states that are occupied by electrons depend on the density of states as well as on the Fermi distribution function. In contrast to the damping effects discussed below, a finite temperature does not affect the density of states but the Fermi distribution function. At finite temperature, the distribution of the occupied states at the Fermi level ϵ_F is no longer step-like, but smeared out over the energy range $k_B T$. Hence, the redistribution of electrons on the outermost Landau tube which passes through the Fermi surface does not take place at a sharply defined field. This results in a spread of the oscillation frequency that can be treated as a phase smearing. After a Fourier transform of the distribution function of this phase smearing is performed (see e.g. [9]), the amplitude reduction factor R_T for the p -th harmonic is obtained as

$$R_T = \frac{\alpha p \frac{m^*}{m_e} T / B}{\sinh(\alpha p \frac{m^*}{m_e} T / B)}, \quad (2.11)$$

with the constant $\alpha = 2\pi^2 k_B m_e / \hbar e \simeq 14.69$ T/K.

With the present reduction factor introduced into the LK formula the effective cyclotron mass, m^* , of the electrons on the extremal orbit can be determined by fitting the measured temperature dependence of the oscillation amplitude $A(T)$, where m^* acts as fitting parameter. It has to be noted that the obtained effective mass involves an average of the dispersion relation along the periodic orbit.

Dingle Factor R_D

Lattice distortions and impurities lead to a finite relaxation time, τ , of the conduction electrons and, owing to the uncertainty principle, to a broadening of the otherwise δ -shaped Landau levels. If τ can be assumed as independent of the energy, the effect of this broadening is equivalent to that of a variation of the Fermi energy around its zero temperature value. This in turn can be regarded as a phase smearing which further reduces the oscillation amplitude. Since a finite relaxation time has almost the same effect as a rise of temperature, it is obvious to introduce a temperature which would entail a damping equivalent to that caused by the finite relaxation time:

$$T_D = \frac{\hbar}{2\pi k_B \tau}. \quad (2.12)$$

T_D is the so-called Dingle temperature which is proportional to the electron scattering rate and therefore an indicator for the purity of the sample. The relaxation time τ is the orbital average of the mean lifetime over the extremal orbit on the Fermi surface [13]. A Fourier transform of the distribution function of the phase smearing which is assumed to be sufficiently described by the Lorentzian distribu-

tion function (see e.g. [9]) gives the Dingle reduction factor for the p -th harmonic,

$$R_D = \exp\left(-\alpha p \frac{m^* T_D}{m_e B}\right). \quad (2.13)$$

Provided that the effective cyclotron mass is known for a certain orbit,² the corresponding Dingle temperature can be extracted from the magnetic field dependence of the dHvA oscillation amplitude. This is either done by directly fitting the experimentally obtained magnetization oscillation amplitude, $A(B)$, to the LK formula or by a plot of $\ln\left[A\sqrt{B} \sinh(\alpha p T m^*/m_e B)\right]$ against $1/B$ (commonly called Dingle plot), where A needs not to be measured absolutely. If the field dependence of the amplitude is determined exclusively by a finite relaxation rate, this plot should be linear with a slope, $-T_D \alpha p m^*/m_e$, which gives directly the Dingle temperature.

Effect of Zeeman Splitting, R_S

In a magnetic field, the spin degeneracy is lifted by Zeeman splitting, with the result that each energy level, ϵ , is split into two sublevels according to the two spin orientation with respect to the magnetic field direction. The energy gap which separates the split levels amounts to $\Delta\epsilon = g^* \mu_B B$, where $\mu_B = e\hbar/2m_e$ is the Bohr magneton and g^* the electronic g -factor (for free electrons $g = 2.0023$) renormalized by both carrier-carrier and carrier-phonon interactions and averaged over the extremal orbit [15]. Thus, two sets of Landau levels evolve for the spin-up and spin-down electrons, respectively. They pass the Fermi surface at increasing field with a phase difference, $\pi\Delta\epsilon/\epsilon$, that leads to a reduction of the oscillation amplitude by the factor

$$R_S = \left| \cos\left(\frac{\pi}{2} p g^* \frac{m^*}{m_e}\right) \right|. \quad (2.14)$$

The oscillation amplitude of the p -th harmonic even vanishes when

$$p g^* m^*/m_e = 2n + 1, \quad (2.15)$$

with $n = 0, 1, 2, \dots$. This situation (known as spin-zero) may occur at distinct magnetic field orientations in the case of an angular dependence of the band structure effective mass, as it is usually found, e.g., in two-dimensional electronic systems. Provided that the angular dependence of the mass is known, the spin-splitting factor, $g^* m^*$, may be estimated from the angular positions of the spin-zeros. With the

²Strictly speaking, the mass which enters the Dingle reduction factor is not the same as that entering the temperature reduction factor. The latter one is renormalized by carrier-carrier as well as carrier-phonon interactions whereas the former is the unrenormalized bandstructure effective mass, m_{band} [14]. For the compounds studied in this work, m_{band} is not exactly known. For simplicity, the mass estimated from the temperature dependence of the oscillation amplitude is used for the determination of the Dingle temperature. It has to be taken into account that in the presence of not negligible electron-phonon interactions this procedure results in an underestimation of the Dingle temperature.

effective cyclotron mass value determined by the temperature dependence of the oscillation amplitude the factor g^* can be directly obtained. As mentioned above, g^* and m^* are both renormalized by carrier-carrier as well as carrier-phonon interactions. For small corrections, the product of both factors, however, depends only on carrier-carrier interactions: $g^*m^* = g_s \cdot m_{band}(1 + A^{EE})/(1 + B^{EE})$ [9], where g_s is the g value affected by spin-orbit coupling, as it would be measured by electron spin resonance (ESR), and A^{EE} and B^{EE} are the correction coefficients of m_{band} and g_s , respectively, due to carrier-carrier interactions. For the case of negligible B^{EE} , further information might be extracted by setting g_s , to a good approximation, to $g_s = 2$ in order to estimate the so-called “bare” mass, $m_b = m_{band}(1 + A^{EE})$. By comparing the bare mass with the effective cyclotron mass m^* which, in the approximation of small correction coefficients can be expressed as $m^* = m_b(1 + \lambda)$, an approximate value for the carrier-phonon coupling constant λ is obtained.

2.2.2 Magnetic Breakdown

The LK formula in the form (2.9)/(2.10) considers only the contribution of electrons on well defined closed orbits that give rise to magnetic field independent quantum oscillation frequencies. However, in some multiband metals neighboring orbits may be separated by only a small energy gap ϵ_g . Above a threshold magnetic field the carriers are able to tunnel through this gap following a new trajectory. This tunneling process is known as magnetic breakdown (MB). As soon as the additional trajectory is a closed orbit in \mathbf{k} -space, a new oscillation frequency arises whose value corresponds to the new area encompassed by the so-called MB orbit. With increasing magnetic field, more and more carriers populate the MB orbits and contribute to the amplitude of the MB oscillations. Hence the field dependence of the oscillation amplitude of the original orbit is weakened in favor of that of the new arising orbits.

The probability of MB can be expressed as [16]

$$P = \exp\left(-\frac{B_0}{B}\right), \quad (2.16)$$

where the MB field parameter B_0 can be approximately defined as

$$B_0 \approx \frac{m^* \epsilon_g^2}{e \hbar \epsilon_F}. \quad (2.17)$$

At high enough magnetic fields, the contribution of the original orbit to the LK formula splits into as many terms as new orbits evolve plus the original one. According to Pippard’s coupled network model [17, 18], each term has to be multiplied by the MB reduction factor [19],

$$R_b = C(i\sqrt{P})^{n_1} \sqrt{1 - P}^{n_2}. \quad (2.18)$$

The weighting factor C takes into account that different electron orbits may enclose the same area because of their asymmetry. It is essentially the number of orbits

that enclose the same area within the unit cell in the \mathbf{k} -space. n_1 is the number of points in the relevant orbit at which MB occurs, whereas n_2 counts the points where two bands lie close to each other but the carrier keeps its original trace. Even if it is an idealized approximation, the present model can be directly applied to the FS configuration as it is found in the κ -phase quasi two-dimensional organic superconductors such as the compound κ -(BEDT-TTF)₂Cu[N(CN)₂]Br discussed in this work.

2.3 Shubnikov-de Haas Effect

Very shortly before the discovery of the dHvA effect in bismuth [2], Shubnikov and de Haas [1] had found oscillations in the field dependence of the resistivity in the same material. The finding of this phenomenon named after its discoverers represents the first observation of magneto-quantum oscillations. The theory underlying to this effect is far more complicated than that of the dHvA effect that is well described by the LK formalism for most metals. As was discussed by Adams and Holstein [10] and pointed out in more detail by Pippard [20], the origin of the SdH oscillations consists essentially of the fact that the probability of electron scattering is proportional to the matrix element describing the scattering potential and the number of states into which the electrons can be scattered. The matrix element does not considerably change by the orbit quantization in a magnetic field. On the contrary, the number of permitted final states does, since it consists of the integral of the product of the density of states and the Fermi distribution. Hence, the probability of scattering which determines both, the electronic relaxation time and the resistivity, oscillates in a varying field following the oscillation of the density of states at the Fermi level. Adams and Holstein calculated the oscillatory electrical conductivity considering phonon and ionized-impurity scattering. It turns out that, although both scattering mechanisms are completely different, they affect the conductivity to the same order of magnitude. Thus, they argue that the result may be regarded as valid for an arbitrary scattering mechanism. The electrical conductivity transverse to the magnetic field can be expressed in the general form

$$\sigma_{xx}(B) = \sigma_0(B) [1 + \Delta\tilde{\sigma}_1(B) + \Delta\tilde{\sigma}_2(B)], \quad (2.19)$$

where σ_0 represents the classical background conductivity and $\Delta\tilde{\sigma}_1$ and $\Delta\tilde{\sigma}_2$ introduce quantum corrections of different types,

$$\Delta\tilde{\sigma}_1(B) = \frac{5}{2} \sigma_0(B) \left(\frac{\hbar\omega_c(B)}{\epsilon_F} \right)^{\frac{1}{2}} \left[\frac{1}{2} \left(\frac{\hbar\omega_c(B)}{\delta\epsilon_{\parallel}} \right)^{\frac{1}{2}} - \left(\frac{1}{2} + \frac{\delta\epsilon_{\parallel}}{\hbar\omega_c(B)} \right)^{\frac{1}{2}} \right] \quad (2.20)$$

and

$$\Delta\tilde{\sigma}_2(B) = \frac{3}{2} \sigma_0(B) \left(\frac{\hbar\omega_c(B)}{\epsilon_F} \right) \left[\frac{1}{2} \left(\frac{\hbar\omega_c(B)}{\delta\epsilon_{\parallel}} \right)^{\frac{1}{2}} - \left(\frac{1}{2} + \frac{\delta\epsilon_{\parallel}}{\hbar\omega_c(B)} \right)^{\frac{1}{2}} \right]^2. \quad (2.21)$$

$\omega_c = eB/m^*$ is the cyclotron frequency and $\delta\epsilon_{\parallel}$ the amount of energy by which the Fermi level exceeds the energy state of $k_{\parallel} = 0$ associated with the highest occupied Landau level below the FS, $\delta\epsilon_{\parallel} = \epsilon_F - (n_{\max} + \gamma) \hbar\omega_c(B)$. The term $\Delta\tilde{\sigma}_1(B)$ represents scattering of electrons from the highest occupied Landau level to levels above the FS, i.e., inter-level scattering. $\Delta\tilde{\sigma}_2(B)$ stands for intra-level scattering

of electrons within the highest occupied Landau level. For most experiments the second term is negligible since it becomes only relevant in the quantum limit, $(n + \gamma) = F/B \sim 1$. The crucial variable in both correction terms is the energy difference $\delta\epsilon_{\parallel}$. As the magnetic field is varied, $\delta\epsilon_{\parallel}$ vanishes with a Landau level passing the boundary of the extremal FS cross-sectional area. In the case of ideally sharp Landau levels and a FS of a two-dimensional electronic system, $\Delta\tilde{\sigma}_1(B)$ and $\Delta\tilde{\sigma}_2(B)$ would diverge for the corresponding values of magnetic field strength thus entailing a singularity in the conductivity $\sigma_{xx}(B)$. This effect is damped by the FS curvature in field direction that causes a finite $\delta\epsilon_{\parallel}$ value as well as by a finite width of the Fermi distribution function and Landau level broadening, in a similar way as discussed in the previous section. Therefore the amplitude reduction factors, R_T , R_D , and R_S , apply accordingly.

In order to relate the result of Adams and Holstein to the LK formula, the conductivity given by Eqs. (2.19)-(2.21) may be expressed in terms of the oscillatory and steady density of states at the Fermi energy, $\tilde{D}(\epsilon_F)$ and $D_0(\epsilon_F)$ [9]:

$$\sigma_{xx} = \sigma_0 \left\{ 1 + R_T \left[5 \frac{\tilde{D}(\epsilon_F)}{2 D_0(\epsilon_F)} + \frac{3}{2} \left(\frac{\tilde{D}(\epsilon_F)}{D_0(\epsilon_F)} \right)^2 \right] \right\} \quad (2.22)$$

As mentioned above, the number of final states in the scattering process is determined by both, the density of states and the Fermi distribution function. In contrast to the damping effects due to finite relaxation time and the effect of Zeeman splitting, the temperature reduction factor is not concerned with the density of states but with the Fermi distribution function and therefore does not enter $\tilde{D}(\epsilon_F)$.

The density of states at the Fermi level can be calculated from first principles, by integrating the contributions from two-dimensional slabs of \mathbf{k} -space normal to the magnetic field over k_{\parallel} in the same way as it is usually done to obtain the thermodynamic potential. As the thermodynamic potential is already known, the density of states is more easily deduced from the basic definition (2.8) by replacing the sum over all possible energy states by an integral:

$$\Omega(\epsilon_F, T) = -k_B T \int_{-\infty}^{+\infty} D(\epsilon) \ln \left[1 + \exp \left(\frac{\mu - \epsilon}{k_B T} \right) \right] d\epsilon. \quad (2.23)$$

For zero temperature the density of states at the Fermi level is obtained by differentiating twice,

$$D(\epsilon_F) = -\frac{\partial^2 \Omega}{\partial \epsilon_F^2}. \quad (2.24)$$

With regard to the oscillatory parts of the thermodynamic potential and of the density of states at the Fermi energy, Eq. (2.24) yields the relation

$$\tilde{D}(\epsilon_F) = \frac{1}{R_T} \frac{m^*}{e\hbar} \left(\frac{B}{F}\right)^2 \frac{d\tilde{M}}{dB}, \quad (2.25)$$

where \tilde{M} corresponds to the values given in Eq. (2.9)/(2.10). For the case of high quantum numbers, n , and a spherical FS the oscillatory part of the electrical conductivity takes the form

$$\frac{\tilde{\Delta}}{\sigma_0} = \frac{5}{2} \sqrt{\frac{\pi e \hbar}{\epsilon_F}} \frac{\sqrt{B}}{\sqrt{m^* |A''_{extr}|}} \sum_{p=1}^{\infty} \frac{R_T(p) \cdot R_D(p) \cdot R_S(p)}{p^{1/2}} \cos \left[2\pi p \left(\frac{F}{B} - \frac{1}{2} \right) \pm \frac{\pi}{4} \right]. \quad (2.26)$$

In conventional experiments, it is usually not the conductivity rather than the resistivity, ρ , which is measured. For a correct application of Eq. (2.26), an inversion of the resistivity tensor has to be performed. This procedure is essential for metals that exhibit strong quantum oscillations, where $\tilde{\Delta}$ is of the order of σ_0 and the Hall components are not negligible. As shown later, the magneto-quantum oscillations in the compound κ -(BEDT-TTF)₂Cu[N(CN)₂]Br turn out to be very weak ($\Delta\tilde{\sigma} \ll \sigma_0$) and the error which is made by the approximation $|\Delta\tilde{\sigma}/\sigma_0| \approx |\Delta\tilde{\rho}/\rho_0|$ is therefore much smaller than the experimental error.

2.4 Magneto-Quantum Oscillations in 2D Electronic Systems

The derivation of the LK formula for the dHvA effect as well as the theory of Adams and Holstein for the SdH effect are based on a spherical FS shape of a three-dimensional electron system. For this case, every Landau tube which lies within the extremal FS orbit crosses the FS [see Fig. 2.1(a)]. Owing to the finite curvature of the FS along the magnetic field direction, the electrons that lie on the outer tubes are continuously redistributed onto the next inner tubes with increasing field. This leads to nearly ideally sinusoidal quantum oscillations of moderate amplitudes. The situation changes completely for low-dimensional electron systems [see the two-dimensional case in Fig. 2.1(b)]. Here, the FS curvature factor $|A''_{extr}|^{-0.5}$ tends to become singular along the least conduction direction and the LK formalism breaks down. Approaches proposed to derive an alternative formula for the oscillatory magnetization in a two-dimensional electron gas usually consider two limiting cases: a fixed number of electrons occupying the Landau levels that results in a chemical potential which oscillates as a function of the magnetic field (canonical ensemble) and the case of a fixed chemical potential with the number of electrons varying with field (grand canonical ensemble). Within the first approach Vagner *et al.* [21, 22, 23] calculated the magnetization in high magnetic fields and at low temperatures considering the amplitude reduction due to finite temperature,

whereas Shoenberg [9] employed the latter approximation to give an analytical expression which takes into account the main damping mechanisms but is only valid for low magnetic fields and high temperatures. More recent works [24, 25, 26] studied the general case of a closed quasi-cylindrical FS sheet which is affected by a magnetic field independent reservoir which provides electron transfer to the closed FS. They focussed onto a model geometry of closed and open FS sheets that are separated by an energy barrier, similar to the FS configuration found in the family of $(\text{BEDT-TTF})_2\text{X}$ compounds as shown later in this work. Depending on the barrier height and the gap in \mathbf{k} -space different shapes of oscillations, from extreme sawtooth and inverse sawtooth to perfect symmetric sinusoidal, result. Latest works [27] additionally consider the case of a corrugated structure of the FS. Such so-called warping is often important in quasi two-dimensional systems like the BEDT-TTF salts that exhibit weak coupling between neighboring conducting layers.

Chapter 3

Experiment

Several experimental conditions have to be realized for a successful observation of magneto-quantum oscillations in metals. A main prerequisite is that an electron has to be able to trace its cyclotron orbit more than once before it is scattered, i.e., the cyclotron frequency has to be higher than the scattering rate, $\omega_c \tau \gg 2\pi$. This implies the need for samples that come close to an ideally pure single crystal without any defects as well as for the use of very low temperatures. Imperfections of the crystal and thermal broadening can be compensated to some extent by the application of high magnetic fields so as to increase the cyclotron frequency, $\omega_c = eB/m^*$. The following sections briefly discuss how these conditions are realized at the Grenoble High Magnetic Field Laboratory (GHMFL). Furthermore, the techniques that were used to detect the dHvA and SdH effect, respectively, in the measurements performed in this work will be presented.

3.1 High Steady Magnetic Fields

The generation of magnetic fields is based on a current passing through a coil thus inducing the maximum field in the center of the coil. The main configurations that have proved to meet the requirements that arise with the production of very high quasi-static fields (> 20 T) are resistive magnets with so-called Bitter or polyhelix coils and the hybrid system which consists of a combination of resistive and superconducting parts.

The magnet type invented by F. Bitter [28] in 1936 is still widely in use since it allies a robust construction with relatively low costs. It consists of a stack of conducting circular disks that are insulated from each other by a Kapton foil except a slit of $\sim 20^\circ$. The slits are radially shifted from one to the next, that allows the current to flow helically through the stack. The disks are usually made of copper that allows to keep the electrical resistance as low as possible at a high stress stability. In order to ensure proper contacts between the disks, they have to be pressed onto one another by a force of at least 1 kN/cm^2 [29]. The Joule heat produced by dissipative current transport is drawn off by de-ionized water pumped under high pressure through holes drilled vertically into the stack of Bitter plates. The current density in this coil configuration is proportional to $1/r$, where

r is the radius from the center of the coil, resulting in high fields in the bore but requiring extra technical effort concerning the water cooling and mechanical support in this region. With regard to these limiting factors the more recent design of the polyhelix magnet [30] was developed to optimize the current density distribution. It consists of several copper coils concentrically fitted into each other. This configuration enables the current density to be adjusted separately for each coil both radially and parallel to the magnetic field. The cooling is effected by pressurized water flowing axially between neighboring coils. The choice between both types of magnets is generally governed by compromising on the flexible tuning of the electrical current, that is possible with the polyhelix magnet, and the more frugal manufacture of the Bitter magnet. In order to profit by both eligibilities, combinations of the two types are often used. As an example, a sketch of the at present most powerful magnet in Grenoble which was employed for most of the experiments carried out in this work is displayed in Fig. 3.1. This magnet consists of a polyhelix system surrounded by two small Bitter coils. This inner part is inserted into the bore of two big concentric Bitter magnets. For the standard configuration of a 50 mm inner bore diameter available for the experiment, the inner part produces a maximum field of 20 T which is added to the field of up to 10 T produced by the big Bitter part. In order to reach the maximum field of 30 T, a total current of 30 kA and a water flow rate of $\approx 1000 \text{ m}^3/\text{h}$ is applied. The upper limit of the field, from the technical point of view, is set by the highest possible cooling rate as well as by very strong Lorentz forces onto the coils that emerge at high fields. Another constraint represents the total available electrical power of 20 MW. These limits can be partially extended by a hybrid configuration [31], the combination of resistive Bitter and polyhelix magnets with a superconducting magnet around them. The superconducting part is cooled by a bath of liquid helium which is pumped to a temperature of about 2 K. The hybrid magnet at the GHMFL which was employed for some experiments presented in this work will be replaced by a more powerful system. For a long time it produced the world's record fields of up to 31.4 T.

The spatial homogeneity of the field produced by the above mentioned magnet types is of the order of $\Delta B/B = 10^{-3}$ at a distance of 1 cm from the field center. The field stability in a resistive magnet is determined by the stability of the power supplies which is about $\Delta I/I \sim 10^{-5}$. At the highest fields this corresponds to a noise of $\sim 10^{-4}$ T. Both magnetic field specifications do not represent any major restrictions for the experiments carried out in this work.

3.2 Cryogenic System

The temperature range necessary for the detection of the dHvA and SdH oscillations was realized using a combination of a ^3He insert immersed into a conventional ^4He bath cryostat. The lower end of the ^3He cryostat is thermally isolated from the ^4He bath by a vacuum space, whereas a copper cone in the middle of the insert provides direct thermal contact to this bath. The temperature of the liquid ^4He

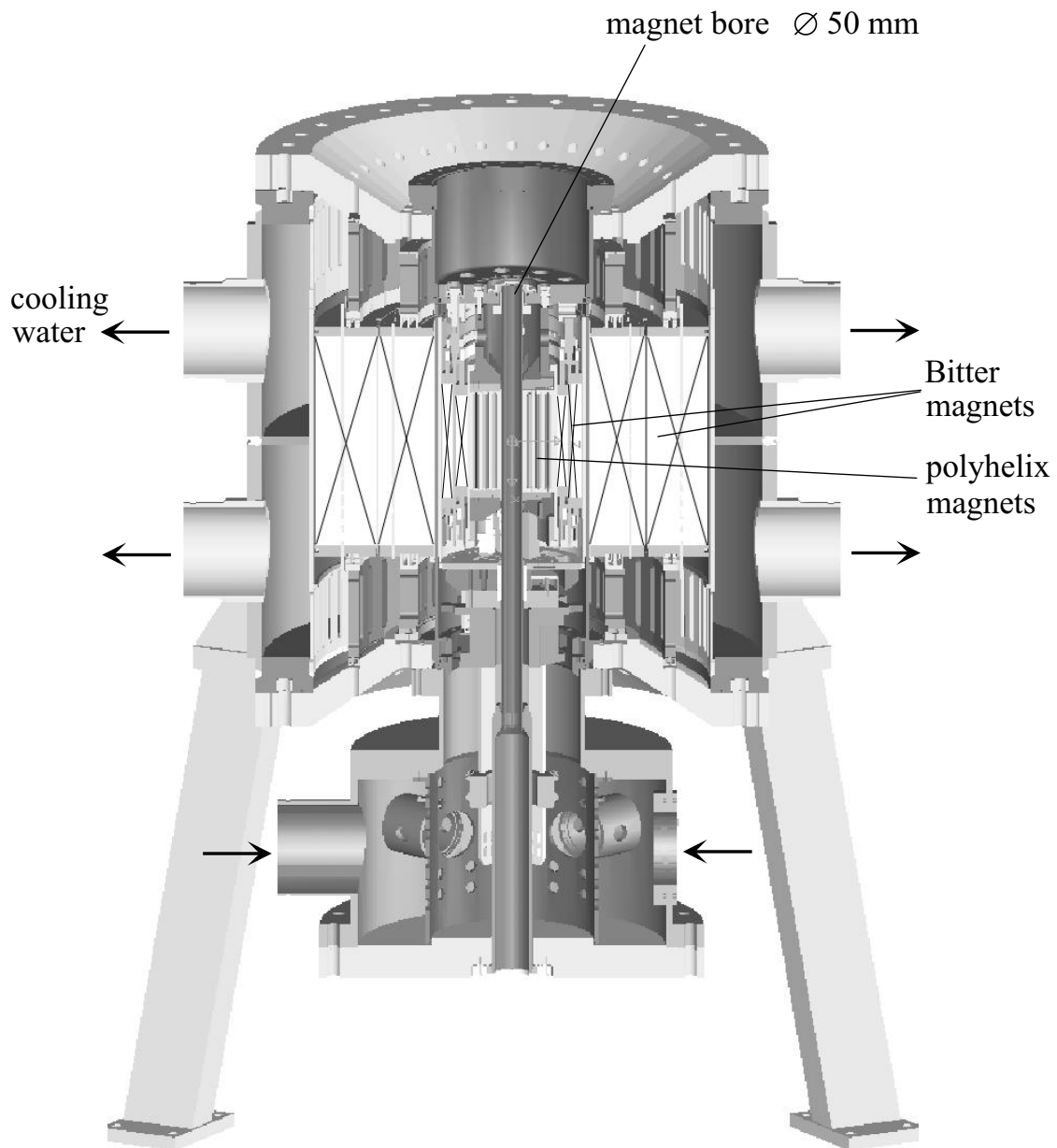


Figure 3.1: 20 MW resistive magnet.

can be lowered from 4.2 Kelvin at ambient pressure to ≈ 1.3 Kelvin by lowering the vapor pressure above the liquid ^4He bath. At around 2.1 K, the ^3He gas contained in the insert condenses at the copper cone. By pumping the ^3He bath, temperatures down to 380 mK can be achieved. In typical experiments, this temperature can be kept for around 10 hours.

3.3 Temperature Measurement and Control

For the determination of the temperature, a calibrated RuO_2 resistor of 10 k Ω room temperature resistance was used for nearly all experiments. Advantages of this resistor type are a high sensitivity in the temperature range below 4.2 K and a weak magnetic field dependence. The temperature dependent electrical conductivity of the RuO_2 sensor was measured by the four-probe AC technique using a conductance bridge.¹ The current induced by the excitation voltage was checked not to heat the thermometer. Changes in the temperature could be measured with an accuracy of ~ 1 mK below 4 K, ~ 10 mK below 10 K, ~ 0.1 K between 10 K and 20 K, and ~ 1 K above. Below 4.2 K it was verified by the vapor pressure above the ^4He and ^3He bath, respectively. In some measurements a cernox resistor was used which exhibits an extremely low magnetic field dependence and a measuring range of up to 100 K.

For all measurements that are performed in a variable magnetic field, it is indispensable to stabilize the temperature to a high extent. In the combination of ^3He and ^4He baths, there are three temperatures that are naturally stable: 4.2 K, where the ^4He is condensed, ~ 1.3 K, the lowest temperature which could be reached by pumping the ^4He bath with the pump used in the experiment and ~ 0.4 K, the base temperature which is reached by pumping the ^3He bath. For the stabilization of the temperature between and above these points different methods were used. In the temperature ranges 4.2 K to 1.3 K and 1.3 K to 0.4 K, the temperature was stabilized by keeping a constant vapor pressure above the ^4He and ^3He bath, respectively. In both temperature ranges, the maximum deviation of the desired temperature could be restricted to $\Delta T \sim 10$ mK. For the temperature control above 4.2 K, a manganin wire served as a heater. As a first step, the ^3He was nearly totally pumped out of the insert except for a pressure of a few mbar which served as a contact gas to the liquid ^4He bath. Then a current of typically $\sim 10 - 100$ mA was applied to the heater in order to regulate the temperature. Since this method does not allow to accurately equilibrate the heat input and cooling power, it was only used to perform temperature sweeps.

3.4 Detection Methods

For the detection of dHvA oscillations a cantilever beam torquemeter developed by Christ and Biberacher [32, 33] was employed whereas the oscillations in the

¹Barras Provence Siemensmetre

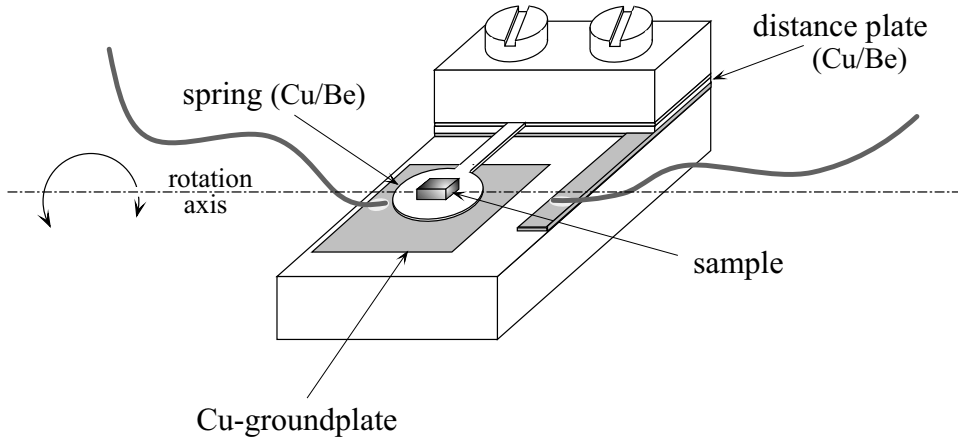


Figure 3.2: Sketch of the capacitive torque meter.

electrical resistance were measured by the standard four-probe technique. The principles of these measurements and their experimental realization are described in this section.

3.4.1 Torque Method

A magnetic moment \mathbf{m} placed in a magnetic field \mathbf{B} generates a torque $\boldsymbol{\tau}$ in the direction perpendicular to \mathbf{m} and \mathbf{B} :

$$\boldsymbol{\tau} = \mathbf{m} \times \mathbf{B}. \quad (3.1)$$

For a sample of magnetization \mathbf{M} which is homogeneously distributed over the volume V the absolute value of the torque amounts to

$$\tau = M_{\perp} BV, \quad (3.2)$$

where M_{\perp} denotes the magnetization component perpendicular to the magnetic field. Using relation (2.10) it can be written in terms of the magnetization M_{\parallel} parallel to the field:

$$\tau = -\frac{1}{F} \frac{dF}{d\theta} M_{\parallel} BV. \quad (3.3)$$

The detection of dHvA oscillations by the torque technique requires an anisotropy of the FS, i.e., $dF/d\theta \neq 0$. Furthermore, the torque vanishes when the magnetic field points into a direction parallel to a symmetry axis of the crystal. In this case either $dF/d\theta$ is equal to zero or opposite components of the torque cancel each other out.

The device used to measure the torque in the experiments presented in this thesis is a capacitive torque meter (Fig. 3.2). The capacitor consists of a copper-groundplate and a plane-parallel circular plate made of copper-beryllium. The circular plate is connected via a narrow cantilever beam ($\approx 0.4 \mu\text{m}$ wide and

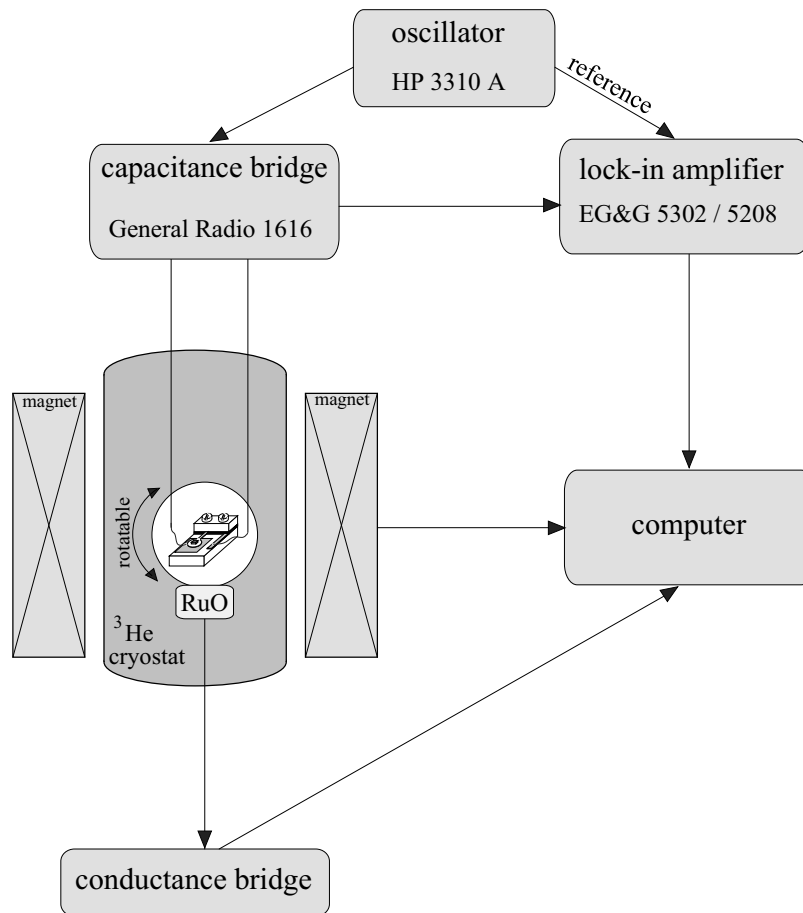


Figure 3.3: Schematic view of the set-up used for the detection of de Haas-van Alphen oscillations by the torque technique.

≈ 3 mm long) to a rectangular plate. Both parts are etched out as a whole from one sheet. The rectangular plate is fixed to the sample holder separated by a distance plate from the plane of the groundplate. The diameter of the circular plate used in the experiment is ≈ 3 mm, its thickness $25 \mu\text{m}$, that of the distance plate $50 \mu\text{m}$. The sample is mounted onto the circular plate by a small amount of vacuum grease. When the sample is subject to a torque in the magnetic field the cantilever plate acts as a spring where the distance and hence the capacitance between the spring and the groundplate are slightly changed. The present cantilever is rather rigid and especially for one of the title compounds, namely the κ -(BEDT-TTF) $_2$ Cu[N(CN) $_2$]Br, the changes in the capacitance turned out to be very weak ($\Delta C/C < 1\%$). For such small excitations of the spring, so-called torque interaction is negligible and the capacitance can be assumed to be proportional to the torque. The torque was measured using a precision capacitance bridge² and standard lock-in technique³. Since the analysis of the electronic properties discussed in

²General Radio 1616 capacitance bridge

³EG&G 5302 and 5208 lock-in amplifier

this work requires only the detection of the relative changes of the torque, the measurements have been carried out in the range of highest sensitivity by setting off the background signal. A 5.27 kHz AC excitation voltage⁴ of typical amplitude of 15 V was inductively coupled to a circuit with the capacitance of the torquemeter connected in series with a tunable capacitance. The excitation voltage served also as a reference signal for the lock-in amplifier. At the beginning of each measurement both capacitances were compensated so that the induced excitation voltage vanished. In a magnetic field sweep the variations of the torquemeter capacitance were detected by measuring the amplitude of the compensation detuning via the voltage which was induced in the circuit. Besides this method, several experiments were carried out using a capacitance bridge⁵ which directly provides the value of the measured capacitance. In order to perform measurements at different sample orientations, the torquemeter was mounted onto a rotatable holder. The angular resolution of the worm gear driving the sample holder was better than 0.1° . The sample holder was mounted to the low-temperature tail of a self-made insert which fits into the ^3He cryostat. A sketch of the whole assembly inserted into the magnet bore is shown in Fig. 3.3.

3.4.2 Four-Probe Technique

Since the NaBa_3N crystal investigated in this work can only be handled sealed in a glass capillary under argon atmosphere, it is not possible to study its electrical magnetoresistance directly. Therefore, the following description of the detection of SdH oscillations is focussed onto the application to the quasi-two-dimensional organic superconductor $\kappa\text{-(BEDT-TTF)}_2\text{Cu}[\text{N}(\text{CN})_2]\text{Br}$.

Four contacts on the sample were made by use of annealed platinum wires of 20 μm diameter attached with a conducting carbon paint. Concerning the choice of a suitable contact geometry for an interplane⁶ resistance measurement, care has to be taken to have no current in the ac plane direction as this current contribution exhibits other magnetoresistance properties. Hence, the contact paste must not cover the edge of the crystal rather than only touch the conducting plane surface. Therefore, the contacts were placed on opposite faces of the sample with the current applied perpendicular to the highly conducting ac plane. This configuration yields much larger and thus more easily measured resistances than in the case of the current parallel to the conducting layers. Expressed by the ratio of the inter-plane and in-plane conductivity, the extreme anisotropy in the conductivity was typically $\sigma_\perp/\sigma_\parallel \sim 10^{-2}$. The sample cross-section perpendicular to the crystallographic b -axis amounted to $\sim 0.5 \text{ mm}^2$, whereas the typical sample thickness was $\sim 200 - 300 \mu\text{m}$. That allows to assume the current distribution in such a way that the voltage drops only perpendicular to the highly conducting

⁴supplied by a Hewlett Packard 3310A oscillator

⁵Andeen Hagerling 2500A 1 kHz Ultra-Precision Capacitance Bridge

⁶I.e. perpendicular to the highly conducting plane of the layer structured sample. In the case of $\kappa\text{-(BEDT-TTF)}_2\text{Cu}[\text{N}(\text{CN})_2]\text{Br}$ this direction coincides with the crystallographic b axis normal to the ac plane.

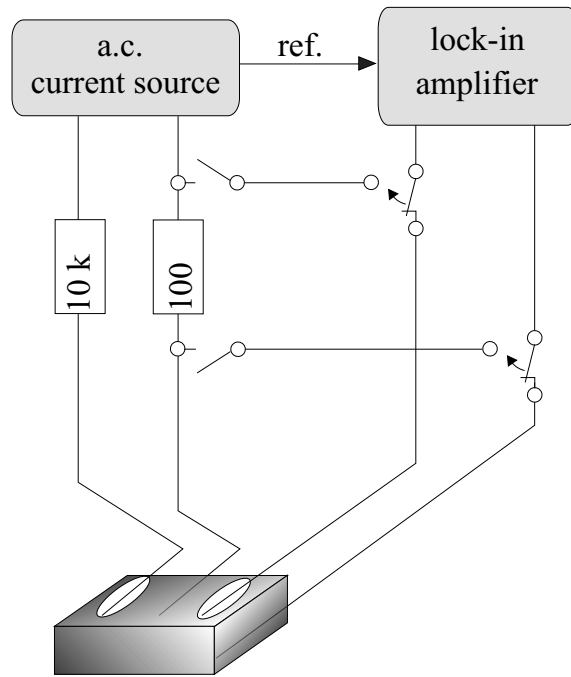


Figure 3.4: Schematic diagram of the set-up used to detect the interlayer magnetoresistance of κ -(BEDT-TTF) $_2$ Cu[N(CN) $_2$]Br.

layers and the whole voltage which drops between the current contacts is measured. The accuracy of this assumption is believed to be better than 1%. The excitation current was applied to the sample by an AC current source and was chosen in the range of 10 to 100 μ A r.m.s. This current intensity was checked not to heat the sample within an accuracy better than 10 mK at the lowest temperature. The frequency of the excitation current was widely varied from one measurement to the other between 15 Hz and 4 kHz. The voltage induced by this current was usually enhanced by a preamplifier⁷ before it was measured by the lock-in amplifier which was fed by the excitation signal as a reference. This technique allows the voltage to be measured without any current flowing through the voltage contacts and hence avoids the sample resistance to be distorted by additional resistance contributions. For the adjustment of the current and the phase in the sample circuit a high quality 100 Ω resistor was employed as sketched in Fig. 3.4. In order to stabilize the current through the sample a 10 k Ω resistor, also of superior quality, was connected in series. Hence, a change of the sample resistance from 100 Ω to 0 Ω entailed a variation of only 1% in the current. The typical sample resistance in the experiments was $\sim 1 \Omega$ at low temperatures and could be determined with an accuracy better than 10^{-4} . Typical values for the contact resistance at room temperature were $< 10 \Omega$ per contact, that is small enough not to provoke any heating of the sample with the above given excitation current.

⁷ITHACO 565 Ultra Low Noise Transformer Coupled Voltage Preamplifier or internal preamplifier of EG&G 5302 lock-in amplifier

3.4.3 Simultaneous Torque and Transport Measurement

A series of measurements was carried out by use of a set-up which allowed to measure the magnetic torque and the magnetoresistance simultaneously. The realization of such an experiment requires an extra effort, in order to avoid any crosstalk between the two signals. Especially thin platinum wires of 10 μm diameter have been attached to the sample with contact paste,⁸ in the configuration detailed above. The use of such an extremely small diameter prevents the wires from acting as springs that artificially influence the force onto the torquemeter. It turned out that, at low magnetic fields, the sample easily moves off the plate when it is in the superconducting state. Therefore the surface of the plate was covered by thin paper which gives better adhesion.

3.5 Pressure Cell

For several magnetotransport measurements, quasi-hydrostatic pressure was applied making use of a clamp cell (Fig. 3.5/3.6). The cell was made of $\text{Cu}_{98}\text{Be}_2$ alloy which was hardened by heating for three hours in a stove at a temperature of 320°C and subsequent slow cooling down to room temperature. The same system had been already used in the measurements that had revealed SdH oscillations in $\kappa\text{-(BEDT-TTF)}_2\text{Cu[N(CN)}_2\text{]Br}$ for the first time [34].

Copper wires of 100 μm thickness were led into the cell via a feedthrough. The 0.7 mm bore of the feedthrough served as the channel and was sealed by epoxy.⁹ Annealed platinum wires of 20 μm diameter and ~ 1.5 mm length were soldered to the copper wires that came out of the epoxy at the sample side. The sample was contacted to these platinum wires as described above and adjusted with its conducting plane perpendicular to the magnetic field. A cylindrical Teflon cup containing the mineral oil GKZh, which served as a pressure medium, was put over the sample and the top of the feedthrough. This sort of oil is especially suitable for low temperature experiments because of its pressure and temperature properties. It has a very low compressibility that allows to use a short Teflon cup and pressure channel. Furthermore, it has a low melting point, 160 K - 220 K, depending on the applied pressure, and does not crystallize but remains amorphous in the solid state, thus providing rather isotropic pressure at low temperatures. In order to seal the pressure space, a copper-beryllium washer was placed between the Teflon cup and the feedthrough, the sharp edge touching the Teflon cup. The feedthrough with the Teflon cup at the head was put into the channel of the pressure cell which fitted the cup exactly in diameter. Pressure was applied via a tungsten-carbide piston which was placed in this channel and had the same diameter as the Teflon cup. Since the middle part of the channel became slightly larger in diameter after the first loadings, a copper washer was placed between the Teflon cup and the piston, again with the sharp edge towards the Teflon cup. This prevents the bottom of

⁸DuPont silver paste

⁹blue Araldite or 3M epoxy

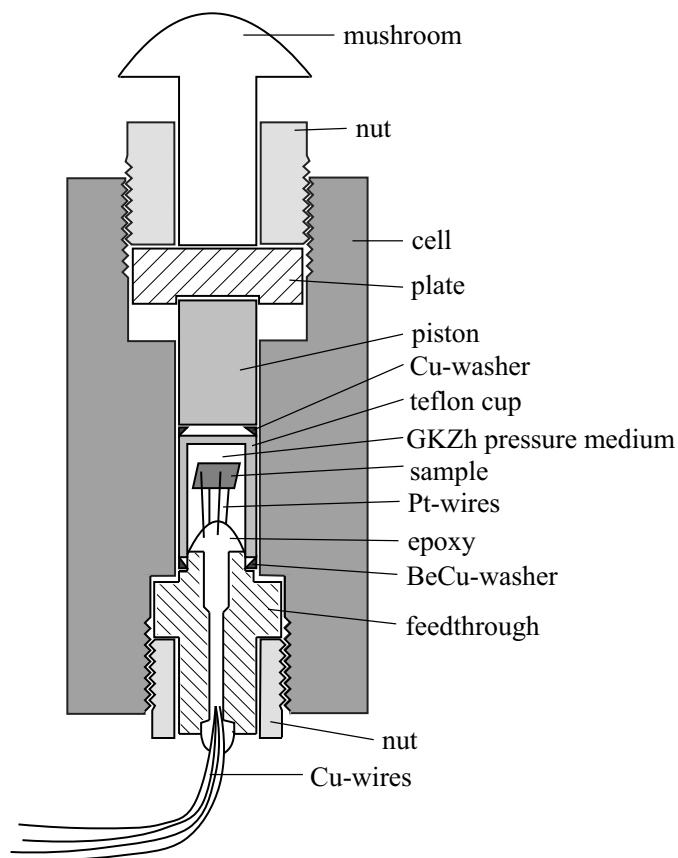


Figure 3.5: Sketch of the copper-beryllium clamp cell. The height and diameter of the cell body amount to 39 mm and 22 mm, respectively.

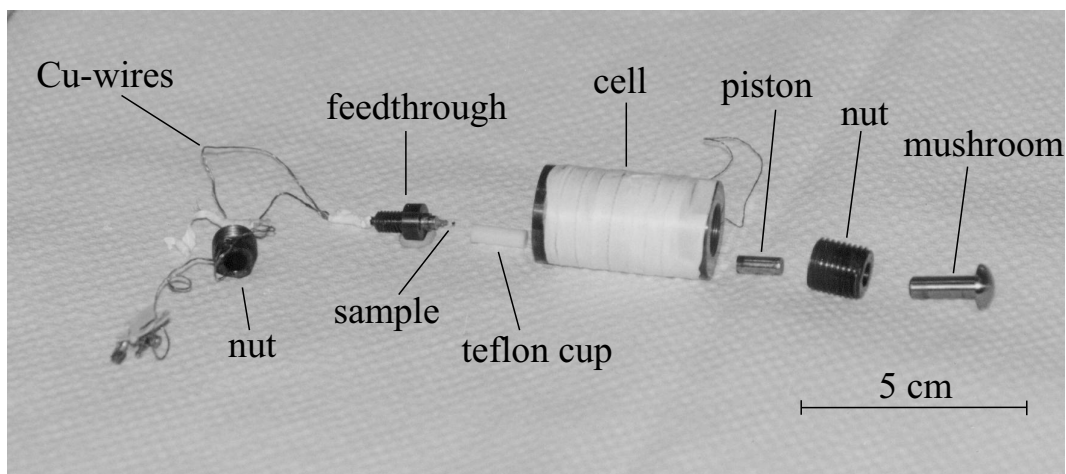


Figure 3.6: Parts of the pressure cell assembly. The heater which is wound around the cell is protected by a Teflon tape.

the Teflon cup from destruction by flowing, under pressure, into the space between the piston and the channel wall. It has to be kept in mind that this washer could cause additional friction in the channel.

The cell was loaded in a press under continuous control of the applied loading force and the sample resistance. This control served as a check of the reproducibility of the loading and deloading processes and even allowed an inference to the applied pressure owing to the pronounced sensitivity of the sample resistance to the pressure. The normal procedure for the estimation of the pressure in the sample was based on the loading force at room temperature which was corrected for low temperatures according to Ref. [35]. Such an estimation is believed to be within an accuracy of $\approx 10\%$. The highest pressure applied amounted to 15 kbar at room temperature that corresponds to ≈ 12.5 kbar at low temperatures.

The pressure cell was mounted to the low-temperature tail of a ^3He insert which was based on a similar operating principle as that used for the torque measurements and was specially designed for the present pressure experiment.

Chapter 4

Magneto-Quantum Oscillations in κ -(BEDT-TTF)₂Cu[N(CN)₂]Br

4.1 The Organic Superconductor

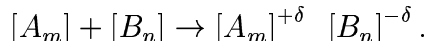
κ -(BEDT-TTF)₂Cu[N(CN)₂]Br

During the first half of the twentieth century there was only limited interest in the solid-state properties of organic molecules and their ions. Conventional organic solids have covalent chemical bonds within each molecule and only much weaker van der Waals or London interactions between molecules. The constituent cations and anions usually carry no formal charges that could mediate Coulomb interactions between organic molecules in crystals. The prerequisites of building conducting molecular solids are the creation of free carriers and their delocalization throughout the crystal. Two main tracks have been successfully followed for the synthesis of stable organic conductors. Both attempts arose from a stimulating idea of W.A. Little [36], who proposed to look for conduction in materials constructed of polymeric chains with polarizable side groups. Owing to an “excitonic conduction”, this kind of materials was predicted not only to show electrical conductivity but rather to develop a superconducting state with transition temperatures possibly elevated up to $T_c = 2000$ K. However, this mechanism of conduction was never observed, and metallic conduction was obtained in a more classical way.

Most directly inspired by Little’s proposal was the doping of straight unsaturated covalent polymers. A suitable doping was known since long to drive graphite into a metallic state. With the discovery of fullerenes in 1985 [37], the doping method was also applied to these balloon-like compounds. Their tube-like extensions, found in 1991 [38] and well known under the main term of carbon nanotubes, are at present one of the most intensively studied fields of research.

The other approach was based on the idea to create compounds composed of A and B , with A acting as electron donor and B as electron acceptor. A should be an “electron-rich” molecule with a low ionization energy which can be easily oxidized by the acceptor B having the appropriate electron affinity. Both molecules combine

to form a charge-transfer complex according to the reaction



As long as no covalent binding exists between A and B , the van der Waals and metallic short-range interactions lead to a separation of the molecules into parallel stacks of A and stacks of B molecules. Their ionicity caused by the charge transfer ensures that both types of stacks alternate in space. The overlap of electronic states of the molecules within each stack leads to electrical conduction of predominantly one-dimensional character. Soon, it was realized that these quasi-one-dimensional metals are not “metals” in the low temperature region due to an instability of the planar FS ([39], and, e.g., [40] for a review of the special case of organic conductors). Of course, this instability has provided colorful physics but is not favorable to the superconductivity. Therefore chemists aimed to increase the dimensionality of the electronic structure by modifying the stacking architecture towards two-dimensional conduction paths. The main representatives of the resulting second-generation organic conductors are the BEDT-TTF charge-transfer salts, most of them being superconductors at low temperatures. Among the organic superconductors known today the BEDT-TTF based compounds yield the largest number. They display numerous compositions, (BEDT-TTF) _{m} X _{n} , with a remarkable variety of structural modifications. In the large majority the molecular ratio $m : n$ amounts to 2 : 1, i.e., two BEDT-TTF molecules transfer one electron to the acceptor X . With regard to superconductivity, the (BEDT-TTF)₂X salts with the complex anions $X = \text{Cu}(\text{NCS})_2^-$, $\text{Cu}[\text{N}(\text{CN})_2]\text{Br}^-$, and $\text{Cu}[\text{N}(\text{CN})_2]\text{Cl}^-$ (hereinafter referred to as κ -NCS, κ -Br, and κ -Cl, respectively, where κ denotes the special packing motif of the BEDT-TTF molecules in these compounds) are of particular interest. They yield the to date highest superconducting critical temperature values of 10.4 K [41], 11.6 K [42], and 12.8 K (at 300 bar) [43], respectively. Similar to the high- T_c cuprate superconductors, these compounds exhibit a competition and sometimes even coexistence of superconductivity and antiferromagnetism [44]. Both families of compounds can be characterized by qualitatively similar phase diagrams, with the difference that the key parameter for the cuprate superconductors is doping whereas it is pressure for the organic compounds. Fig. 4.1 displays the proposed phase diagram of κ -(BEDT-TTF)₂X [44]. With respect to the pressure axis, notably the κ -Br compound, with the highest T_c at ambient pressure, lies closest to the superconductor-insulator transition. Going from the κ -NCS to the κ -Cl the lattice volume slightly decreases. This contraction, however, is not isotropic and thus cannot be directly related to the position of each compound in the phase diagram. It is suggested that the crucial parameter is rather the ratio of the intra and inter dimer transfer integral [44]. This ratio increases from κ -NCS to κ -Cl and is proportional to the ratio of the on-dimer effective Coulomb interaction and the bandwidth, U_{eff}/W . Since U_{eff}/W is about unity for the κ -(BEDT-TTF)₂X family the superconductor-insulator transition is likely driven by electron-electron correlations and thus supposed to be of the

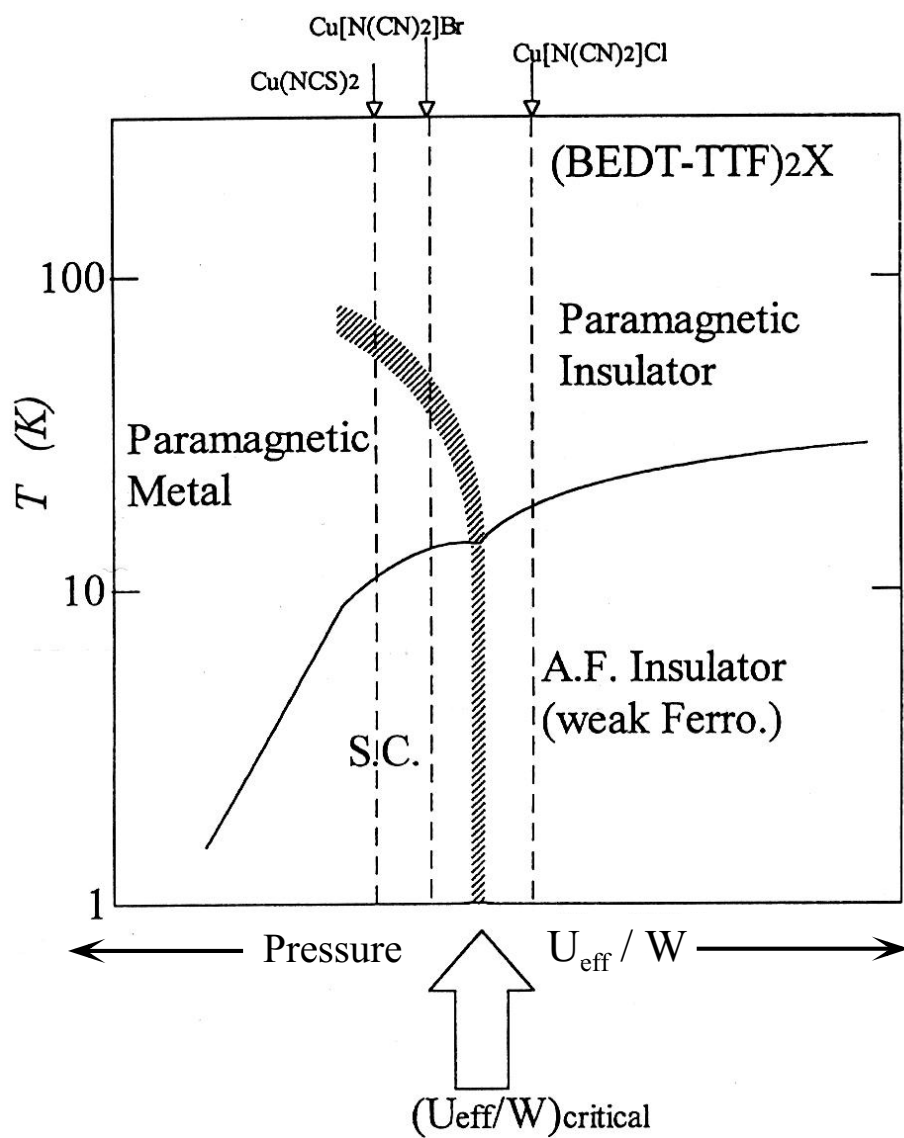


Figure 4.1: Phase diagram of κ -(BEDT-TTF)₂X proposed by Kanoda [44]. A.F. and S.C. denote antiferromagnetic and superconducting phases, respectively. U_{eff} is the effective on-site Coulomb interaction and W the bandwidth. The ratio U_{eff}/W is estimated to be of the order of unity for the κ -Br compound [45].

Mott type¹ [46]. Within this hypothesis, the difference in the anion entails a critical change in U_{eff}/W and thus provides the metallic, superconducting, and insulating ground states. These states can also be realized by physical pressure which causes an approximately isotropic contraction and leads to a suppression of electron-electron correlations. If we regard the change in the anion as variation of an “internal” chemical pressure the κ -(BEDT-TTF)₂X family exhibits the remarkable feature of the chemical pressure working in opposite direction to an externally applied hydrostatic pressure.

Studies of the electronic band structure are very important for understanding the nature of the interplay between different ground states in these compounds. In contrast to the structurally similar sister compounds [47, 48, 49], magneto-quantum oscillation experiments had failed to provide conclusive evidence for a well-defined FS existing at the ambient pressure for the κ -Br salt at the beginning of this work. Positron annihilation experiments [50] at room temperature could not confirm the FS prediction, either. This was attributed to a shortcoming of the theoretical calculation of the electronic structure or of the positron wavefunction, needed for the interpretation of the experimental results. Magnetotransport experiments under high pressure [34] revealed SdH oscillations but indicated considerable deviations from the theoretically predicted FS.

With the aim to obtain more detailed information about the electronic structure in the vicinity of the FS in κ -Br, magneto-quantum oscillation experiments were carried out on this compound in the present work.

4.1.1 Synthesis

All the κ -(BEDT-TTF)₂Cu[N(CN)₂]Br crystals employed for the experiments performed in this study were produced by N. Kushch (Institute for Chemical Physics Research, Chernogolovka, Russia). Ph₄P[N(CN)₂] (60.75 mg) and CuBr (21.53 mg) were solved in a mixture of 1,1,2-trichloroethane (27 ml) and ethanol (3 ml). BEDT-TTF (25 mg) was then electrolyzed in the presence of this suspension with Pt-electrodes at a current density of 1 μ A/cm² and a temperature of 293 K for 3 - 4 weeks. At the anode, black single crystals of a typical size of $\sim 0.7 \times 0.3 \times 0.7$ mm³, with the largest face lying parallel to the (*ac*)-plane, were grown.

The data presented in this work were obtained on four samples of two different batches of production. Two samples of the same batch were used for SdH experiments, one of them being measured in two different series of experiments separated by a six-month time interval. Hereinafter, the first sample is referred to as sample #1 and the other as sample #2 and #2'. Two samples of another batch were used for dHvA and for simultaneous SdH and dHvA measurements, respectively. These samples are referred to as sample #3 and sample #4, respectively.

¹In organic conductors the screening due to electron charges is usually much lower than in ordinary metals, and the electron-electron correlation effect dominates. This leads to a strong (compared to the bandwidth W) on-site Coulomb energy U . Electrons thus tend to be localized on each lattice site to avoid the Coulomb repulsion. As a result, the system may have an insulating ground state, called the Mott insulating state.

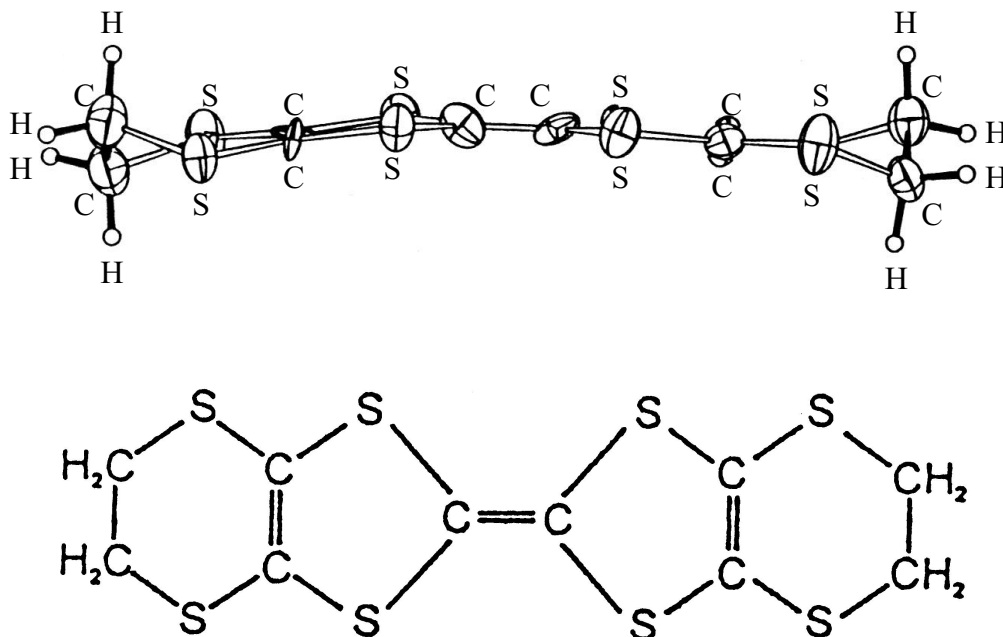


Figure 4.2: Molecular shape of the BEDT-TTF molecule in κ -(BEDT-TTF)₂Cu[N(CN)₂]Br (staggered form). The top (bottom) figure gives the view in the direction parallel (perpendicular) to the central tetrathiafulvalene plane [40].

4.1.2 Crystal Structure

κ -(BEDT-TTF)₂Cu[N(CN)₂]Br crystallizes in an orthorhombic structure with eight BEDT-TTF molecules (Fig. 4.2) per unit cell (space symmetry Pnma) [51] (Fig. 4.3). The lattice parameters, derived from an X-ray analysis at room temperature, are $a = 12.949 \text{ \AA}$, $b = 30.016 \text{ \AA}$, and $c = 8.539 \text{ \AA}$. The volume of the unit cell amounts to $v = 3317 \text{ \AA}^3$ [52].

In general, for every (BEDT-TTF)₂X salt the BEDT-TTF molecules can crystallize in different orientations against each other. The packing motifs of these donor molecules are distinguished in several so-called phases which are denoted by a Greek letter as a prefix to the formula of the compound.

(BEDT-TTF)₂Cu[N(CN)₂]Br only exists in the κ -phase which is characterized by two BEDT-TTF molecules paired with their central tetrathiafulvalene planes approximately parallel to each other to form dimers. Adjacent pairs are packed in almost orthogonal order [Fig. 4.4(a)] with the consequence that the interdimer interaction nearly equals the intradimer interaction. The BEDT-TTF layers alternate with sheets of Cu[N(CN)₂]Br anions. The latter consist of planar triply-coordinated Cu(I) atoms with two bridging dicyanamide [(NC)N(CN)]⁻ ligands forming a zig-zag chain along the a -axis in the (ac)-plane [Fig. 4.4(b)]. The terminal Br⁻ ions represent the third coordination site at each Cu(I) atom. Due to the alternate tilting of the BEDT-TTF molecules along the b -axis, the unit cell contains two donor and two acceptor layers.

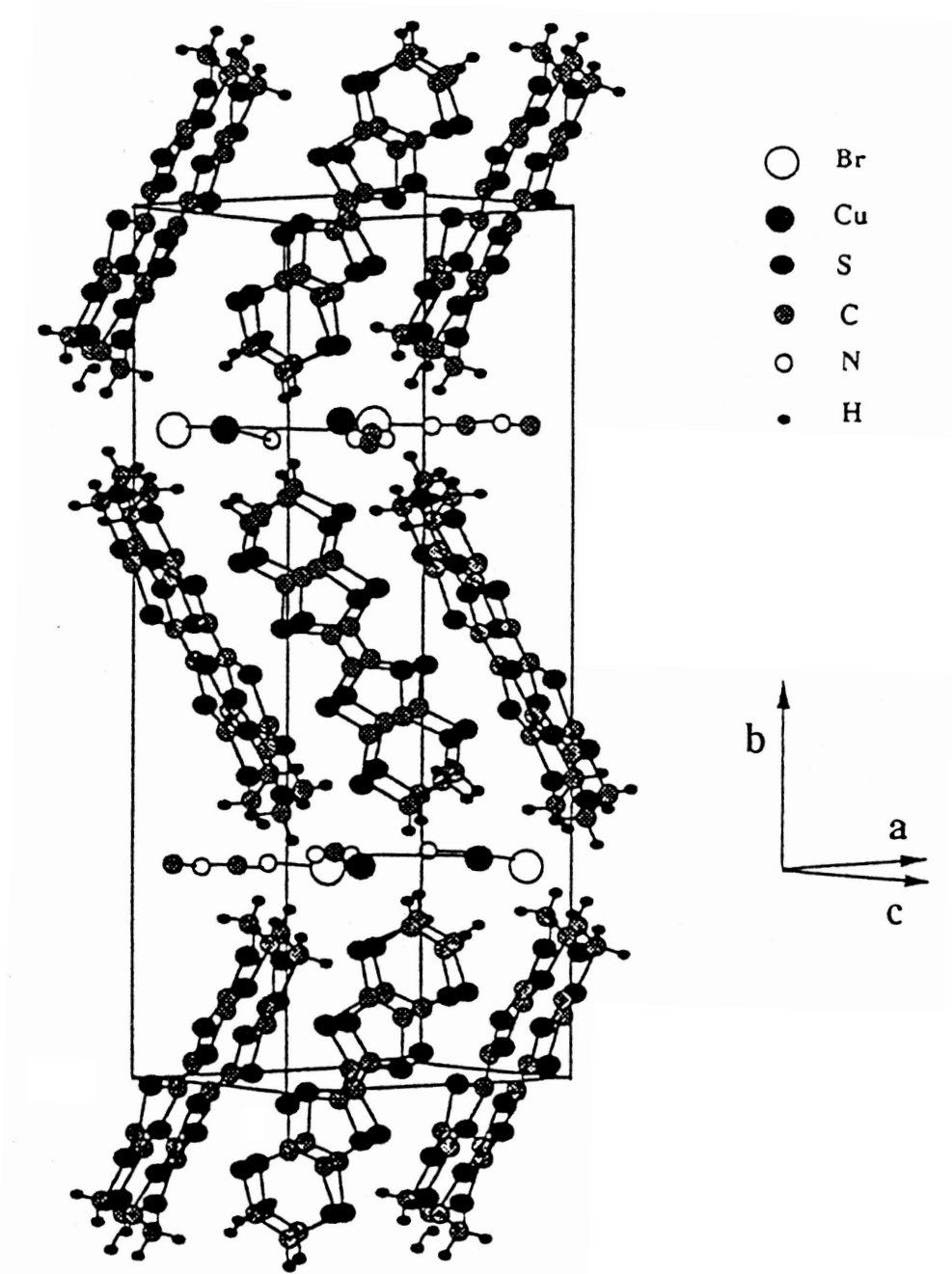


Figure 4.3: Crystal structure of κ -(BEDT-TTF)₂Cu[N(CN)₂]Br taken from Ref. [53].

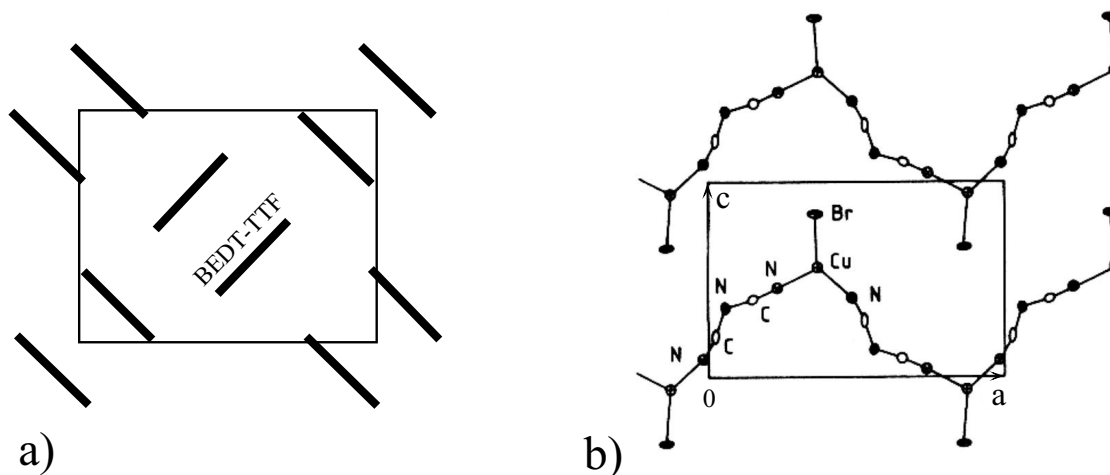


Figure 4.4: (a) Sketch of the packing pattern of the BEDT-TTF molecules within a donor layer of the κ -(BEDT-TTF)₂X compounds, viewed along the molecular long axis. (b) Structure of the X = Cu[N(CN)₂]Br anions in the (ac)-plane [52].

The sp^3 hybridization of the carbon atoms of the two terminal ethylene groups, $(CH_2)_2$, of the BEDT-TTF molecules allows two stable configurations of these groups: *staggered* and *eclipsed*, depending on the relative orientation of the outer C-C bonds. As the activation energy between these conformations is small, the motion between the two positions is very fast at room temperature, whereas at lower temperature, the ethylene groups freeze in an ordered eclipsed configuration [51, 52] (the same effect is observed in κ -Cl which adopts an eclipsed configuration [52] and in κ -NCS which takes a staggered ordering [54] but only partly in κ -(BEDT-TTF)₂Cu[N(CN)₂]I, where two groups are eclipsed for one staggered [52]). X-ray “monochromatic” Laue type photographic investigations [55] revealed the formation of a superlattice that doubles the crystallographic c parameter at temperatures lower than about 200 K. Such an effect has not been observed in other structurally similar salts, such as κ -Cl, κ -NCS, κ -(BEDT-TTF)₂Cu(CN)[N(CN)₂], and κ -(BEDT-TTF)₂I₃. The origin of this superlattice could not be elucidated, so far. Measurements of the nuclear relaxation rate, T_1^{-1} , by ¹H nuclear magnetic resonance (NMR) on single crystals suggested a freezing of the ethylene motion at around 200 K [56], i.e., at the temperature range where the superlattice formation takes place. It is not clear whether both phenomena are related to each other, but it was proposed that the structural modification caused by the ethylene ordering may help to stabilize the superstructure [55]. It has to be noted that ethylene ordering was put forward as a possible explanation for other observed features as well. Namely for an anomalous jump in the thermal expansion coefficient associated with the (ac)-plane [57] and a dip in the electrical resistivity [58, 57, 59] that were both observed at 80 K. Recent resistance relaxation studies on κ -Br and its deuterated analog revealed first-order phase transitions in the relaxation time as a function of annealing temperature at around 64 K and 80 K as well as a minimum in the superconducting transition temperature on annealing at around 170 K [60].

A comprehensive explanation of these results and the above mentioned phenomena [55, 56, 57, 58, 59] is proposed in terms of a transformation sequence predicted for ethylene ordering [61].

4.1.3 Electronic Structure

In order to understand the metallic properties, exhibited by most of the BEDT-TTF based compounds in the normal state, one has to start from the molecular orbitals of the isolated BEDT-TTF molecule. Upon forming rings composed of S and C atoms the *s*- and *p*-atomic orbitals hybridize to form σ and π molecular orbitals. While the σ orbitals are localized along the bonding axes, the π orbitals are extended normal to the molecular planes. Owing to their low binding energy, the π electrons are easily delocalized, thus enabling the charge transfer process. Since, along certain directions, the distance between S atoms of two neighboring BEDT-TTF molecules is less than the sum of the van der Waals radii of two S atoms, the π orbitals of the partly filled outer molecular shells overlap so that discrete energy levels of the individual molecules spread out to form energy bands. Provided that the intramolecular electron repulsion is smaller than the resulting bandwidth, the partially filled bands can thus lead to a metallic conductivity. The negatively charged anions that are sandwiched between the BEDT-TTF layers adopt a closed-shell configuration and do hardly contribute to the electrical conductivity. This entails a highly anisotropic conductivity that is responsible for the designation of these compounds as *quasi-two-dimensional* conductors.

The calculation of the band structure from first principles is complex, sensitive to the computation procedure, and limited by computer capabilities. A rather simple but very successful approach to calculate the band structure of the organic charge-transfer salts is a two-dimensional tight-binding calculation, within the extended Hückel molecular orbital approximation ([62, 63, 64] and Refs. therein). In this model, the molecular orbitals for the isolated BEDT-TTF molecules are calculated using semi-empirical molecular parameters. They are constructed by linear combinations of the atomic orbitals of the constituent atoms. For the further treatment, usually only the highest (lowest) occupied (unoccupied) molecular orbitals of the donor (acceptor) molecule, i.e., the π orbitals, are considered. Using structural data, the electron transfer energies are deduced from the overlap integrals. By means of a standard tight-binding calculation the band structure and FS can be determined. With the initial approximation of non-interacting conducting layers separated by insulating sheets, hence neglecting any interlayer electron transfer, the FS is strictly two-dimensional and exhibits no dispersion along the interlayer direction.

Fig. 4.5 displays the energy dispersion of κ -Br in the vicinity of the Fermi level [42], derived from tight-binding calculations. Between the second and third bands a clear band-gap exists indicating that the higher two and lower two bands are due to the anti-bonding and bonding orbitals within the dimers, respectively. The conduction band is three-quarters filled, as there is one hole per two BEDT-TTF molecules, each of which can accommodate two electrons.

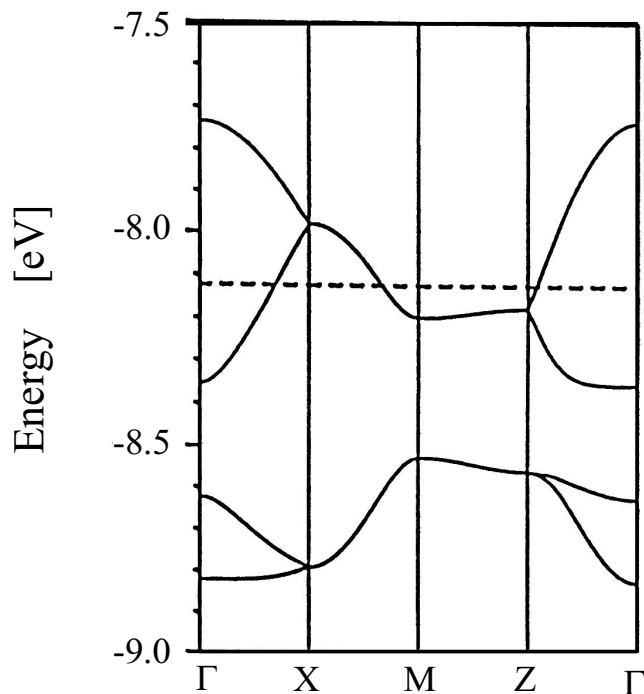


Figure 4.5: Calculated energy bandstructure of κ -(BEDT-TTF)₂Cu[N(CN)₂]Br near the Fermi level (dashed line) [42].

The FS resulting from this band structure is presented in Fig. 4.6 [42]. It consists of two open, slightly warped electron-like sheets normal to the k_c -axis and a cylindrical hole-like surface running along the k_b direction, whose elliptical cross-sectional area is centered at X. Owing to the structural similarity, the FS shape closely resembles to that predicted for other κ -(BEDT-TTF)₂X systems such as the κ -Cl [65] and κ -NCS [47]. Since the latter salt exhibits a monoclinic crystal structure it lacks a center-of-inversion symmetry, that lifts the degeneracy and makes a small gap open up at the first Brillouin zone (BZ) boundary. This mechanism is not present in the κ -Br and κ -Cl salts with an orthorhombic structure; however, in reality, gaps can be expected to exist also in these compounds, but of considerably smaller size than in the κ -NCS.

According to the calculations, two main contributions should appear in magneto-quantum oscillations in κ -Br.

(i) Oscillations of a frequency corresponding to the area enveloped by the closed orbit. This orbit encompasses $\simeq 14\%$ of the first BZ cross-sectional area and, by convention, is called α orbit.

(ii) High-frequency oscillations with a frequency corresponding to an orbit enclosing the area equal to 100% of the first BZ cross-sectional area. This orbit, usually called β orbit, is due to MB enabling the electrons to overcome the gaps at the BZ boundary in sufficiently high magnetic fields. For the case of negligible in-plane anisotropy, it has a perfect circular shape. Due to an extremely high anisotropy of

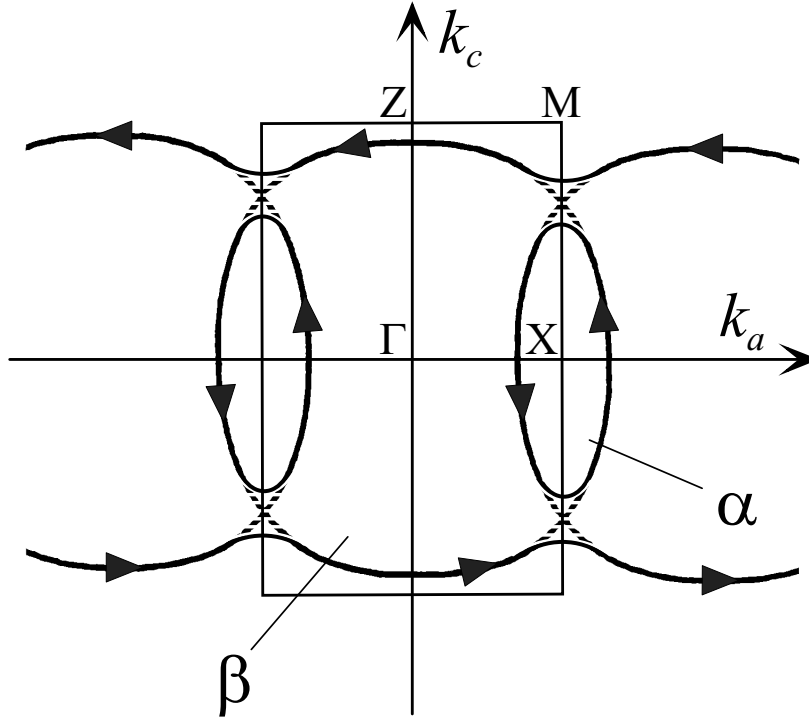


Figure 4.6: Computed Fermi surface of κ -(BEDT-TTF)₂Cu[N(CN)₂]Br [42]. Due to inversion symmetry of the orthorhombic crystal structure, band structure calculations yield no gap at the Brillouin zone boundary along X-M (dashed line). In reality, a gap can be expected to open up (considerably exaggerated for clarity). The arrows indicate possible electron motions on the α and β orbits for a magnetic field pointing out of the plane.

the FS, the quasi-two-dimensional metals based on BEDT-TTF exhibit a strong enhancement of the MB manifestation. Since the transverse bandwidth is expected to be much smaller than the MB gap, the MB orbit likely gives the dominating contribution to magneto-quantum oscillations.

In remarkable agreement with the theoretical calculations [47, 65], both orbits have been experimentally confirmed in numerous studies of the κ -NCS salt in a magnetic field (see, e.g., [66] for a review) as well as in the Shubnikov-de Haas (SdH) experiment on the κ -Cl salt in the metallic state (under pressure $p \geq 2$ kbar) [49, 67]. However, at the beginning of the present work, no SdH oscillations had been observed in the κ -Br at ambient pressure. Weak oscillations attributed to the MB β orbit were found only under high pressure, $p \approx 9$ kbar [68]. These oscillations were superimposed on very low-frequency oscillations that were observed down to 10 T, also at high pressures [34]. Strikingly, the low frequency could not be readily attributed to the normal α orbit, since it was found to be by almost a factor of four lower than it would be expected from the area enclosed by the predicted α pocket [42]. Considering theoretical [65] and experimental [49, 69] results for the pressure dependence of the band structure of the κ -salts, it turns out that, in the case of a smoothly varying FS with pressure, an exceptionally small size of the α

orbit could be caused only by an unusually high sensitivity of the Fermi surface to the pressure. A possible reduction of the α orbit size was therefore held to be more likely driven by a phase transition induced by the pressure or the low temperature. This could modify the Fermi surface which is calculated for ambient pressure and room temperature.

Furthermore, the amplitude of the SdH oscillations reported in Refs. [34, 68] is by two orders of magnitude smaller than those found in the other κ -salts. As argued in Ref. [34], this weak amplitude can unlikely be caused by a simply higher concentration of mechanical defects.

The origin of such unexpectedly large discrepancies was not clear at the time of the first experiments. It thus rose the question about the validity of the extended Hückel method for calculating the band structure and FS for κ -Br [42] even for qualitative predictions. The available data were very restricted at that time. Only one study had been reported which dealt with the slow oscillations [34] and only one in which the observation of the rapid oscillations was announced [68]. At ambient pressure no oscillations had been seen at all. These data did not allow to make any clear conclusion with regard to the Fermi surface. Therefore it was highly desirable to continue these studies and especially tempting to search for magneto-quantum oscillations also at ambient pressure.

In order to clarify the uncertainties and to obtain a clear description of the electronic state in κ -Br, magnetic torque and magneto-transport studies have been performed in this work under various conditions. Although the present study was started by carrying out extensive magneto-transport experiments, the following presentation and discussion of the experimental results begins with magnetization measurements since they turned out to allow for a more detailed description of the electronic system.

4.2 de Haas-van Alphen Measurements

In this section the first torque measurements that have been successful in observing dHvA oscillations in the κ -Br salt [70], are presented. They were carried out with the highly conducting (*ac*)-plane of the κ -Br crystal parallel to the cantilever plate of the torquemeter. The angle θ between the direction normal to the (*ac*)-plane and the field \vec{B} was varied in the range $-42^\circ \leq \theta \leq +51^\circ$. The position $\vec{B} \perp (ac)$, i.e., $\theta = 0^\circ$, was explicitly determined by minimizing the torque signal in the superconducting field range. All experiments were performed in magnetic fields up to 28 T provided by a 20 MW resistive magnet.

4.2.1 dHvA Oscillation Frequencies

Fig. 4.7 shows some representative examples of the torque signal after subtraction of the steady background. Oscillations become visible starting from $\simeq 19$ T at the lowest temperature, $\simeq 0.4$ K. Already in the raw curves, it is seen that the oscillations exhibit a dominant high frequency modulated by a weaker low frequency.

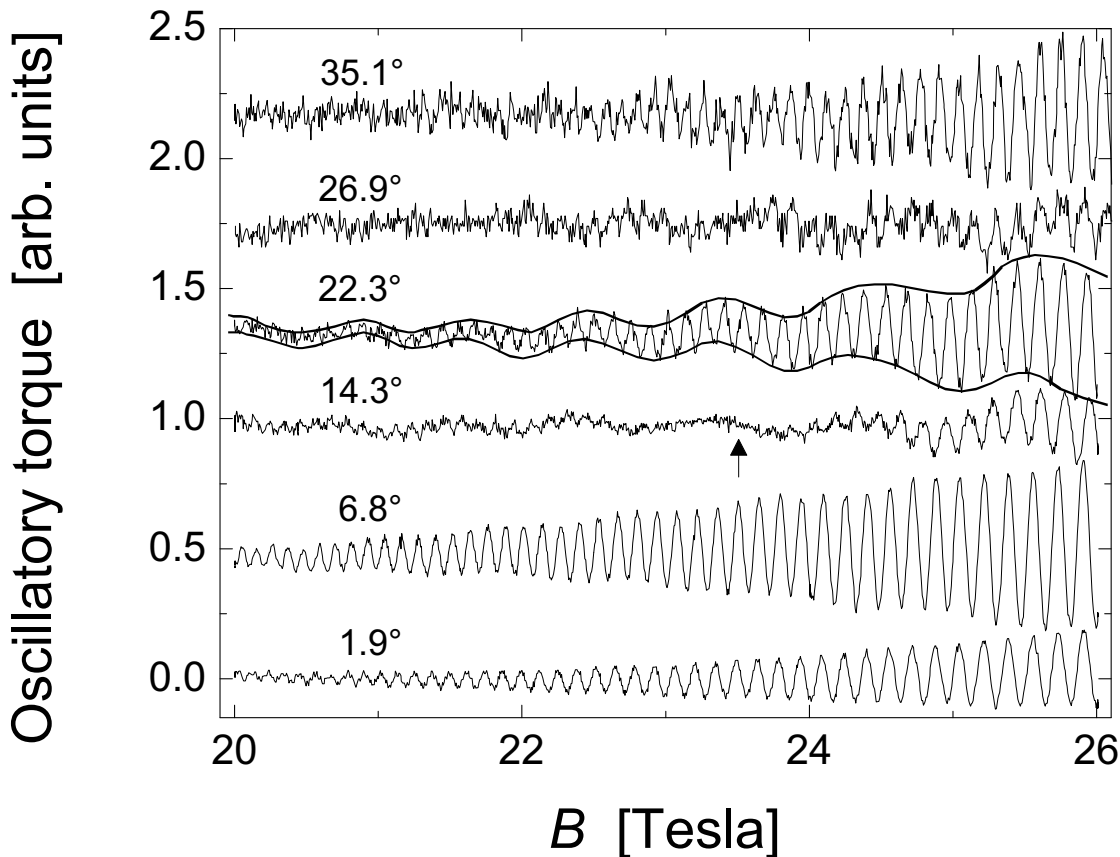


Figure 4.7: Torque signal at several angles θ , after subtraction of the slowly varying background. The line enveloping the curve for $\theta = 22.3^\circ$ is drawn to emphasize the α oscillations. The arrow points to the node in the beating β oscillations at $\theta = 14.3^\circ$.

As the usual procedure for the exact analysis of the oscillation frequencies a fast Fourier transform (FFT) was performed in the inverse magnetic field scale (Fig. 4.8). As an additional check of this procedure, for some curves the number of every oscillation period (which follows the Landau level index n) was plotted versus the inverse magnetic field (Fig. 4.9). The slopes of the resulting curves are equal to the oscillation frequencies and their deviation from a straight line provide a precise estimate for the error made in the frequency determination.

Two frequencies can be detected, as indicated in the FFT spectra in Fig. 4.8. The low frequency, $F(\theta = 0^\circ) = 530 \pm 5$ T, corresponds to a FS orbit enclosing $\approx 14\%$ of the first BZ cross-sectional area. It can be readily identified as the α orbit on the closed part of the FS (Fig. 4.6), in excellent agreement with tight binding band calculations [42]. The presence of the α pocket was experimentally confirmed since long for the sister compounds κ -Cl [49] and κ -NCS [47] but still matter of discussion for the κ -Br. This finding [70] thus gives the first evidence of the existence of the closed α orbit in this compound and proves the validity of

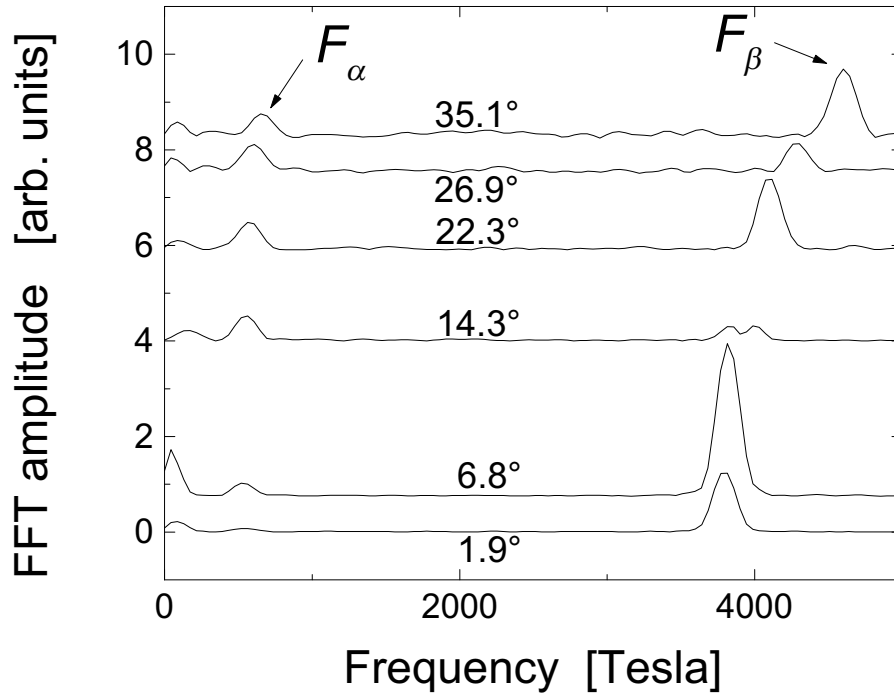


Figure 4.8: FFT of the curves shown in Fig. 4.7. The transformation is performed over a field interval 20 T to 26 T. The curves are offset for clarity.

the tight-binding band structure calculations for the present system. The rapid oscillations exhibit a frequency of $F(\theta = 0^\circ) = 3790 \pm 10$ T which corresponds to the first BZ area and is thus equivalent to the area enclosed by the MB β orbit. It was previously observed in magnetotransport experiments, first under pressure [68] and afterwards also at ambient pressure [71, 72] (see section 4.3). The coexistence of the two frequencies, F_β and F_α , suggests that the FS is indeed similar to those found in the sister compounds κ -Cl [49] and κ -NCS [48, 73]. However, the relative intensities of the oscillations found in the κ -NCS are markedly different from that in the κ -Br. In the case of the former, the high frequency oscillations appear at the threshold field for MB around 20 T superimposed onto the strongly dominating low frequency oscillations. In the κ -Br the β oscillations are more pronounced than the α oscillations already at the lowest fields where oscillations are visible. Thus, we can presume the present system to be in a strong MB regime in the studied field range. This is in agreement with band structure calculations predicting an energy gap existing between the open sheets and the closed orbits of the FS in the κ -NCS salt [47] but no or only a negligible gap which is easily overcome by MB, for the κ -Br [42] and κ -Cl [65].

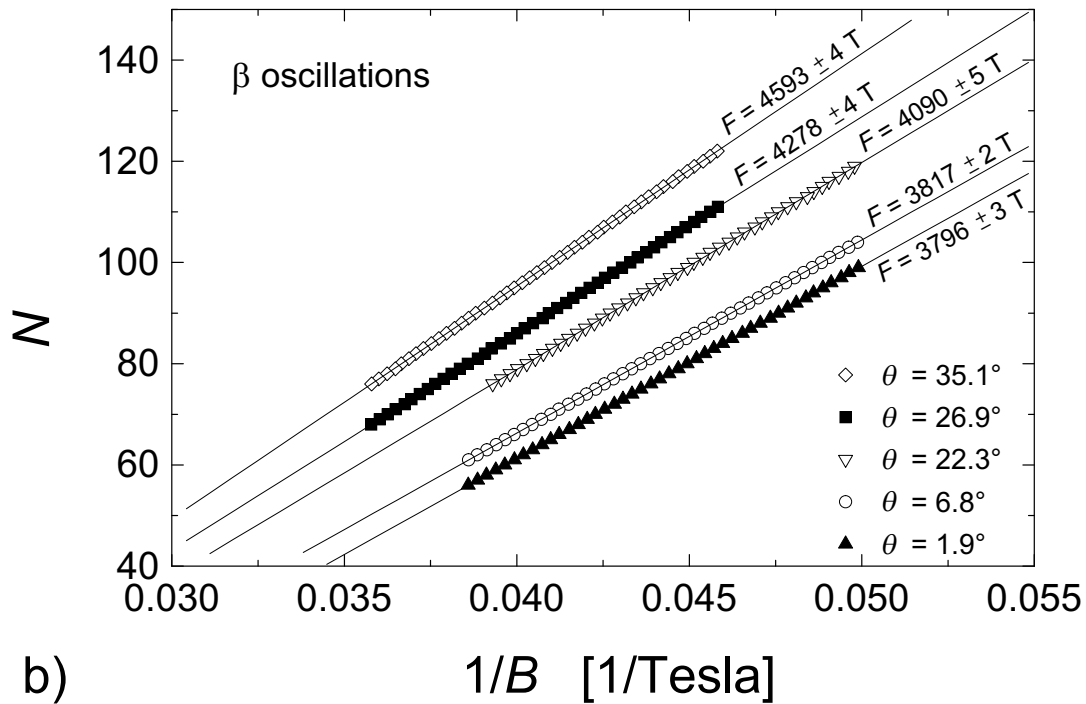
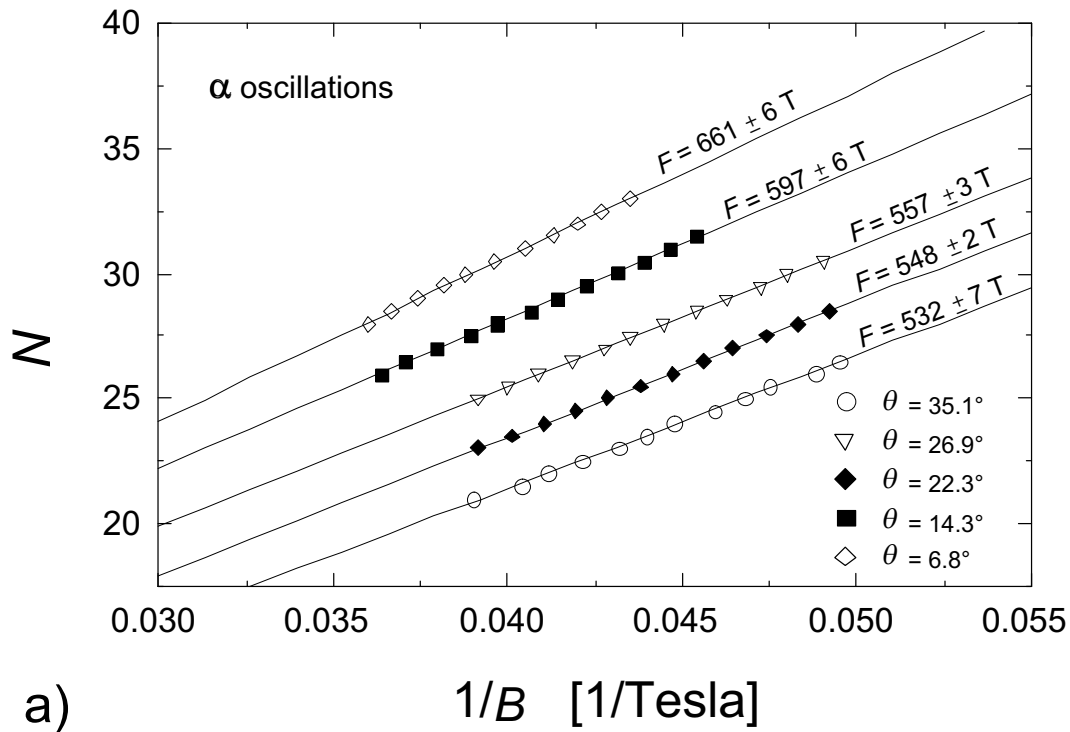


Figure 4.9: Index of the oscillation period for (a) α and (b) β oscillations. The slopes of the curves directly yield the oscillation frequencies. The curves are offset for clarity.

4.2.2 Angular Dependence of dHvA Oscillation Frequencies - Beating Effect

Magneto-quantum oscillations of the magnetization are observed at angles θ up to 42.5° for the α oscillations and up to 51° for the β oscillations. At higher angles, the amplitudes become lower than the resolution of the experiment. Within the measured range, both frequencies follow an angular dependence of $F \propto 1/\cos\theta$ (Fig. 4.10). This behavior is characteristic of a cylindrical FS which is found in two-dimensional systems. However, due to the error in the frequency determination, this result does not allow to rule out possible deviations from an ideal cylindrical shape of the FS that are smaller than $\Delta S/S \sim 2\%$, where ΔS is the variation of the cross-sectional area, S , along the axis of the FS cylinder.

At angles $12^\circ \leq \theta \leq 16^\circ$, distinct beating of the high-frequency dHvA oscillations is observed [70]. This is illustrated by the curve at $\theta = 14.3^\circ$ in Fig. 4.7: it shows a node in the β oscillations at $B \approx 23.5$ T. In principle, this feature could be caused by a bicrystalline structure of the sample. In this case, the sample would consist of two crystals which are tilted against each other by a few degrees. For non-symmetric field orientations, this leads to two different effective areas enclosed by the carrier orbits of both crystallites and thus to two slightly different oscillation frequencies that interfere with each other. For certain magnetic field strengths and angles θ , the oscillation amplitude would then have a minimum due to destructive interference. However, the examination of all the samples, used for the experiments, under an optical microscope did not reveal any obvious regular bicrystalline structure. An X-ray crystallographic analysis [74] performed on one of the samples could not provide unambiguous information about the entire volume of the crystal, since the sample was too big to allow for a penetration of the X-ray deep into the bulk. Besides some non-systematic orientational disorder, the X-ray analysis of the crystal surface did not show any considerable defects that could be responsible for a frequency splitting. A convincing argument against the existence of a bicrystalline structure is given by the fact that the same data were obtained on two samples and the node appeared symmetrically at positive and negative angles around $\pm 14^\circ$. A more likely reason for the beating behavior is therefore a slight warping, i.e., a corrugation of the FS cylinder in the direction perpendicular to the (ac) -plane (Fig. 4.11). This FS geometry originates from a finite coherent electron transfer in the transverse direction to the highly conducting layers of the crystal, that slightly increases the dimensionality of the system and can be described by the energy dispersion [75]

$$\epsilon_k = \frac{\hbar}{2m_{band}^\beta} (k_x^2 + k_y^2) - 2t_\perp \cos(\mathbf{h}\mathbf{k}). \quad (4.1)$$

For simplicity, the in-plane FS β orbit is assumed to have an ideal circular shape and to be occupied by electrons of the band structure effective mass m_{band}^β . $\mathbf{h} = (u_x, u_y, b')$ is the direction vector of the interlayer transfer energy t_\perp , and b' is the spacing between neighboring highly conducting layers. A qualitative picture of this corrugated FS cylinder for the case $u_x, u_y = 0$ m is shown in Fig. 4.11. In this

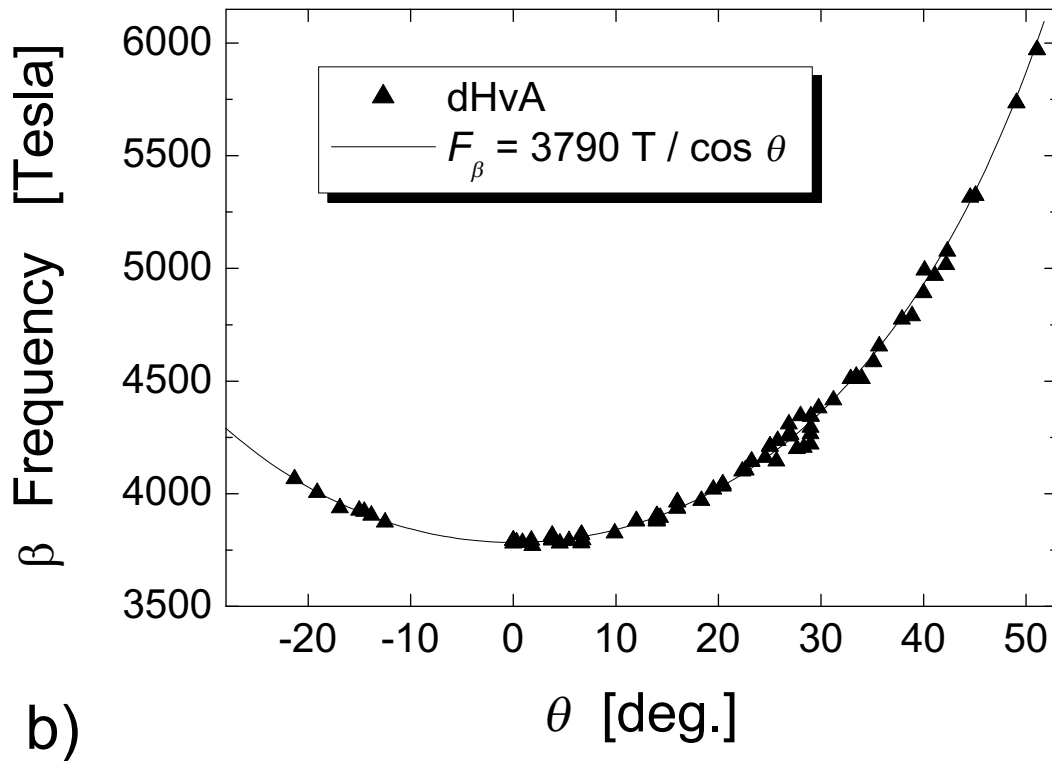
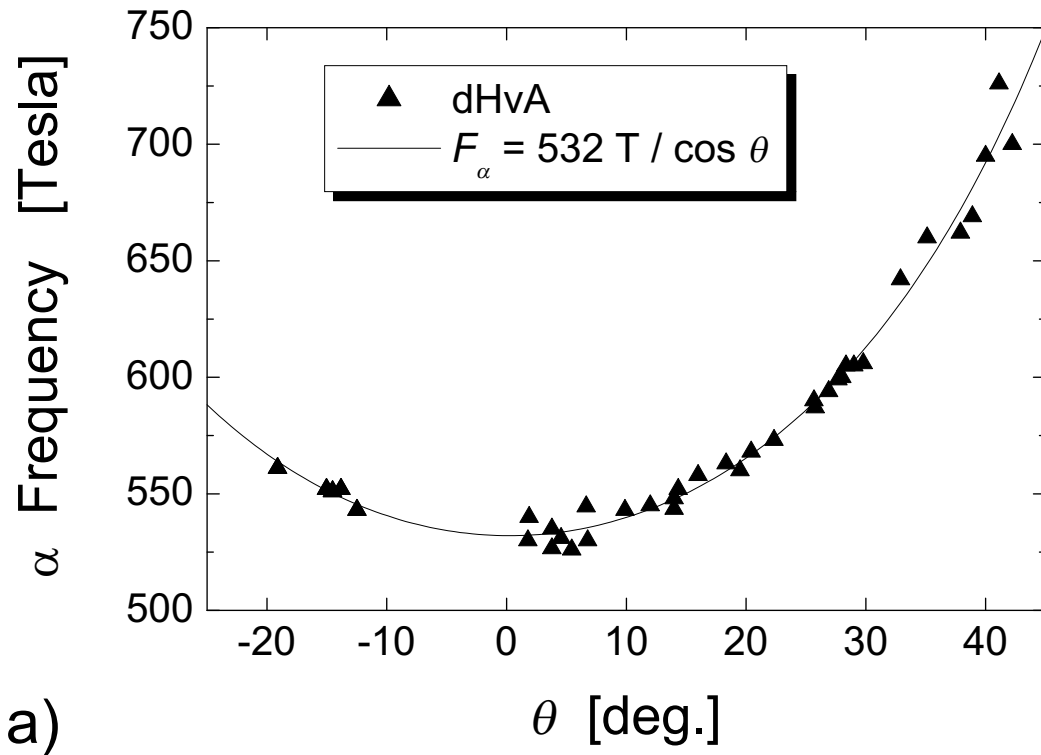


Figure 4.10: Angular dependence of (a) α and (b) β oscillation frequencies. Both follow a $1/\cos\theta$ behavior.

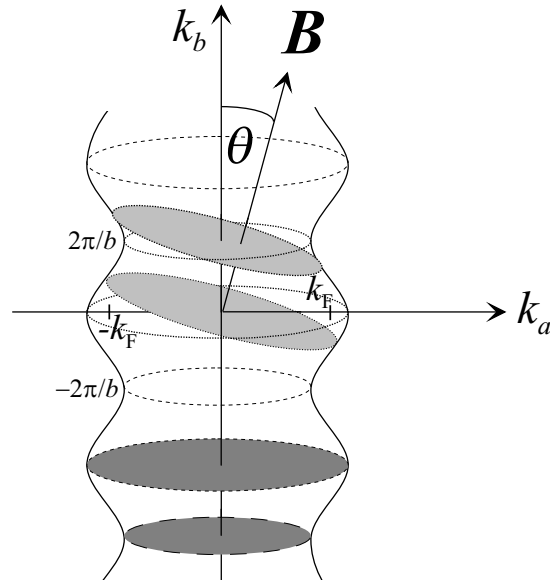


Figure 4.11: Schematic view of the warping of the β orbit cylinder. The dark shaded lower two areas are enveloped by the extremal electron orbits for the magnetic field direction parallel to the cylinder axis; the upper two areas for the field tilted by the angle θ .

situation, the two cross-sectional areas of maximum and minimum size contribute to quantum oscillations with slightly different frequencies, F and $F + \Delta F$. Taking into account that in the limit $1/B \rightarrow 0$ the phase constants in Eq. (2.9) amount to $-1/4\pi$ for the maximum cross-sectional area and $+1/4\pi$ for the minimum cross-sectional area [9] the oscillations are modulated by the function $\cos(\pi\Delta F/B - \frac{\pi}{4})$. The fact that the dHvA amplitude observed in the present experiment does not exactly vanish at the node position in the magnetic field, B_{node} , hints to slightly different contributions from the maximum and minimum cross-sections of the FS. This could be due to different Dingle temperatures or effective masses associated with the respective orbits.

According to the modulation function, the condition for the node position in the magnetic field may be written as

$$B_{node} = \frac{4\Delta F}{4n + 3}, \quad n = 0, 1, 2, \dots \quad (4.2)$$

In the experiment, the node appears at the highest fields at the angle $\theta \simeq 12^\circ$, shifts down to low fields with increasing angle and finally can no more be resolved due to the vanishing oscillation amplitude below 19 T for angles $\theta > 17^\circ$. Using the experimentally obtained node positions, B_{node} , and taking $n = 0, 1$, and 2, possible values for $\Delta F(\theta)$ are estimated as shown in Fig. 4.12.² Noteworthy, although

²Since only one node is observed in the available field interval, the beat frequency ΔF cannot be determined by simply measuring the distance between two subsequent nodes.

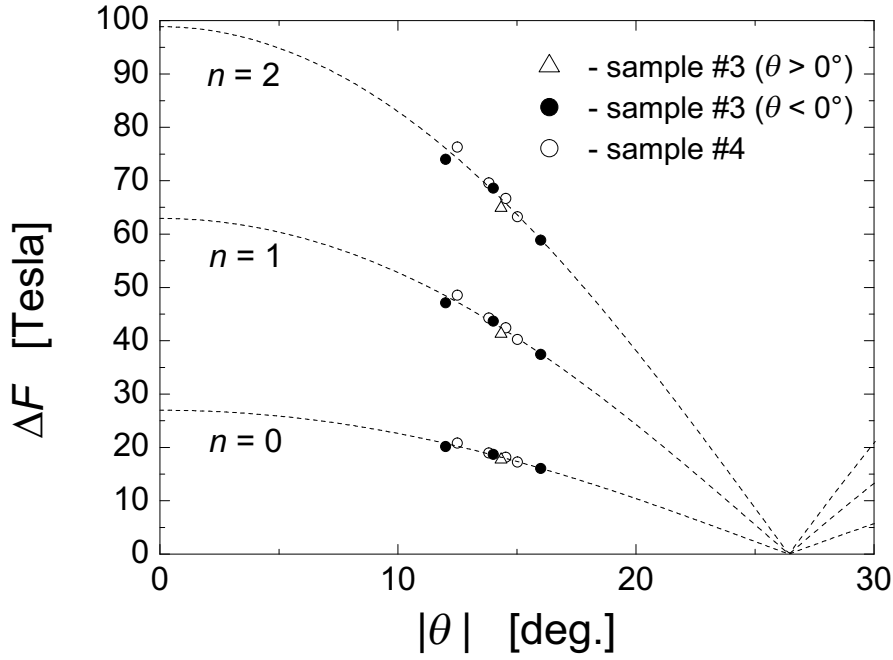


Figure 4.12: The beat frequency, ΔF , derived from the node position using Eq. (4.2) for $n = 0, 1, 2$, as a function of the tilt angle. The dashed lines are fits to the experimental data by Eq. (4.3).

the fundamental frequency grows with angle, $F_\beta \propto 1/\cos\theta$, the beat frequency *decreases* with increasing angle θ . This is a good illustration of the so-called Yamaji's effect [75] which predicts that the difference between the extremal cross-sections of a slightly warped FS oscillates with the angle, vanishing at certain field directions. The dashed lines in Fig. 4.12 represent fits to the oscillating angular dependence of the beat frequency [75],

$$\Delta F(\theta) = \Delta F(0^\circ) J_0(b'k_F \tan\theta) / \cos\theta, \quad (4.3)$$

where J_0 is the zeroth order Bessel function, $b' = b/2 \approx 1.48$ nm is the interlayer distance [42, 57] and k_F is the in-plane Fermi wave vector. The fits yield $k_F = 3.28 \cdot 10^7 \text{ cm}^{-1}$ which is a reasonable value, taking into account the area of the β orbit, $S_\beta = 3.6 \cdot 10^{15} \text{ cm}^{-2}$. The error for the value of k_F , revealed by the fits, amounts to $\Delta k_F = 0.13 \cdot 10^7 \text{ cm}^{-1}$ and is much smaller than the possible error caused by the deviation of the FS orbit at $\theta = 0^\circ$ from an ideal circle.

According to the fits, the lowest possible frequency difference between the maximum and minimum orbits amounts to $\Delta F_\beta(0^\circ) = 27$ T at $\theta = 0^\circ$. For this beat frequency, the first node (coming from high fields), $n = 0$, is observed and the next one, $n = 1$, would be expected at fields below 15.4 T (solid lines in Fig. 4.13). If the beat frequency would amount to the next higher value $\Delta F_\beta(0^\circ) = 63$ T, then the node observed in the experiment would be already the second one, with $n = 1$. In this case, the first node, $n = 0$, would shift through the field interval which allows for the detection of a possible node, at around the angles $\theta = 21^\circ$,

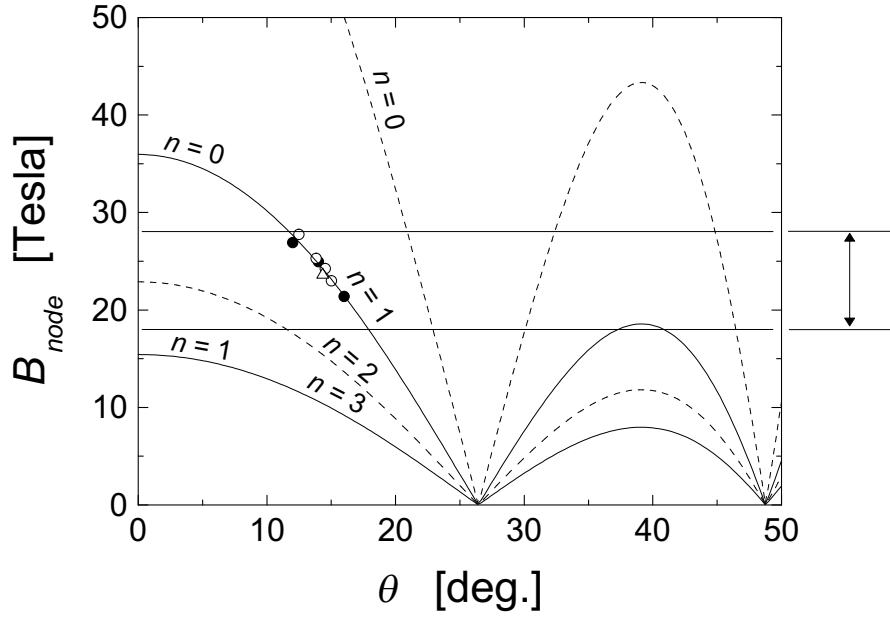


Figure 4.13: Position of the node in the magnetic field, derived from Eq. (4.2) and (4.3). The set of values n to the left (right) refers to the beat frequency $\Delta F = 27$ T ($\Delta F = 63$ T). The horizontal lines demonstrate the upper and lower limit for the detection of the node.

30° , and 45.5° . In contrast to this calculation, no node was observed in these angular regions. This could be due to the very steep slopes of $B_{node}(\theta)$ for this node, that require a very narrow angular scanning for its detection. The third node, $n = 2$, however, should be clearly seen at angles up to $\theta = 10^\circ$. Since, in spite of a thorough angular scanning, no node has been detected also in this range, it is concluded that the observed node originates from a beat frequency $\Delta F_\beta(0^\circ) = 27$ T and is characterized by $n = 0$ in Eq. (4.2). Using this frequency difference, the variation of the β orbit area over the FS is estimated as $\Delta S_\beta/S_\beta = 0.71\%$. Expressed in terms of energy, this variation corresponds to an interlayer bandwidth $W_\perp = \epsilon_F \Delta F_\beta(0^\circ)/F_\beta(0^\circ) \approx 7 \cdot 10^{-3} \epsilon_F$. Taking account of Eq. (4.1), this result allows to estimate the interlayer transfer energy as $t_\perp = W_\perp/4 \approx 2 \cdot 10^{-3} \epsilon_F$. With a Fermi energy of 0.06 eV the transfer energy is thus calculated to $t_\perp \approx 0.1$ meV. This value is by three orders of magnitude lower than typical values of the intralayer transfer energy [76, 77].

4.2.3 Effective Cyclotron Masses

The effective cyclotron masses, m^* , of the carriers on either orbit were determined by fitting the experimentally observed temperature dependence of the oscillation amplitudes to the LK formula (2.9)/(2.11). At least four field sweeps at roughly equally spaced constant temperatures in the range 0.4 K to 1.3 K were performed, respectively, for different orientations of the magnetic field. The amplitudes of

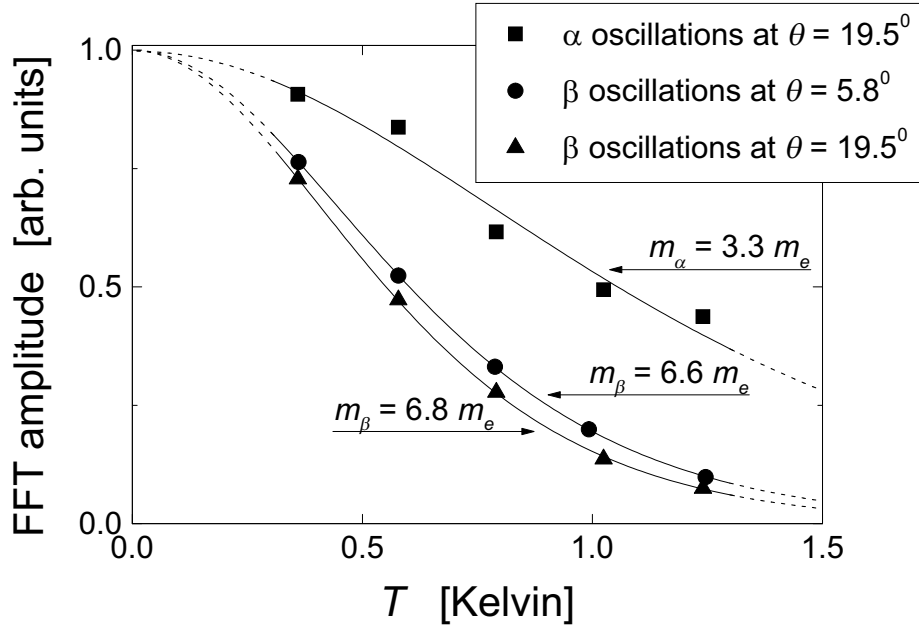


Figure 4.14: Temperature dependences of FFT amplitudes of the dHvA α and β oscillations along with the fits according to the LK formula (solid lines). The data are normalized to the amplitude extrapolated to 0 K.

the oscillations were estimated by taking the height of the corresponding peaks in the FFT which was performed in the same magnetic field interval for each temperature. The factor $1/B$ in the fitting function was taken as the average inverse magnetic field, $\overline{1/B}$, over this interval. This is assumed to cause no additional error if the interval is not too large. The error for the effective cyclotron masses yielded by the fits was estimated by the variation that was obtained by taking different field intervals. As a parallel method, for some curves, the amplitude was additionally measured directly from the envelope of the curve at a fixed field. Both methods revealed the same values within the error bars. A typical example for a fit obtained by the former procedure is presented in Fig. 4.14. As it is seen in these plots, the temperature dependence of the α and β oscillation amplitudes can be well described by the LK formalism. With the assumption of a $1/\cos\theta$ dependence for the effective cyclotron masses³ the corresponding values for $\theta = 0^\circ$ are estimated as $m_\beta^* = 6.6 \pm 0.2 m_e$ and $m_\alpha^* = 3.1 \pm 0.5 m_e$. The first result is consistent with the value obtained in the previous SdH experiments [81] (see section 4.3), but considerably exceeds that reported from pulsed field magnetotransport measurements by Mielke *et al.*, $m_\beta^* = 5.4 \pm 0.1 m_e$ [72]. Within the experimental error, it is the same as that obtained for the effective cyclotron mass associated with the β orbit in κ -NCS in SdH [48, 73, 69] and dHvA [82] measurements. A

³This assumption is made considering the $1/\cos\theta$ dependence of the oscillation frequencies that, in the first approximation, should be also reflected in the effective cyclotron masses. Systematic studies of the angular dependence of m^* in various organic superconductors have confirmed this behavior [78, 79, 80].

close similarity to this sister compound is also reflected in the value of m_α^* which is found to $m_\alpha^* \simeq 3.5m_e$ in the cited experiments.

4.2.4 Angular Dependence of the dHvA Oscillation Amplitudes

While the observed amplitudes of the α oscillations indicate a smooth angular dependence [Fig. 4.15(a)], those of the β oscillations vary by two orders of magnitude and exhibit distinct dips. This is demonstrated in Fig. 4.15(b) which shows the FFT amplitude of the β oscillations as a function of the tilt angle θ . The minimum around $\theta = 14^\circ$ is caused by the above discussed beating phenomenon. At $\theta = 27^\circ$, 41° , and 49° , the dHvA amplitude again exhibits local minima; however, here the oscillations do not show the beat-like behavior (see, e.g., the curve at $\theta = 26.9^\circ$ in Fig. 4.7). These minima at higher angles are most likely caused by the Zeeman spin-splitting of the Landau levels as described by the LK theory [Eqs. (2.14)/(2.15)]. The energy difference between spin up and spin down states of one Landau level depends only on the magnetic field strength and can thus be assumed to be angle-independent. The inter Landau level spacing, however, depends on the effective mass which, in two-dimensional systems, usually changes strongly with angle following the above mentioned $1/\cos\theta$ behavior. Since the value of m_β^* amounts to a few times the free electron mass, spin-zeros appear already at angles where oscillations are observable. The low oscillation amplitude (compared to the sister compounds), however, admits the detection of minima in the oscillation amplitude only up to the angle $\theta = 51^\circ$. For the sequence of three minima in this angular range, the spin-splitting factor is unambiguously described by $g^*m_\beta^* = (9.85 \pm 0.10)m_e/\cos\theta$. If we take the effective cyclotron mass m_β^* extracted from the temperature dependence of the quantum oscillation amplitude the spin g -factor g^* , renormalized by both carrier-carrier and carrier-phonon interactions, is estimated as 1.5 ± 0.1 . Within the experimental error bar this result is equal to that obtained for the κ -NCS salt [82]. The g -factors of both compounds would thus significantly deviate from the bare g -factor value $g \simeq 2$, as it is usually found in ESR experiments (see, e.g., Ref. [83] for the κ -NCS salt and Refs. [84, 85, 86, 87] for other compounds of the BEDT-TTF family). If we neglect any possible carrier-carrier interactions affecting the g -factor and assume $g_s = 2$, we would obtain a bare mass of $m_{b,\beta} = 4.9m_e$ and, according to the relation $m_\beta^* = m_{b,\beta}(1 + \lambda)$, a carrier-phonon coupling constant λ of about 0.34. This value would indicate a slightly stronger carrier-phonon coupling strength than found in the κ -NCS salt [82] and thus agree with the higher superconducting transition temperature T_c in the κ -Br compound. If we take the Debye temperatures $\Theta_D = 215 \pm 15$ K and 210 ± 15 K obtained by specific heat measurements for the κ -NCS [88] and κ -Br [89] salts, respectively, T_c may be estimated via the standard relation given by the BCS formalism, $T_c \simeq 1.13\Theta_D \exp(-1/\lambda)$. The results are $T_c \approx 9.6$ K for the κ -NCS and $T_c \approx 12.5$ K for the κ -Br compound. These estimates fit remarkably well to the values established in several works (see, e.g., [41, 42]) and may support the assumption that g^* is renormalized predominantly

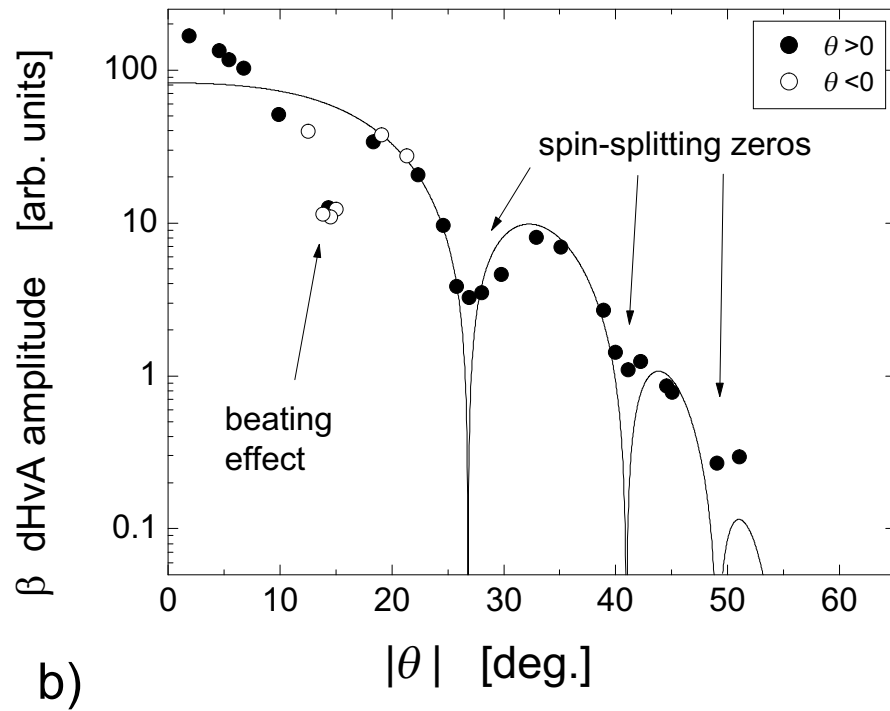
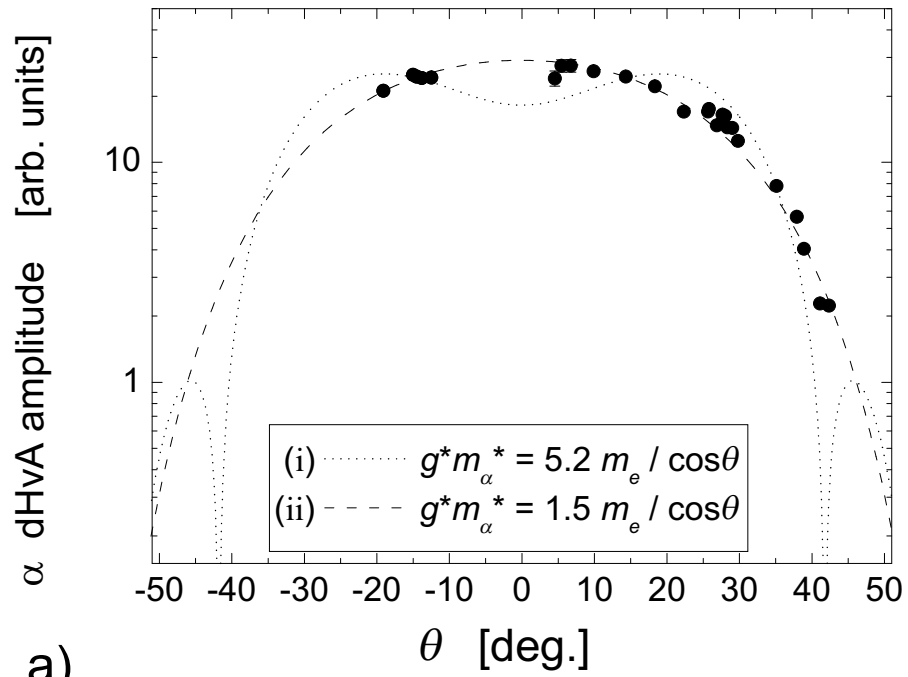


Figure 4.15: (a) Angular dependence of the FFT amplitude of the α oscillations. Two fits according to the LK formalism are shown (dotted and dashed lines). (b) Angular dependence of the FFT amplitude of the β oscillations along with the LK fit (solid line).

due to carrier-phonon coupling.

As it is seen in Fig. 4.12, the beat frequency ΔF_β is estimated to vanish at $\theta = 26.5^\circ$. At this angle, all electron orbits should enclose the same FS cross-sectional area, with the consequence that the Landau levels become extremely sharp and all electrons on the highest occupied level contribute to the oscillations. Therefore, one would expect the β oscillation amplitude to be strongly enhanced for this field orientation. However, it is nearly exactly at this angle that the first spin-zero is observed. A possible increase of the oscillation amplitude around $\theta = 27^\circ$ is thus masked by the obviously much stronger spin splitting effect.

As mentioned above, no minimum but a steady decrease of the angular dependence of the α oscillation amplitude was found up to $\theta = 42.5^\circ$. An unequivocal determination of the value for the spin-splitting factor associated with the α orbit is thus not possible. If we nevertheless tentatively fit the present behavior to the dependence predicted by the LK theory, we have to take into account two possible situations [Fig. 4.15(a)] [90]:

(i) A minimum at very small angles around $\theta = 0^\circ$ occurs in the α oscillation amplitude, which, however, could not be detected due to the vanishing sensitivity of the torquemeter for the magnetic field direction perpendicular to the highly conducting plane. In this case, the experimentally observed behavior may be best described by a spin-splitting factor of $g^*m_\alpha^* = (5.2 \pm 0.1)m_e/\cos\theta$ as fitting parameter. This value would be identical with that reported for the sister compound κ -NCS, $g^*m_\alpha^* = 5.2m_e/\cos\theta$ [82]. The analysis of this result carried out in the same way as for the β oscillations reveals the renormalized g -factor for the α orbit as $g^* = 1.68 \pm 0.10$ and, with the same assumption as made for g_s associated with the β oscillations, a carrier-phonon coupling constant $\lambda \approx 0.19$. These values are in the same range as those found for the electrons on the β orbit and as those reported for the κ -NCS salt, $g^* = 1.60 \pm 0.08$ and $\lambda = 0.27$ [82]. In particular the g -value is in fair agreement with these other results. Yet, especially at small angles there is a considerable discrepancy between this LK fit and the experimental data. Of course, even with consideration of all amplitude reduction factors, the LK formalism might not always perfectly describe the angular dependence of the oscillation amplitude [see also the small angle region in Fig. 4.15(b)]. The maximum discrepancy, however, exceeds the error associated with the determination of the oscillation amplitude by one order of magnitude and thus calls this tentative estimation of the spin-splitting factor into question.

(ii) The α oscillation amplitude actually goes down smoothly with increasing angle. For this situation, the experimental data can be perfectly fitted taking the fitting parameter $g^*m_\alpha^* = 1.5m_e/\cos\theta$. In order to get an upper limit of the spin-splitting factor we assume the first minimum to lie at the highest angle where the α oscillations could be still observed, $\theta \simeq 43^\circ$. In this case, $g^*m_\alpha^*$ takes the value $2.15m_e/\cos\theta$. If we again carry out the analysis detailed above, we come to a strongly reduced g -factor of ≈ 0.5 and a very high coupling constant $\lambda \approx 3$. The g -factors associated with the α and β orbits would thus differ from each other by a factor of about 3 or the coupling constants even by a factor of about 10. This situation would be markedly different from that found in the κ -NCS compound

[82], where the g -value and λ approximately do not depend on the type of the orbit.

Summarizing, due to the lack of a series of spin-zeros, the experimentally observed angular dependence of the α oscillation amplitude does only allow to narrow down the possible values for the actual data to two different scenarios. From the present data, it is not possible to definitely decide which of both cases, (i) or (ii), actually applies.

4.2.5 Dingle Temperature

The explicit determination of the Dingle temperature from the field dependence of the oscillation amplitude is particularly difficult in the present compound: First, the β orbit is associated with MB and the corresponding field dependent amplitude reduction factor (2.18) should thus be taken into account. The latter is largely determined by the FS topology and has to be evaluated from the field dependence of both, the α and β oscillations. For the present FS configuration, below the threshold field for MB⁴ only the α orbit should be seen in the oscillation spectrum, whereas above this field the intensity increase of the α oscillations with field is expected to be reduced in favor of that of the arising MB β oscillations. However, due to a low MB field and the weak oscillation amplitude which allows the observation of quantum oscillations only at fields above $\simeq 19$ T, the system is already in a MB regime within the available field range and the onset of the MB oscillations could not be detected. Hence, the value of B_0 remains unclear and enters the slope of the Dingle plot as an unknown parameter. Furthermore, for the β oscillations the beating behavior renders the standard procedure of the Dingle temperature determination impossible. An alternative method is given by directly fitting the dHvA amplitude by the LK formula taking account of the beat frequency estimated above. Applying this procedure, the Dingle temperature associated with the β orbit takes a value of $T_{D,\beta} = 2.0 \pm 0.5$ K, if we do not consider the MB effect. Assuming the MB field to be lower than 30 T, the value found for B_0 in the κ -NCS [82], the obtained Dingle temperature is overestimated by less than ~ 0.7 K. This assumption for B_0 is likely to be correct, since the energy gap between the open and closed parts of the FS is expected to be smaller in the FS of the κ -Br compound. Although this determination of the Dingle temperature, $T_{D,\beta}$, is rather crude, it should give at least a correct order of magnitude.

Contrary to the β oscillations, the α oscillations are not obviously affected by a beating behavior. However, even if there is no sign of beats in the available field range, there is no plausible reason why the FS associated with the α orbit should not be influenced by a finite interlayer bandwidth as it is evident for the MB β orbit which involves the whole FS. The facts that there is no information about a possible beat frequency, that the α oscillation amplitude is markedly lower than that of the β oscillations, and that only a few oscillation periods can be observed in the available field range, make the Dingle temperature determination for the

⁴As a general rule [9], the MB should be visible starting from $B \simeq B_0/2$, for the present FS configuration.

α oscillations even less reliable than that for the β oscillations. If we still try to roughly estimate $T_{D,\alpha}$ from the magnetic field dependence of the oscillation amplitude, we obtain a value of $T_{D,\alpha} \sim 1$ K.

The values estimated for the Dingle temperatures associated with the α and β orbits are both markedly higher than that found for the κ -NCS. In this sister compound, an analysis of the Dingle temperature associated with the α orbit estimated for the field range below the MB field revealed values of $T_{D,\alpha} \simeq 0.5$ K (see, e.g., [73, 79]) down to $T_{D,\alpha} \simeq 0.25$ K [82]. The Dingle temperature, $T_{D,\beta}$, of the present compound corresponds to a scattering rate of $\tau^{-1} \sim 1.5 \times 10^{12} \text{ s}^{-1}$. In the parabolic band approximation and assuming a Fermi energy of $\epsilon_F \simeq 0.06$ eV this rate gives a mean free path of about 350 Å. Although it is appreciably higher than that reported from the first SdH study [34] this value for the mean free path is much lower than those found in the sister compounds κ -NCS and κ -Cl [91], as well as generally lower than those in most other salts of the BEDT-TTF family (see, e.g., [40] for a review).

The reasons for such strong scattering in the κ -Br salt are not well understood so far. A possible explanation could be based on recent results showing that the ground state of the κ -Br compound is situated at the border between metallic (superconducting) and insulating antiferromagnetic states [44] (Fig. 4.1). Compared to the ground states of the closely related sister compounds κ -Cl and κ -NCS, that lie in the insulating and conducting region, respectively, that of the κ -Br salt is expected to be situated closest to the transition and might thus be already affected by fluctuations associated with the insulating state. This supposition finds support in works by Kawamoto *et al.* [92] and Taniguchi *et al.* [93] who have demonstrated that the substitution of deuterium instead of hydrogen at the terminal ethylene groups of the BEDT-TTF molecule drives the system to a Mott-insulator state which is supposed to be the ground state of the κ -Cl salt [46].

Kawamoto *et al.* [92] and Su *et al.* [94] argued that the rate of cooling of deuterated κ -Br through the temperatures around 80 K has a strong effect on its low temperature electronic properties and decides about whether the system ends up in a superconducting or insulating state at low temperatures. At 80 K, anomalies in the crystal lattice parameters [58, 57] and bond lengths in the anion layer [95] exhibiting characteristics of a second order phase transition had been observed in both the hydrogenated and deuterated modifications of κ -Br. The details of these findings suggest that this transformation is associated with conformational ordering of the terminal ethylene groups upon cooling through the transition temperature. This is corroborated by recent relaxation studies of the hydrogenated κ -Br [96, 60] that reveal a highly hysteretic character of this transformation. Since the characteristic time needed to bring the system into equilibrium is $\sim 10^3$ s at 80 K [96, 60] and rapidly increases with cooling, it is plausible to expect a phase inhomogeneity at low temperatures even for a relatively slowly cooled sample (in the experiments presented in this work the cooling rate was about 1 K/min at ~ 80 K). The remanent high-temperature phase, which probably undergoes magnetic ordering, may cause additional scattering and even some internal field inhomogeneity, thus suppressing the amplitude of the quantum oscillations.

Recent systematic SdH and relaxation studies on the κ -Br salt [97] allowed to correlate the Dingle temperature to the degree of structural order in the sample and thus to separate the relative contributions of intrinsic impurities and structural disorder to the carrier scattering. The Dingle temperature appeared to approach a value of about 2 K for the ideally ordered state. Such high residual value of T_D would imply that it is actually not disorder but rather a high intrinsic impurity level which is responsible for the increased scattering in the present compound. This mechanism would be in line with the suggestion of Mielke *et al.* [72]. These authors propose a contamination by Cu(II) ions produced during the electrochemical synthesis as a probable source of additional scattering. Electrochemical studies showed that the oxidation potentials of BEDT-TTF and the Cu[N(CN)₂]Br anion are similar [98]. This implies that considerable quantities of Cu(II) are indeed generated during the electrocrystallization process. However, further investigations are needed in order to clarify whether the produced Cu(II) is finally incorporated into the κ -Br crystal. Moreover, it would be desirable to carry out comparative studies on the κ -Cl and κ -NCS salts that can be produced in very similar synthesis processes. This could allow to find out if the κ -Br salt contains more Cu(II) than its sister compounds.

4.3 Shubnikov-de Haas Measurements

Before the observation of dHvA oscillations in κ -Br by the torque method, electronic transport measurements had been employed to search for magneto-quantum oscillations in this compound. Until the present work, however, these measurements unveiled weak SdH oscillations only under high pressure.

Fig. 4.16 shows a typical plot of the ambient pressure interlayer magnetoresistance over a large field interval, 0 T to 26 T [71].

Above the superconducting transition field $B_{c2} \simeq 9$ T, a broad magnetoresistance onset is observed. As indicated by the smooth change in the slope of the curve over a field range as large as ~ 10 T, superconducting fluctuations likely survive up to fields of ≈ 20 T. At further increasing the field, the magnetoresistance slope saturates and even tends to become negative at the highest available fields. The low-temperature magnetoresistance in the non-superconducting region is rather low compared to many other BEDT-TTF based salts, but comparable to that found in the metallic state of the κ -Cl compound under low pressure [67]. By subtracting the slowly varying background semi-classical resistance, R_0 , quantum-oscillations become clearly visible starting from 18 T.

4.3.1 SdH Oscillation Frequencies

Figure 4.17(a) displays the normalized oscillatory magnetoresistance for different orientations of the magnetic field, θ . At a first glance, the oscillations exhibit only one frequency with an oscillation amplitude of $\sim 0.1 \Omega$ at the highest fields.

Applying a Fourier filter a frequency $F(\theta = 0^\circ) = 3790 \pm 10$ T is detected. In

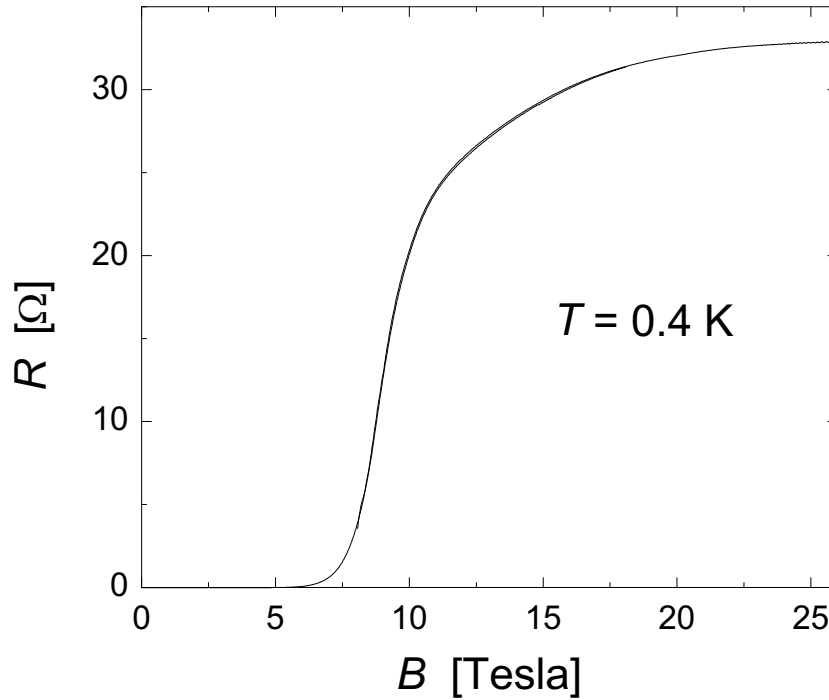


Figure 4.16: Magnetic field dependence of the interlayer resistance for $\theta = 0^\circ$ at $T = 0.4$ K.

coincidence with the recent dHvA experiments [70], this frequency can be readily identified with the area enclosed by the MB β orbit. The observation of this oscillation frequency in an ambient pressure SdH experiment [71] within the present work provided the first evidence of the existence of a well-defined FS in the κ -Br compound under ambient pressure.⁵ It thus definitely allowed to place the ground state of the κ -Br salt into the metallic phase of the generalized phase diagram shown in Fig. 4.1. The data obtained in these initial studies did not reliably prove the existence of the expected conventional α orbit. Yet, further detailed measurements [70] unveiled a distinct contribution of a frequency $F(\theta = 0^\circ) = 530 \pm 15$ T which agrees well with that found for the α oscillations in the dHvA Fourier spectrum.

At the highest field and $\theta = 0^\circ$, the amplitude ratio of the oscillatory part to the background amounts to $R_{osc,\beta}/R_0 \approx 0.02$ for the β oscillations, whereas it is markedly lower, $\Delta R_{osc,\alpha}/R_0 < 5 \cdot 10^{-4}$, for the α oscillations. The ratio of the α and β oscillation amplitudes is thus noticeably lower than found in the dHvA signal.⁶ These facts illustrate, why the α oscillations have been found first in the dHvA experiment [70] and much later than the β oscillations [68, 71, 72]. Even with the use of the highest-quality κ -Br crystals synthesized to date the intensity

⁵At the same time as this study [71], SdH oscillations in κ -Br at ambient pressure were independently observed in pulsed magnetic fields [72]. In that work the oscillations of the single frequency, $F = 3798 \pm 5$ T, become visible above 40 T.

⁶A quantitative discussion of this feature is given in the following section 4.4.

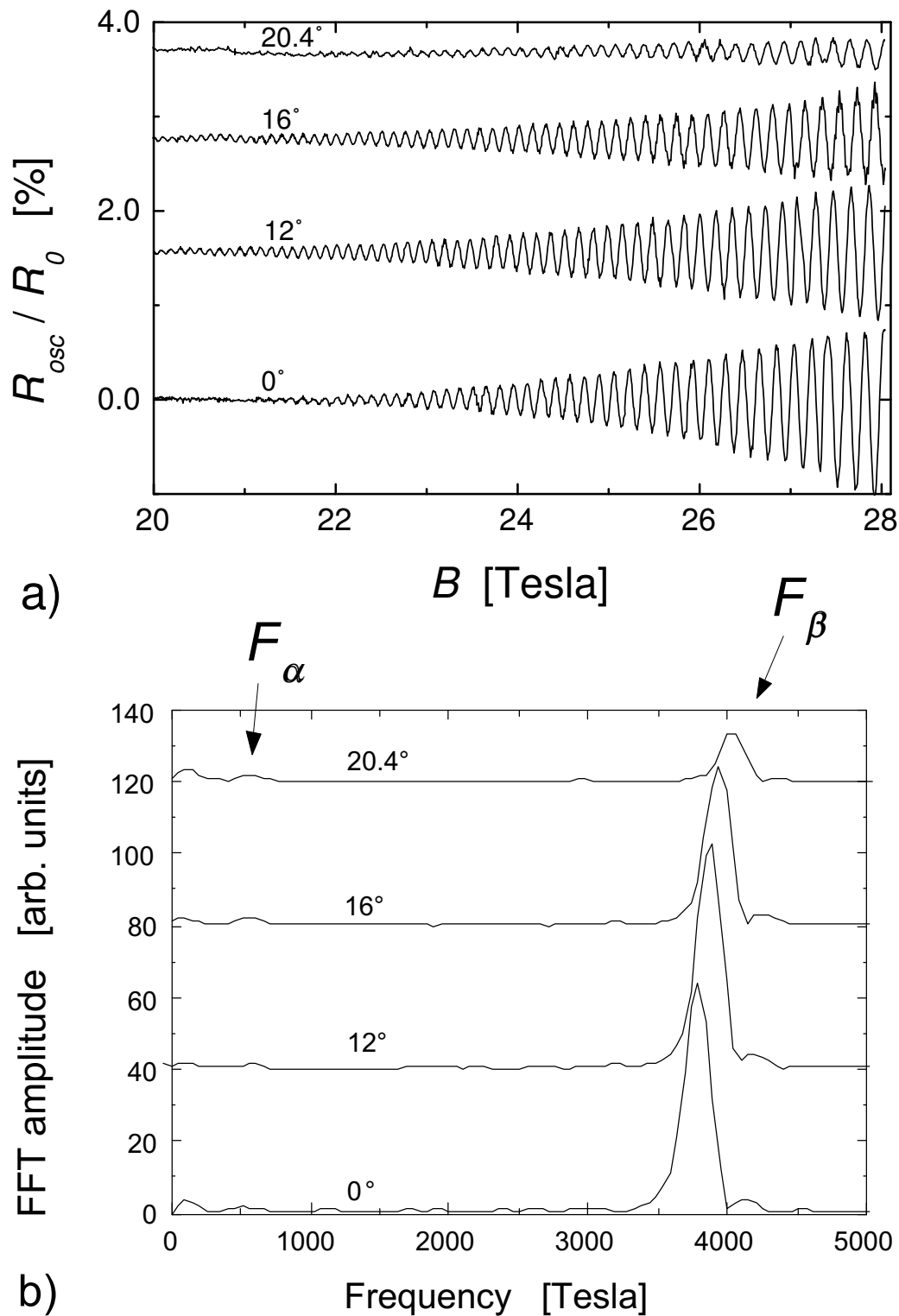


Figure 4.17: (a) Oscillatory magnetoresistance, $R_{osc} = (R - R_0)$, normalized to the slowly varying background resistance R_0 , at several angles θ . (b) FFT of the curves shown in Fig. 1(a) over a field interval from 20 T to 28 T. The curves are offset for clarity in both graphs.

of SdH oscillations associated with the α orbit exceeds only slightly the resolution of the experiment. The very low amplitude ratio $\Delta R_{osc,\alpha}/\Delta R_{osc,\beta}$ confirms the conclusion, made in the previous section 4.2.1, that we can assume the system to be in a deep MB regime already at the lowest fields where oscillations become visible. This situation resembles to that found in SdH experiments on the κ -Cl salt [49] in the metallic state under pressure. In this compound both frequencies coexist already in fields below 14 T in the whole pressure range up to 12 kbar. Noteworthy, angle dependent magnetoresistance oscillations (AMRO) on this compound [67] revealed a finite in-plane component of the transfer energy direction vector, \mathbf{h} . This hints to a break in the orthorhombic symmetry that in turn causes a gap opening between the open and closed parts of the FS. A rough estimation of the MB gap gives $\epsilon_g \approx 0.14$ meV at a pressure of 7.7 kbar [99], that would correspond to a MB field of the order of 10 mT, three orders of magnitude lower than the fields involved in the experiment and than the MB field found for the FS of the κ -NCS salt [82]. From the similar behavior of the SdH oscillations in κ -Br and in κ -Cl in the metallic state we can presume the MB field and thus the energy gap at the BZ boundary to be of comparable size in both systems. However, AMRO studies on κ -Br would be desirable in order to obtain more information about the origin of the MB gap in the FS of this compound.

4.3.2 Effective Cyclotron Masses

The analysis of the temperature dependence of the oscillation amplitudes, as described in the previous section 4.2.3, reveals cyclotron masses, $m_\alpha^* = 3.0 \pm 0.5 m_e$ [70] and $m_\beta^* = 6.7 \pm 0.5 m_e$ [81] at $\theta = 0^\circ$, that are consistent with the dHvA data [70]. Compared to the mass value, $m_\beta^* = 5.4 \pm 0.1 m_e$, reported by Mielke *et al.* [72], the present result is considerably higher. The difference between both values exceeds the stated error bars by more than a factor of 2. It has to be noted that the lower mass value was obtained in pulsed-field magnetoresistance studies in fields well above 30 T, the upper field limit of the present experiment. However, no field dependence of m_β^* was found within the studied field interval. Another possible reason for the discrepancy between both estimates of the effective cyclotron mass value may be sample heating in pulsed-field measurements that often leads to underestimates of the effective mass [100]. Very recently, Stalcup *et al.* [97] nearly exactly reproduced the value m_β^* of the present experiment in SdH measurements using steady fields up to 33 T.

4.3.3 Angular Dependences of Electronic Properties

On account of a less favorable signal-to-noise ratio, the SdH signal could not be followed over an angular range as large as measured in the dHvA study. SdH oscillations are resolved within tilt angles, θ , of the magnetic field up to 30° for both, the α and β oscillations.

Analogously to the observations made in the dHvA experiment, both oscillation frequencies increase with the angle θ . As illustrated in Fig. 4.18(a), the β

oscillation frequency reproduces the $1/\cos\theta$ dependence.

Due to the extremely low oscillation amplitude of the α oscillations, the determination of their frequency is affected by a significant uncertainty. Hence, an unambiguous angular dependence of the α oscillation frequency cannot be deduced from the SdH data. Nevertheless, a $1/\cos\theta$ fit does not contradict to the present behavior [Fig. 4.18(b)].

Within the angular range where SdH oscillations could be observed, the β oscillation amplitude decreases with θ and exhibits a minimum at $\theta = 27^\circ$, shortly before it becomes lower than the resolution of the experiment. This minimum is in very good agreement with the spin-splitting zero observed in the torque signal. Therefore, although only one minimum is observed, we assume it to be caused by the Zeeman spin-splitting effect. A plot of the experimental data along with a fit according to the LK formula is shown in Fig. 4.19.

The low amplitude of the SdH oscillations associated with the α orbit does not allow to reliably extract any angular dependence of the α oscillation amplitude. A definite conclusion, which of the two scenarios indicated in Fig. 4.15(a) apply, can thus not be made. In principle, due to a vanishing torque signal at angles around $\theta = 0^\circ$, SdH measurements allow for a more accurate estimation of the oscillation amplitude in this angular region than magnetic torque measurements do. Further detailed SdH studies with better statistics and narrow angular scanning around this symmetry direction are therefore likely to provide useful information for a final decision.

4.4 Simultaneous de Haas-van Alphen and Shubnikov-de Haas Measurements

In order to be able to directly compare the data obtained by thermodynamic and transport measurements at identical conditions, simultaneous torque and inter-layer magnetoresistance measurements were carried out on κ -Br [70]. Such kind of experiment is especially intriguing since it allows to check if the theoretical descriptions that are used for the analysis of dHvA and SdH oscillations, respectively, generally apply to the present system and lead to the same results. Although it is usually assumed that the SdH effect can be treated in an analogous way as the dHvA effect [cf. Eq. (2.9) and (2.26)], a conclusive quantitative theory as given by the LK formalism is still missing for the SdH effect. Moreover, this shortcoming is of particular consequence for the compound under investigation since it is characterized by a highly anisotropic conductivity associated with a FS characteristic of a quasi-two-dimensional electronic system.

4.4.1 Relative Oscillation Amplitude $\Delta R_\alpha/\Delta R_\beta$

A typical example of a simultaneous dHvA and SdH run is shown in Fig. 4.20 for the magnetic field orientation $\theta = 16^\circ$. As already mentioned in the previous section 4.3.1, the contribution of the α oscillations related to the β oscillations is

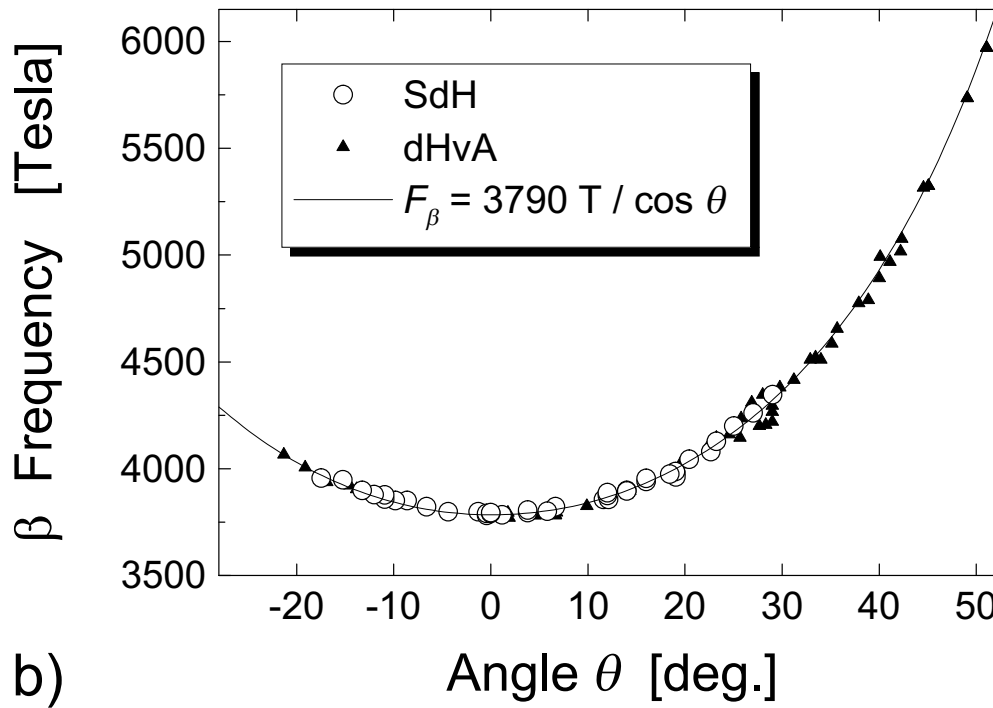
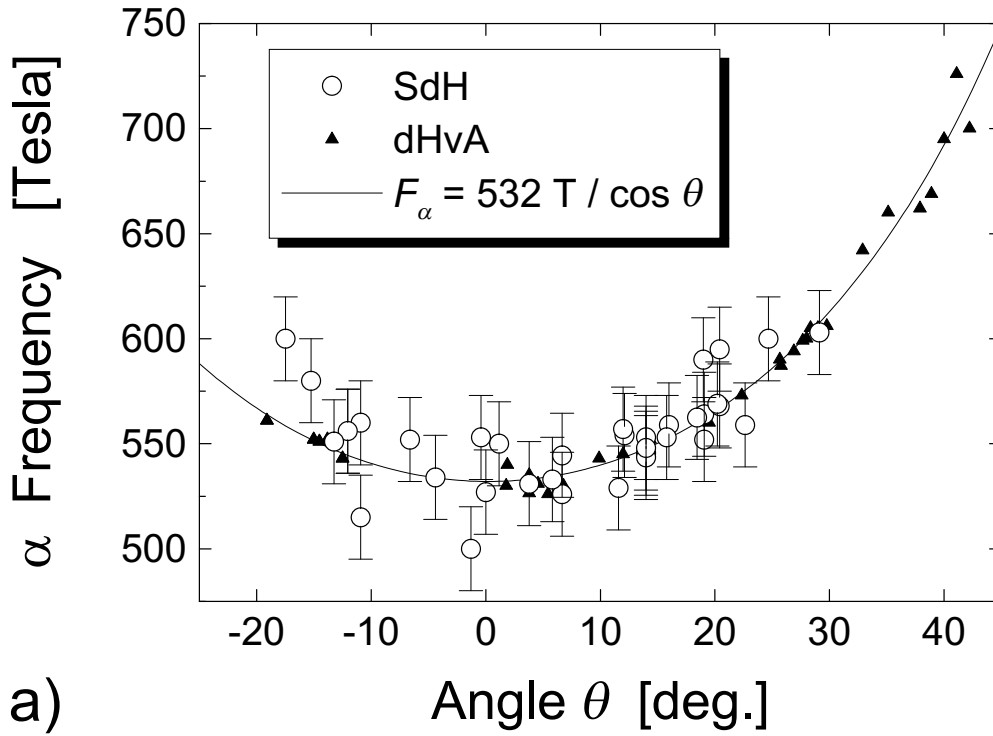


Figure 4.18: Angular dependence of the (a) α and (b) β oscillation frequencies observed in SdH measurements. For comparison, also the values extracted out of the dHvA oscillations (Fig. 4.10) are shown.

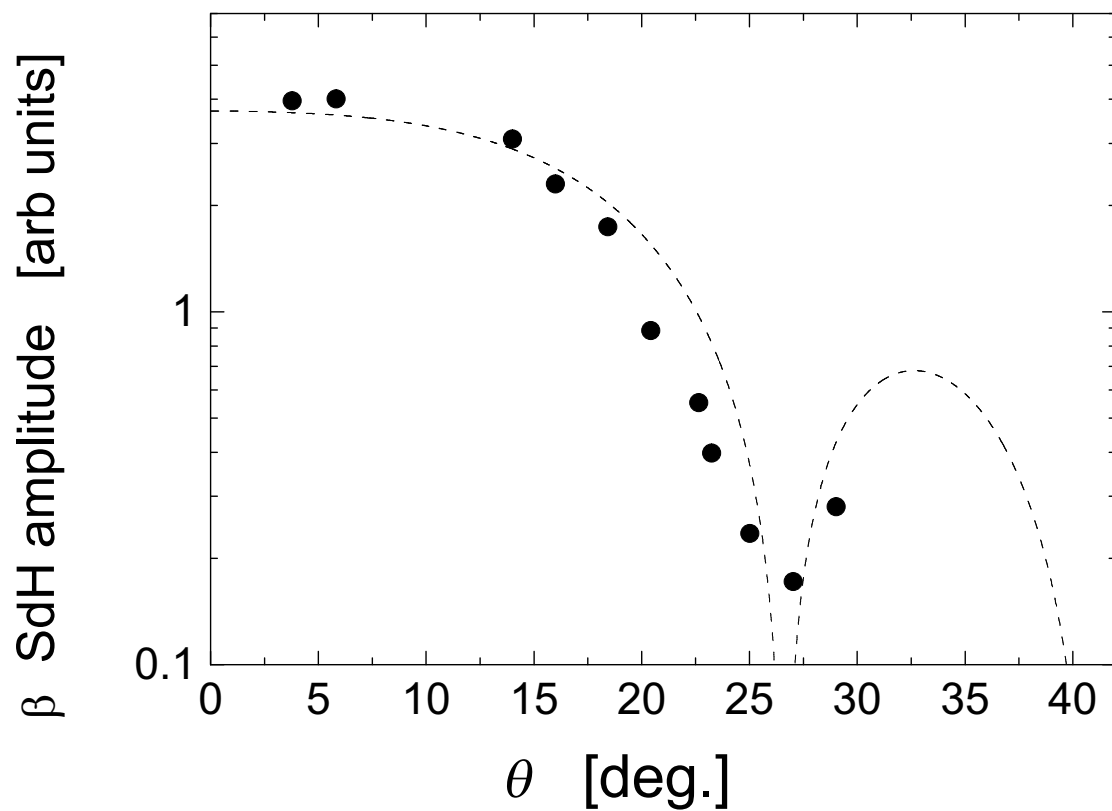


Figure 4.19: Angular dependence of the FFT amplitude of the β oscillations observed in the SdH study along with the fit according to the LK formula (dashed line).

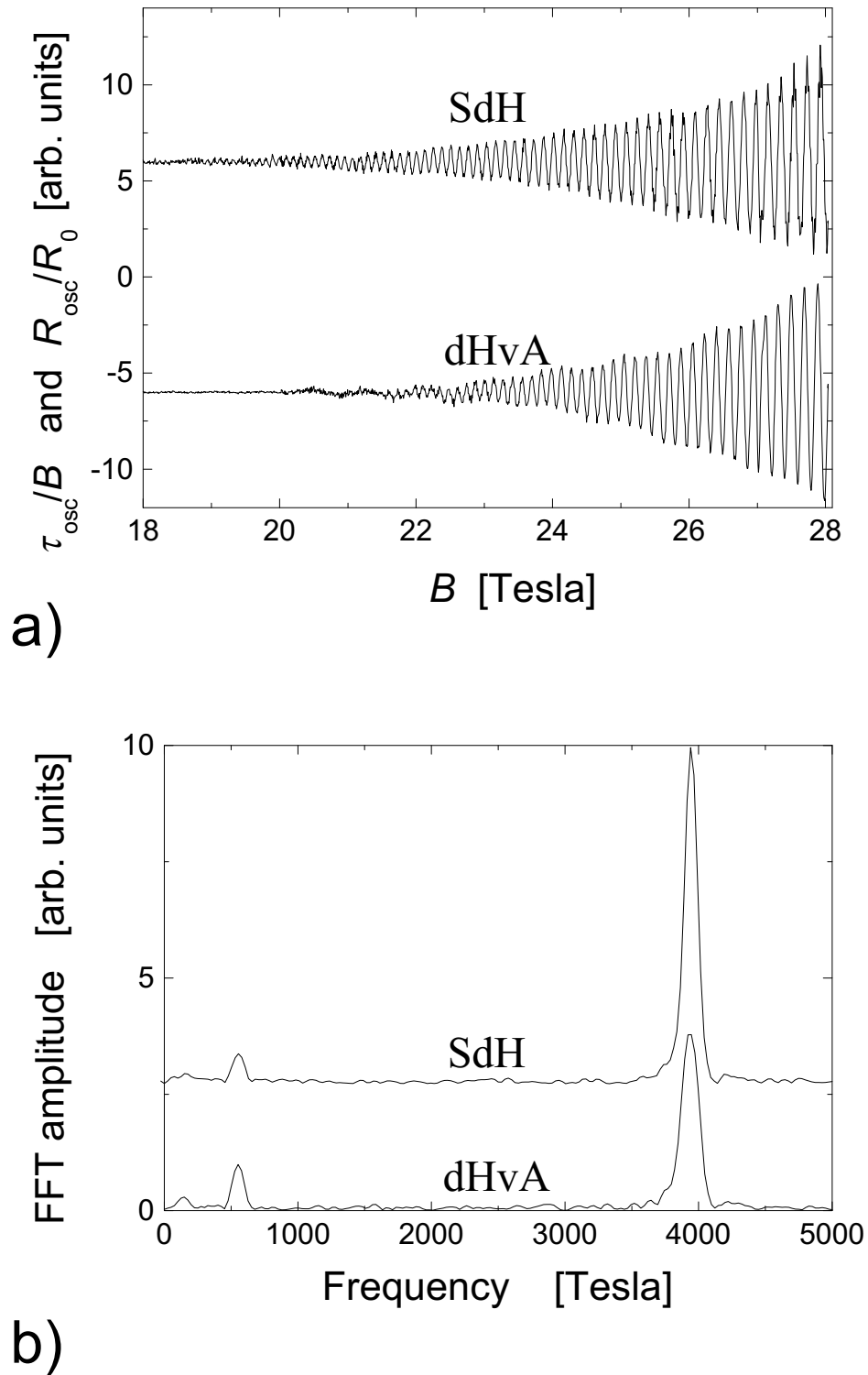


Figure 4.20: SdH and dHvA oscillations at $\theta = 16^\circ$ (a), along with the corresponding FFT's (b). R_0 denotes the slowly varying background resistance. The curves are offset for clarity.

noticeably lower in the SdH signal compared to the dHvA signal. Equation (2.25), which demonstrates the proportionality between the density of states at the Fermi level and the derivative of the magnetization with respect to the field, sets up a relation between the dHvA and the SdH oscillations derived for a three-dimensional FS. Applying this relation to the magnetization extracted from the torque signal we obtain an estimate for the behavior of the SdH oscillations as expected by the theory. Fig. 4.21(a) illustrates the field-normalized torque displayed in Fig. 4.20(a) along with its derivative modified according to Eq. (2.25).

It is evident that with this transformation of the oscillatory torque signal the low α oscillations are markedly suppressed and the FFT spectrum yields essentially the amplitude ratio of the α and β oscillations observed in the SdH measurement. The dHvA and SdH measurements thus give consistent results. This indicates that compared to the dHvA measurement, which probes pure thermodynamics, the magnetotransport is not considerably influenced by scattering processes in the investigated field and temperature range.

4.4.2 Beating Effect

As discussed in section 4.2.2, a node was observed in the dHvA oscillations for field orientations around positive and negative angles $\theta = \pm 14^\circ$. The most striking difference between the SdH and dHvA signals is the fact that the former do not show any node or beating behavior in the available field interval. Fig. 4.22 presents dHvA and SdH signals measured simultaneously on the same sample at the tilt angle $\theta = 12^\circ$. At this field orientation, a node in the dHvA oscillations appears at the field $B_{node} = 26.5$ T. The insets (a) and (b) show both types of oscillations at fields above and below the node position. At $1/B < 1/B_{node}$, the phase shift between the dHvA and SdH oscillations is $\pi/2$, in full agreement with the standard semi-classical theory [9] [cf. Eq. (2.9) and (2.26)]. At B_{node} , the phase of the dHvA oscillations reverses whereas the SdH oscillations do not show such features at this field. This leads to a change in the relative phase shift by π [see Figs. 4.22(a) and (b)]. This observation was made on two samples and is consistent with the results obtained by separate SdH and dHvA measurements.

As a possible check if the SdH oscillations actually follow an angular dependence as theoretically expected for a perfectly two-dimensional FS shape, the envelope of the SdH oscillations can be analyzed. This is easily done by employing the Dingle temperature which provides a measure for anomalies in the field dependence of the oscillation amplitude. In general, the Dingle temperature should be independent on the tilt angle θ . A plot of the angular function of the Dingle temperature estimated from the field dependence of the β oscillation amplitude assuming an angular behavior, $m_\beta^*(\theta) = m_\beta^*(\theta = 0^\circ)/\cos\theta$, of the effective cyclotron mass is shown in Fig. 4.23. The value of T_D obviously decreases by about 50% over the angular range $\theta = 0^\circ$ to 25° . With the analysis of this result, the question arises whether the actual scattering rate τ or the mean free path l is angle dependent in the κ -Br system. The solution of this question requires the knowledge about which of both quantities is renormalized by the angle dependent effective mass.

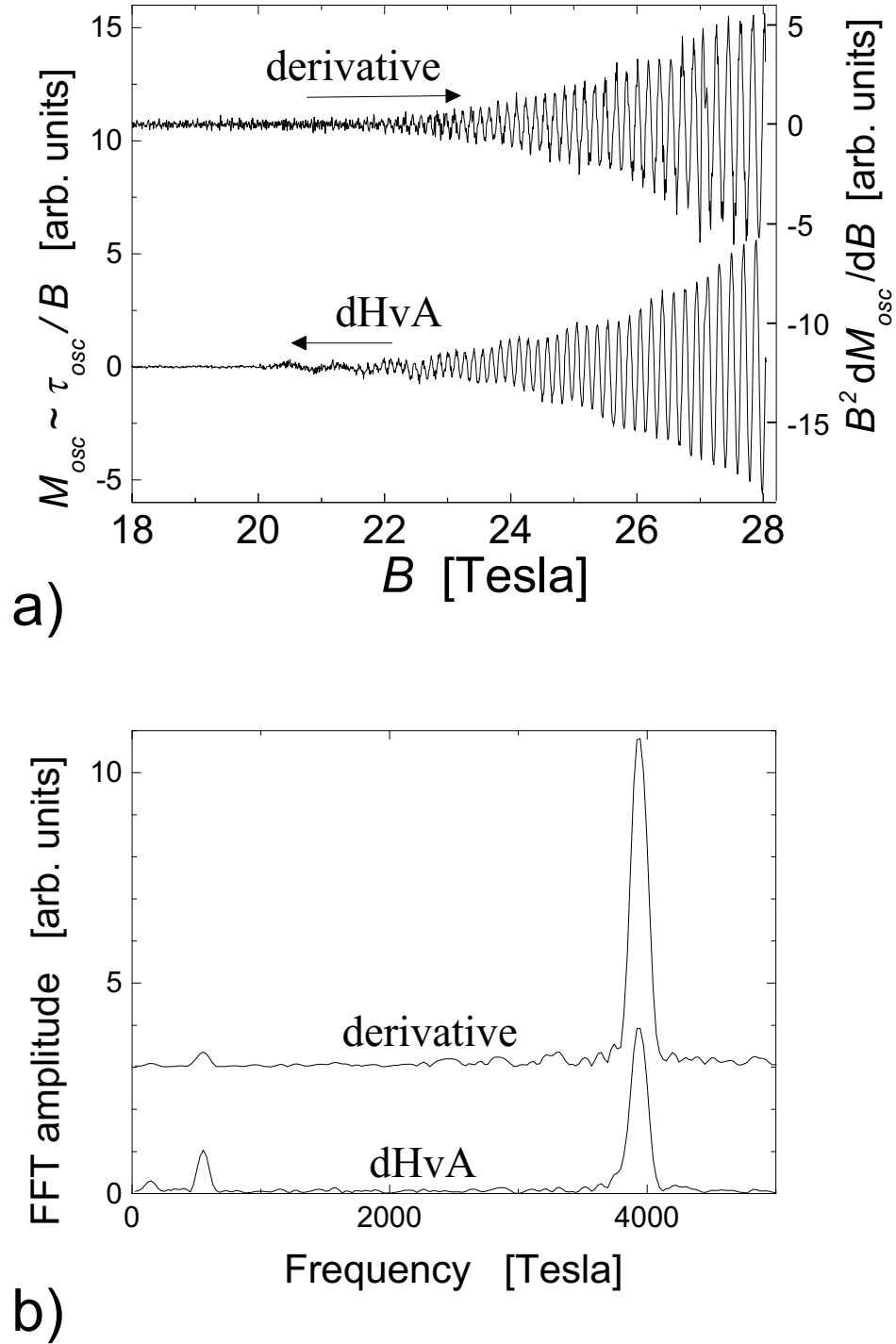


Figure 4.21: (a) dHvA oscillations at $\theta = 16^\circ$ (left scale) together with the derivative (right scale) expected to yield the shape of the SdH signal. (b) FFT's of both curves shown in (a), offset for clarity.

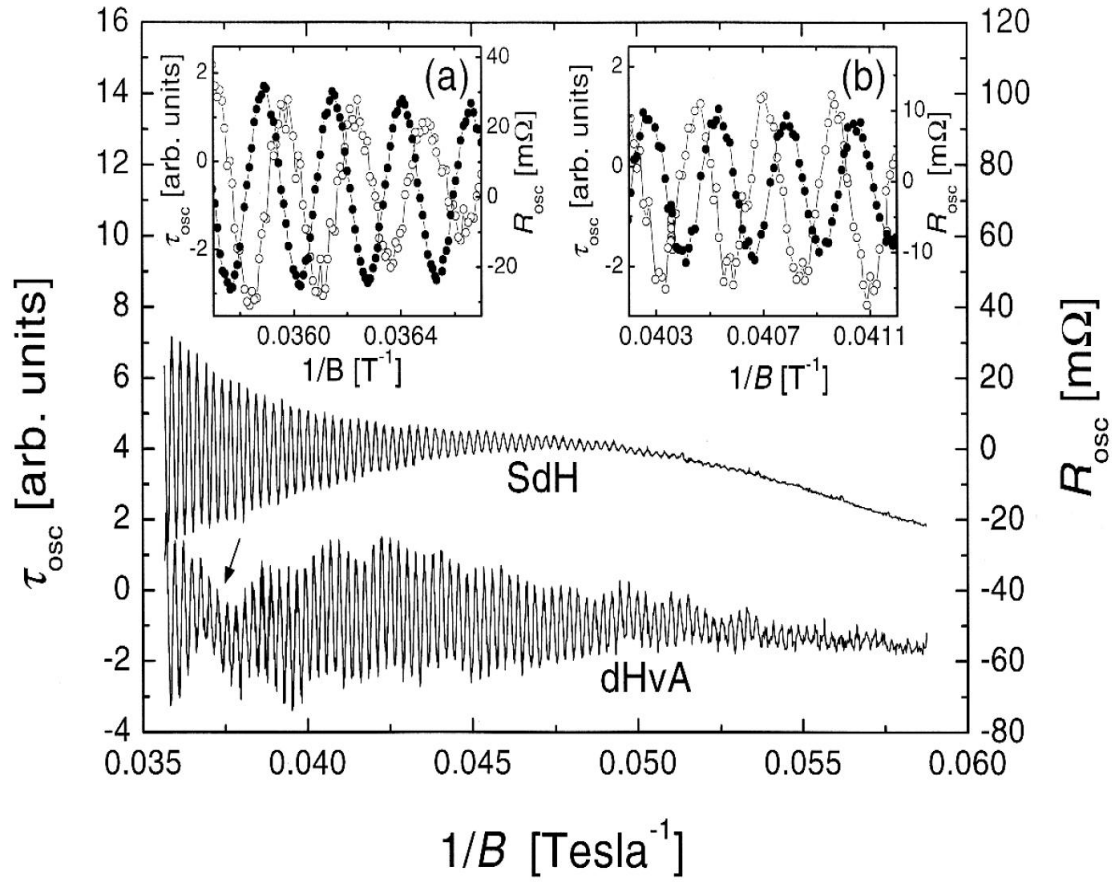


Figure 4.22: (a) SdH and dHvA oscillations at $\theta = 12^\circ$. The arrow points to the node position B_{node} in the dHvA signal. Insets: SdH (solid circles) and dHvA (open circles) oscillations in a larger scale at $1/B < 1/B_{node}$ (a) and $1/B > 1/B_{node}$ (b).

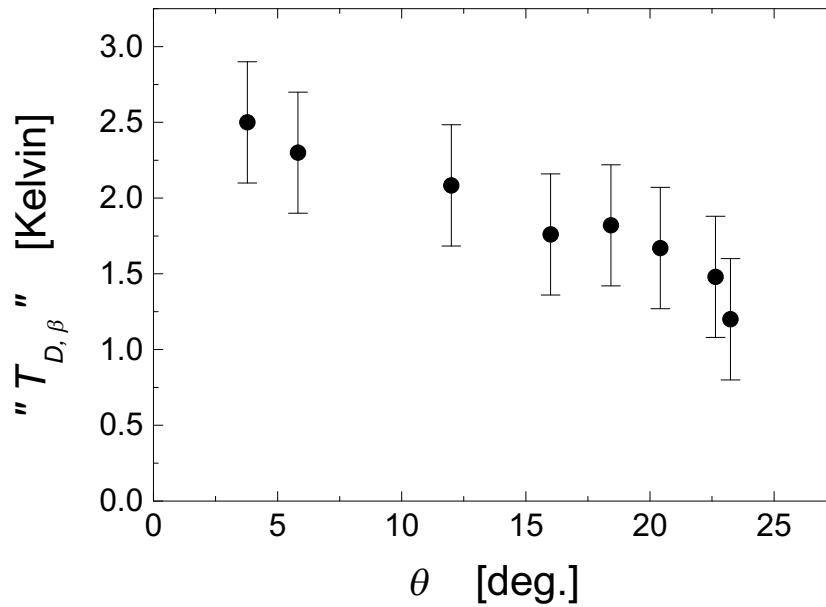


Figure 4.23: Angle dependent values for the Dingle temperature estimated from the field dependence of the SdH oscillation amplitude associated with the β orbit. The effective cyclotron mass m_{β}^* is assumed to follow a $1/\cos\theta$ behavior.

However, in the present situation, each of both cases would lead to a variation of the respective quantity by not more than 5% at the angle $\theta = 25^\circ$. This is significantly less than observed for the decrease in the value of T_D . Hence, the angular behavior of T_D is not reducible to an angular dependence caused by the effective mass. It is rather very likely an indication that the SdH oscillations are affected by beats, too, but with beat nodes that are shifted in field with respect to those of the dHvA oscillations and thus could not be detected within the available field range. The beat nodes shift from high to low fields with increasing θ that leads to an artificial decrease of the Dingle temperature value with increasing angle. This model finds support in recent experiments [101, 102]⁷ that had been stimulated by the present results. Subject of these measurements were organic conductors, β -(BEDT-TTF)₂IBr₂ and (BEDT-TTF)₄[Ni(dto)₂] that exhibit slightly warped FS structures and allow the detection of more than one node at relatively low magnetic fields. Nodes proved to exist indeed in both, dHvA and SdH oscillations, with a beat phase considerably shifted between both types of oscillations. A beat phase shift of $\pi/2$ was reported in Ref. [102]. This would mean that, in contrast to the standard LK formalism, the phase factor $\pm\pi/4$ in Eq. (2.9) is effectively inverted to $\mp\pi/4$ in the case of the SdH oscillations. If we assume this factor to be valid for the SdH oscillations observed in the present experiment it turns out that

⁷The experiment reported in Ref. [101] was performed by use of a setup analogous to the present one. The dHvA and SdH measurements described in Ref. [102], however, were not carried out simultaneously. Here the magnetotransport was separately measured; then the contact wires were cut, in order to measure the torque signal.

around $\theta = 0^\circ$ the first node ($n = 0$) coming from high fields should lie at fields higher than 100 T whereas the second node ($n = 1$) should lie at about 20 T, i.e., exactly in the field region where SdH oscillations start to be observable. Hence, there is a probability to observe this second node in the SdH oscillations of κ -Br if samples are at disposal that exhibit slightly higher oscillation amplitudes than found in the present experiment.

The nature of the striking difference between dHvA and SdH oscillations is not clear so far. On the one hand, one could presume that a peculiar warping of the FS or an unusually strong k -dependence of the electron parameters on the FS affect magnetization and magnetotransport in different ways. The latter could be, for example, caused by the van Hove singularity lying near the Fermi level, as it is found in the band structures of κ -phase compounds [103].

On the other hand, the key for understanding the different behavior of the SdH and dHvA oscillations may lie in consideration of the high two-dimensionality of the system. Indeed, the warping of the FS estimated from the node position in the dHvA oscillations (see section 4.2.2) is likely smaller than or comparable with the Landau level spacing at given fields $20 \text{ T} \leq B \leq 30 \text{ T}$. Under such conditions the predictions of the conventional three-dimensional LK theory concerning the relative contributions from the maximum and minimum orbits to the SdH and dHvA effect [Eq. (2.9)], respectively, might no longer be valid.

A further suggestion is put forward in Ref. [102]. It is pointed out that the theory of the SdH effect worked out by Adams and Holstein [10] which involves the detailed problem of electron scattering in a magnetic field reveals different phases of the oscillations for the cases of inter and intra Landau level scattering. However, for the beat phase difference between SdH and dHvA oscillations, only a maximum phase shift of $\pi/4$ can be deduced. Moreover, in order to obtain this phase shift, intra Landau level scattering should give the major contribution to the oscillations in the magnetoresistance. This scattering mechanism is usually only found in the quantum limit when the innermost Landau tubes that exhibit the largest spacing between each other are occupied. The quantum numbers associated with the β oscillations of the compounds in which the above described beating phenomena have been found are well above $n = 100$. This would imply a predominant inter level scattering. In order to testify a possible dominance of intra level scattering, one might investigate the node position in the SdH oscillations under variation of temperature and magnetic field in compounds where a node is visible in a large field interval. This could allow to vary the weight of different scattering mechanisms that are all associated with distinct SdH oscillation phases.

All mentioned possibilities are rather unusual and are far from giving a comprehensive description of the observed difference. Hence, further detailed experimental as well as theoretical studies that examine the various scattering mechanisms with regard to a considerable SdH oscillation phase shift are highly desirable. Additional modifications for the present case of a quasi-two-dimensional electronic structure might be particularly crucial for this procedure.

4.5 Thermal History

Several experiments have been reported that investigate the influence of thermal treatment on κ -Br [96, 60, 97] as well as on its deuterated analog [92, 94]. They all hint to an exceptional sensitivity of the low temperature structural and electronic properties to the cooling procedure. Especially with regard to the unusually low dHvA and SdH oscillation amplitude observed in the present study it is challenging to look for changes in the magneto-quantum oscillation parameters when the cool-down process is systematically controlled. According to Tanatar *et al.* [60] the superconducting transition temperature can be driven to a maximum value by annealing the crystal at around 75 K. This feature may be ascribed to a reorientation and conformational arrangement of the terminal ethylene groups of the BEDT-TTF molecules. At high temperatures, the ethylene groups freely oscillate between staggered and eclipsed configurations, whereas due to a second order phase transition at the $T = 80$ K [60], they are driven into a conformationally ordered eclipsed state on cooling, given that the system is allowed to relax into its equilibrium state. In order to ensure that the latter condition is fulfilled, the crystal has to be either cooled so slowly that the equilibrium condition is always maintained or it has to be annealed at a temperature just below the phase transition. Since the former method requires very long time, the latter process is usually employed. The best result is obtained using an annealing temperature not far below 80 K, since the relaxation time increases by an order of magnitude when the annealing temperature is lowered from 75 K down to 60 K. If we assume a direct correlation between the height of T_c and the degree of order of the end ethylene groups the highest order is achieved for an annealing time of 10 hours at an annealing temperature of 75 K [60].

In the present experiment the annealing was accomplished by introducing ~ 1 mbar of nitrogen as a contact gas into the isolation vacuum of the ^3He cryostat. The cryostat was then put into liquid nitrogen. After a rather rapid cooling process of about 3 K/min from room temperature down to ≈ 100 K, the sample reached liquid nitrogen temperature and was kept at this temperature for 3.5 hours. Then the ^3He cryostat was inserted into a standard ^4He cryostat and the sample cooled down to ^4He temperature at a rate of about 1 K/min. By pumping the ^4He and ^3He baths, temperatures down to 0.4 K were stabilized and resistance and torque measurements were performed. In order to be able to directly compare the oscillation parameters obtained in the annealed state with those of a presumably more disordered state, the sample was heated up to a temperature above 120 K directly after these runs and was kept at this temperature for several minutes. The heater was then switched off and the sample was let cool down at a rate of nearly 2 K/min. At the lowest temperatures, resistance and torque measurements were carried out in the same temperature range as directly after the annealing procedure.

Comparing the resistance raw curves taken in the annealed state with those taken in the state which was established by the quenching procedure, it turns out that the background resistance is by about 10% lower in the annealed state at the

highest fields. Fig. 4.24 shows the SdH and dHvA oscillations obtained by field sweeps in both states. At all temperatures the β oscillation amplitude observed in the SdH oscillations at the highest fields decreased by about 40% after the heating procedure. For the dHvA oscillations, less curves in satisfactory resolution were obtained in the experiment. At relatively high temperatures around 1 K, where we have enough data to compare the oscillations in both states, the β oscillation amplitude lost nearly 50% in magnitude by the destruction of the annealed state.

Contrary to the significant difference found in the background resistance and in the β oscillation amplitudes of both states, no marked changes were detected in the temperature and field dependence of the oscillation amplitudes within the experimental error bars. Fig. 4.25 displays mass fits for the SdH and dHvA β oscillations in the two states. All curves can be satisfactorily fitted by an effective cyclotron mass of $6.7 \pm 0.5 m_e$. A slight increase of m_β^* is estimated from the temperature dependence of the SdH oscillation amplitude with the destruction of the annealed state. However, it is weaker than the error bar and thus needs further detailed measurements for a reliable corroboration.

The Dingle temperature could be well determined from the SdH β oscillations for both states. Within an error bar of about $\pm 10\%$ no obvious variation of T_D was found from one state to the other.

Very recently, investigations of the time and temperature dependent resistance of κ -Br were carried out by Stalcup *et al.* [97]. In that work, the cooling process was stopped at different intermediate temperatures that were maintained for 140 minutes before the samples were cooled down to the lowest temperature of about 0.4 K. At low temperatures, the superconducting critical temperature as well as the Dingle temperature were determined. The latter was estimated from the field dependence of the β SdH oscillation amplitude in fields up to 33 T. T_c , $1/T_D$, and the β oscillation amplitude were found to depend directly on the total fractional decrease in the resistance, $\Delta\rho/\rho_0$ ($\Delta\rho$ is the resistance difference between the states before and after the relaxation process; ρ_0 is the sample resistance at 90 K, which turned out to be independent of thermal history), due to one or several relaxation sequences at one or several sequential holding temperatures. These findings led these authors to regard $\Delta\rho/\rho_0$ as a parameter which is a direct measure of the structural order in the crystal.

The conditions established by the annealing procedure and the subsequent destruction of the annealed state performed in the present experiment might be regarded as qualitatively equal to those obtained by Stalcup *et al.* by cooling procedures with high and low ordering parameters $\Delta\rho/\rho_0$. Especially the treatment which resulted in the highest $\Delta\rho/\rho_0$ value found in that work is well comparable with the present annealing method. The decrease in the oscillation amplitude with the destruction of the annealed state amounts approximately to the rate found by these authors when $\Delta\rho/\rho_0$ is reduced from its highest value to half of it.

As a main difference to the results reported in Ref. [97] a markedly stronger β SdH oscillation amplitude was observed in the present work. At 26 T and 0.45 K, the oscillation amplitude measured at the raw curves normalized to the slowly varying background resistance, is by at least a factor of 3 higher than found

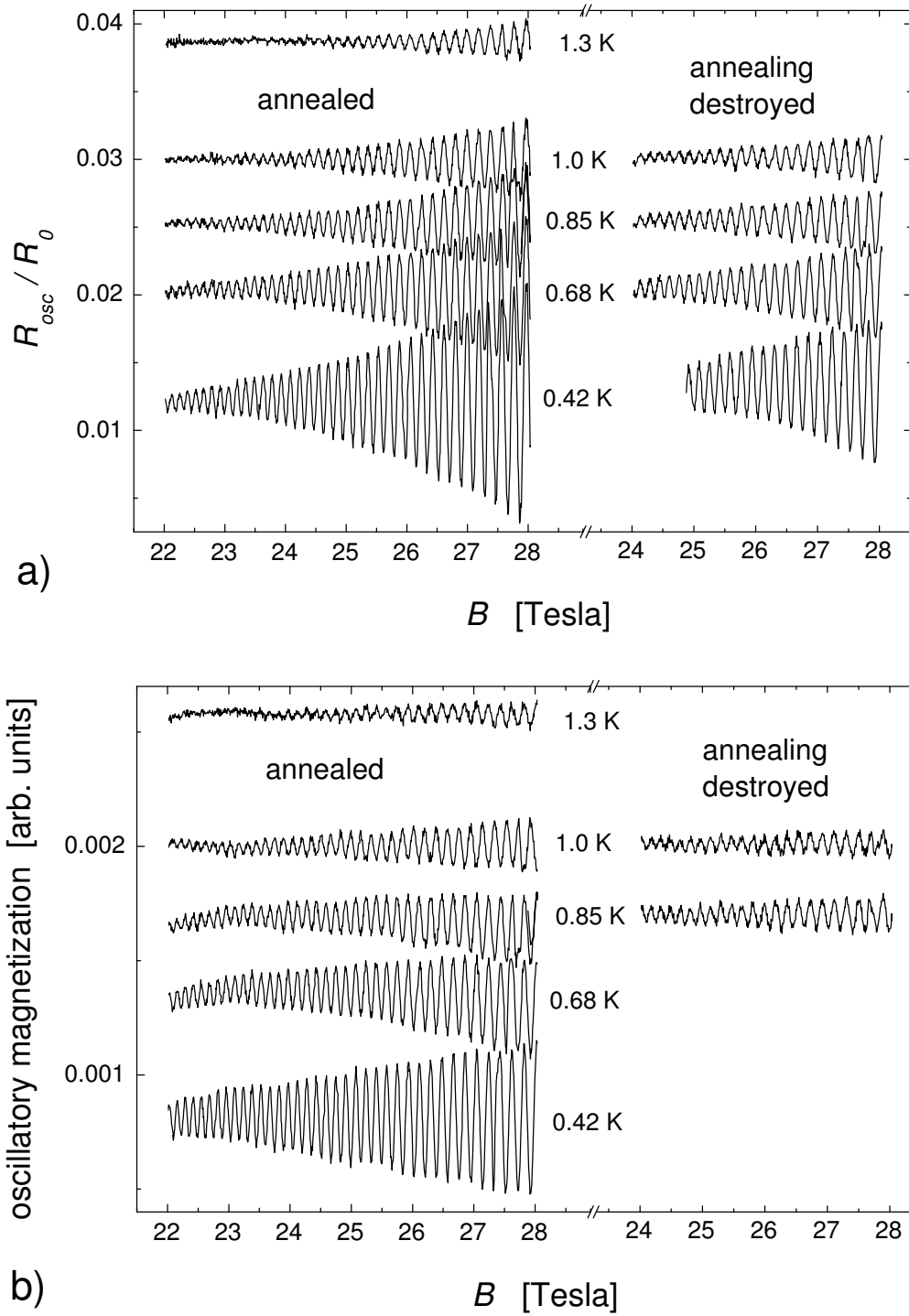


Figure 4.24: (a) SdH and (b) dHvA oscillations for several temperatures in the annealed state (left graphs) and after the destruction of the annealed state (right graphs). R_0 denotes the slowly varying background resistance. The magnetic field orientation corresponds to $\theta = 6^\circ$. All curves are offset for clarity.

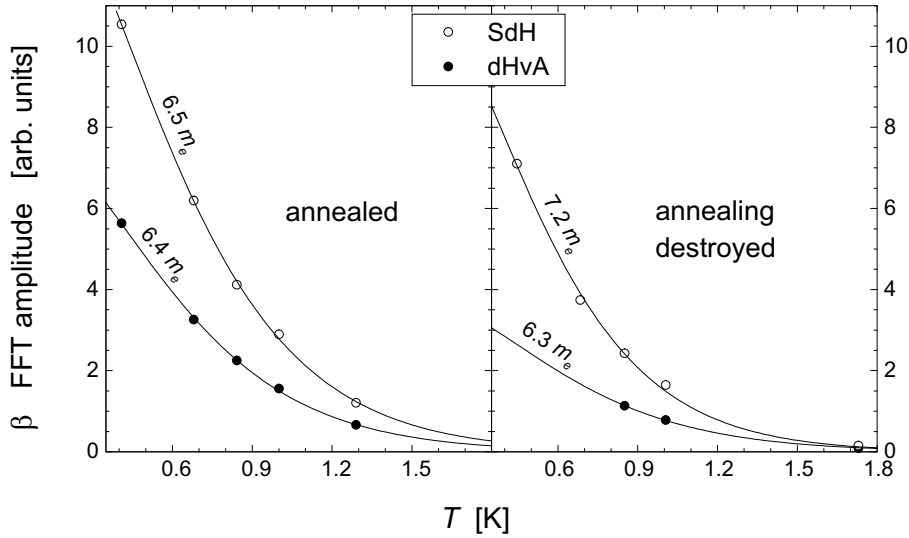


Figure 4.25: SdH and dHvA oscillation amplitudes as a function of temperature in the annealed state (left graph) as well as after the heating procedure (right graph). The magnetic field orientation corresponds to $\theta = 6^\circ$. All amplitudes are obtained by FFT's over the field interval 24 T to 28 T. The solid lines represent fits according to the LK formalism. The effective cyclotron mass values that yield the best fits are given for each curve.

by Stalcup *et al.* for the curve with the highest $\Delta\rho/\rho_0$ value. Presumably due to the weaker amplitude of the oscillations no α oscillations were found in that experiment in spite of a considerably higher maximum magnetic field available. At a first glance, one could ascribe these differences to a higher crystal quality of the samples employed in the present study. However, the Dingle temperatures estimated for our samples are approximately equal to the highest values found for the samples of Stalcup *et al.*, that would hint to a higher scattering rate in the samples used for the present experiment.

A dependence of T_D on the thermal history could not be found in the present study. Assuming both states realized in our experiment to be similar to states with one of the highest and one of the lowest $\Delta\rho/\rho_0$ values, respectively, realized by Stalcup *et al.*, this result does not agree with the dependence of T_D on $\Delta\rho/\rho_0$ reported by these authors. According to Ref. [97], especially at low $\Delta\rho/\rho_0$, where the T_D values obtained in both works coincide, T_D should strongly depend on $\Delta\rho/\rho_0$.

With regard to the results obtained in the present work, one could suggest that it is not a microscopic quality but rather a fraction of the metallic (superconducting) phase which is affected by the annealing procedure. Such a situation could occur with the existence of two spatially separated “subphases”: an ordered one which gives rise to SdH oscillations and a disordered one which may influence the slowly varying part of the conductivity but does not contribute to magneto-quantum oscillations. In that case the annealing procedure likely increases the

fraction of the ordered subphase. It would thus increase the oscillation amplitude and presumably also the superconducting critical temperature without affecting the field dependence of the oscillation amplitude, i.e., without changing the Dingle temperature.

For a conclusive understanding of the effect of the annealing procedure on the oscillation amplitude and Dingle temperature and their interplay between each other, further studies on the thermal history of electronic and structural properties are needed. In particular, the use of samples that originate from different batches and exhibit different Dingle temperatures and oscillation amplitudes at the same conditions, could help to elucidate the raised questions.

4.6 Shubnikov-de Haas Measurements under Pressure

In contrast to the cuprate superconductors that can be driven into different ground states by variation of doping, organic compounds are generally highly sensitive to external stress or pressure. The application of pressure to an organic compound allows to tune the whole system through different states with different structural as well as electronic properties that mainly reflect the increase of the electronic bandwidth. This technique is therefore much advantageous for this class of materials since only a single sample is needed for the realization of different ground states. The phase diagram presented in Fig. 4.1 shows that the κ -(BEDT-TTF)₂X family is especially favorable to a study of the interplay between structural and electronic properties. The members of this group of compounds lie very close to a metal-insulator transition and may thus be driven into states that are fundamentally different from their ground states. Since an external hydrostatic pressure works in opposite direction to U_{eff}/W (Fig. 4.1), states that are similar to each other may be realized by the appropriate variation of one or both of these quantities. Due to the closest vicinity of the ground state of the κ -Br salt to the metal-insulator transition, this compound is an ideal candidate for such studies. The substitution of hydrogen by deuterium at the terminal ethylene groups of the BEDT-TTF molecule was found to drive this system to a Mott-insulator state [92, 93], similar to the ground state of the κ -Cl salt [46]. A strong sensitivity may be expected to the application of external pressure as well which drives the system to the opposite direction, presumably deeper into the metallic state. This is indicated by several properties such as the temperature dependence of the resistance [104] and of the Knight shift [105] that are quite distinct from that of conventional metals at ambient pressure, whereas with the application of pressure of $\gtrsim 5$ kbar, the conventional metallic behavior tends to be restored.

4.6.1 Changes with Pressure - General Features

With the application of pressure, the interlayer resistance changes strongly. Kartsovnik *et al.* [34] reported a room temperature interlayer resistance which gradually goes

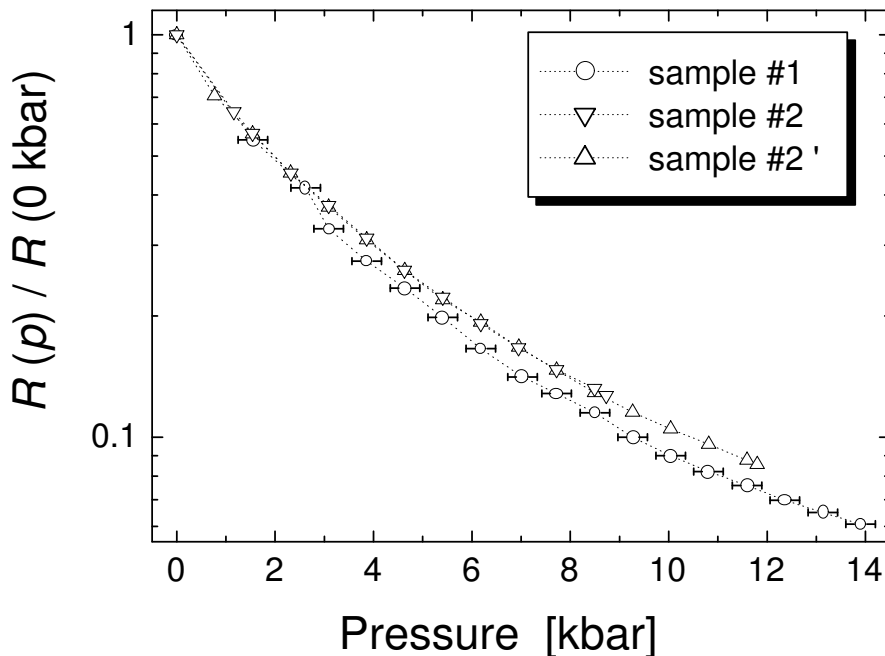


Figure 4.26: Pressure dependence of the electrical interlayer resistance at room temperature.

down with pressure showing no discontinuities that could be attributed to a phase transition. In the present experiment [71, 81], this behavior was confirmed for an even larger pressure range from ambient pressure to 13.9 kbar (Fig. 4.26). For this range, the rate of the resistance decrease is, within the experimental error, the same as that observed for the κ -Cl salt [49].

The resistance change by an order of magnitude during the loading of the pressure cell up to the highest pressure can be explained by the gradual compression of the crystal lattice under pressure. This reduces the interlayer distance and increases the overlap of the molecular orbitals not only within the highly conductive layer but also in the interlayer direction. Due to an enhanced electron exchange between the layers the dimension of the electronic system increases and the anisotropy in the electrical resistance is reduced.

At a temperature of 0.4 K the superconductivity is suppressed by a pressure of about 4 kbar. Above this pressure a superconducting onset is still visible at low magnetic fields which gives evidence for superconducting fluctuations surviving up to pressures as high as ≈ 10 kbar. The low-temperature magnetoresistance in the metallic region is even lower than that observed at ambient pressure. Its slope remains constant up to the highest fields and increases with pressure. In agreement with the previous report [34], the relative resistance increment, $\Delta R(26 \text{ T})/R_N(0 \text{ T})$,⁸ amounts to ≈ 0.06 at a pressure of 5 kbar and to ≈ 0.25 at

⁸ $R_N(0 \text{ T})$ denotes the normal-state resistance extrapolated from higher fields to 0 T, and $\Delta R(26 \text{ T}) = R(26 \text{ T}) - R_N(0 \text{ T})$.

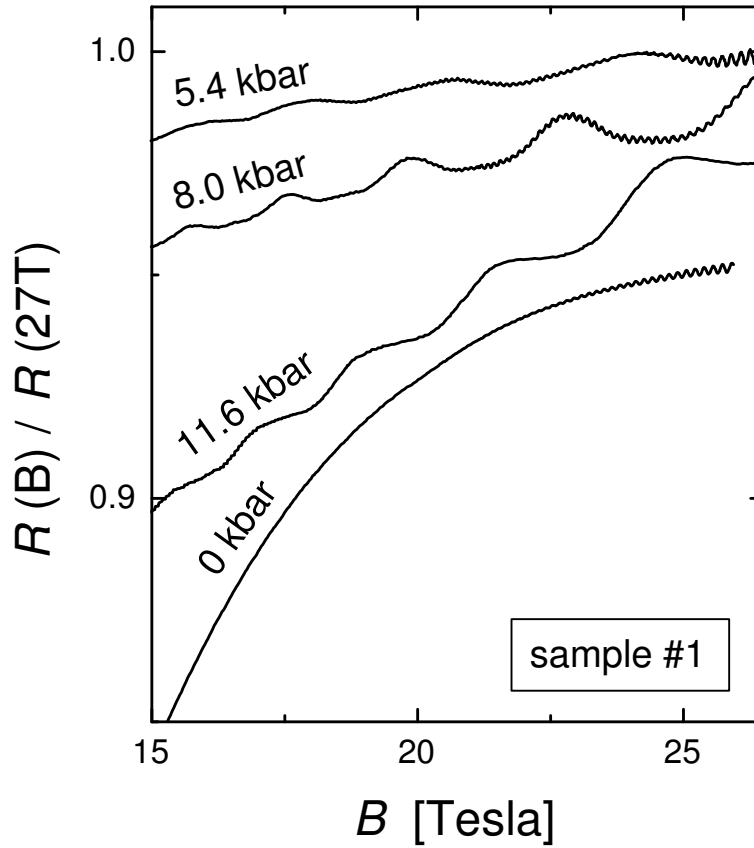


Figure 4.27: Magnetoresistance normalized to the value at 27 T for several pressures, 0 kbar to 11.6 kbar, at a temperature of 0.4 K. The curves are offset for clarity.

the highest pressure of 12.5 kbar at low temperature. Both, the absolute magnetoresistance and its slope are highly relative to those found in the κ -Cl compound under pressure [49]. The field dependence of the magnetoresistance for several pressures is displayed in Fig. 4.27. For all pressures, SdH oscillations could be detected. Depending on the pressure, they start to be visible in fields above ≈ 12 T.

4.6.2 SdH Oscillation Frequencies

Fig. 4.28 shows the oscillatory magnetoresistance, normalized to the slowly varying background resistance, measured at two different samples. In contrast to what was found in the magnetotransport signal at ambient pressure, a distinct contribution of a very low frequency with the amplitude of about $30 \text{ m}\Omega$ at the highest fields appears around 5 kbar. These oscillations are visible in the whole field interval above 12 T up to the highest pressure. Especially in the low field and intermediate pressure region these oscillations noticeably deviate from a sine-shape. Similar to the ambient pressure experiments, high frequency oscillations evolve at high fields around 20 T with an amplitude comparable to that of the low-frequency oscillations

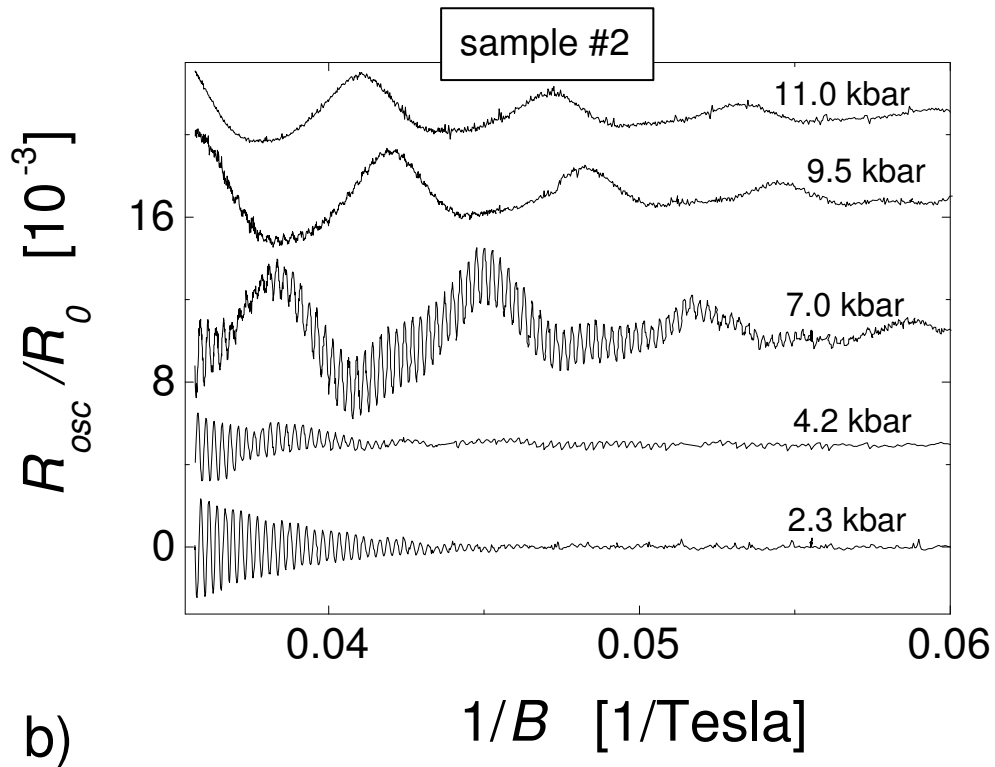
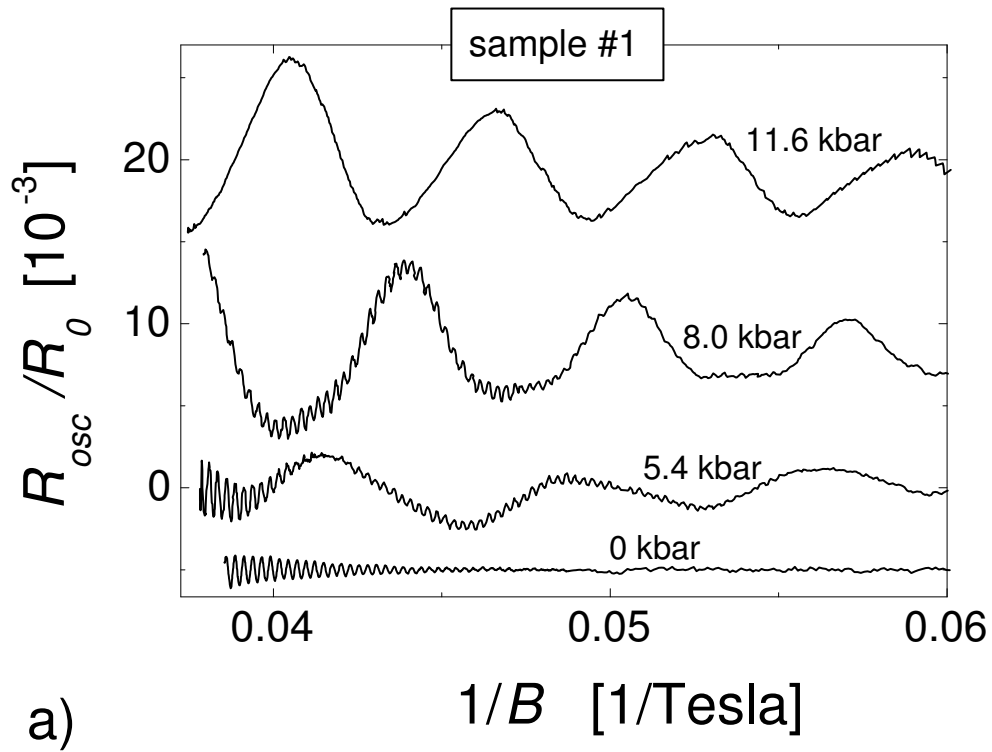


Figure 4.28: SdH oscillations observed in two different samples, (a) #1 (cf. Fig. 4.27) and (b) #2, at a temperature of 0.4 K. The curves are offset for clarity.

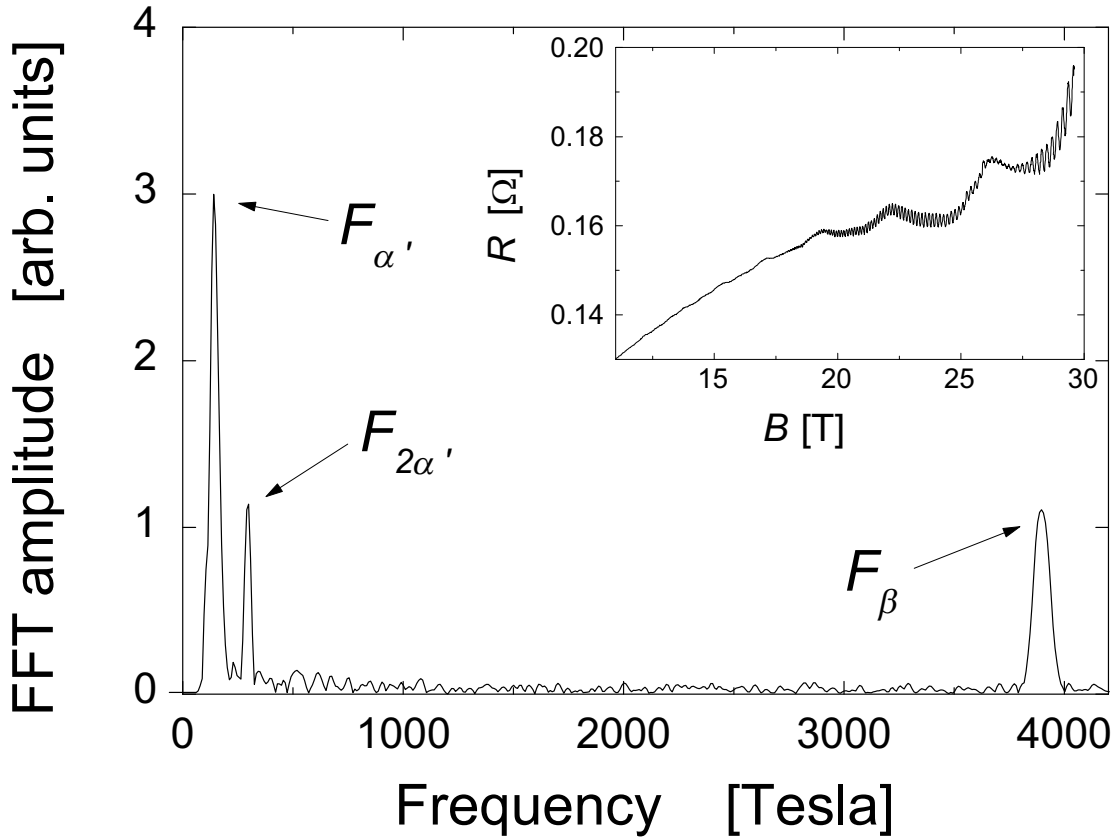


Figure 4.29: FFT spectrum of the SdH oscillations at a pressure of 7 kbar and $T = 0.6$ K, performed over the whole field interval in which the oscillations are visible (see inset with the raw data). The low relative height of the peak at F_{β} with respect to that of $F_{\alpha'}$ is due to the wide field interval, chosen for the FFT, which includes all detected periods of the α' oscillations.

at fields above 26 T and pressures 5 kbar to 7 kbar. At a pressure higher than 10 kbar, they become lower than the resolution of the experiment. A representative FFT for the frequency spectrum under pressure is shown in Fig 4.29 for an applied pressure of 7 kbar.

The peak at the highest frequency, $F = 3894 \pm 10$ T, can be readily ascribed to the β orbit as it was observed, at a slightly lower frequency, in the ambient pressure experiments. It was actually under high pressure of 9 kbar that this frequency was observed for the first time by Kartsovnik *et al.* [68] who attributed it to the MB effect.

The strongest contribution in the FFT spectrum presented in Fig. 4.29 yields a frequency, $F = 143 \pm 3$ T, which corresponds to $\approx 4\%$ of the BZ cross-sectional area. This FS area is almost by a factor of 4 smaller than that enclosed by the α orbit observed at ambient pressure. Hereinafter, this frequency is referred to as α' frequency. It is followed by a frequency, $F = 294 \pm 5$ T, called $2\alpha'$ below in this work. Since $F_{2\alpha'}$ amounts to about the double value of $F_{\alpha'}$, it apparently

causes the non-sinusoidal shape of the α' oscillations. Both these low frequencies were found under pressure of ≈ 9 kbar on the occasion of the very first successful search for magneto-quantum oscillations in the κ -Br salt [34]. This experiment was limited to fields up to 17 T and temperatures higher than 1.4 K, that did not allow a detailed analysis of the oscillations.

As in these previous experiments, no frequency which could be identified with the conventional α orbit was detected in the present study. Owing to a systematic investigation of the SdH oscillations under pressure [71, 81, 106] in rather favorable experimental conditions by use of high quality samples, the present results can be regarded as the most reliable ones to date. With the corroboration of the unexpected results obtained in the first successful measurements [34, 68], it can thus be definitely concluded that, in contrast to what was found in the sister compounds [49, 69], the SdH oscillations under pressure cannot be straightforwardly explained by the FS model which was theoretically proposed [42] and which applies well to the SdH and dHvA oscillation frequencies observed at ambient pressure [70].

Several speculations about the origin of the unexpectedly low α' frequency can be put forward. If we adhere to the initially predicted FS topology (Fig. 4.6) and keep in mind that the gap between the open and cylindrical closed orbits is very small [42], we come to an extremely narrow α' orbit with its cross-section elongated along the X - M direction. Since the β orbit encloses an area of the size of the first BZ, this would entail an almost rectangular FS practically lying at the BZ boundary. Visentini *et al.* [103] pointed out that, due to an extended van Hove singularity near the Fermi level, this FS geometry would indeed occur in the extreme limit of a vanishing interdimer hopping integral along the crystal c direction or along the appropriate direction in the other κ -phase salts. It might be conceivable that this hopping integral is highly sensitive to pressure and the FS ends up in the mentioned geometry under high pressure. However, it is not clear why the hopping integral should drastically decrease with application of pressure in κ -Br but not in all the other κ -phase salts [49, 69]. Moreover, with a high sensitivity of the hopping integral to the pressure, also the position of the van Hove singularity close to the Fermi level should noticeably change with pressure, thus provoking a strong dependence of the size of the electron orbits onto the pressure, especially for the small α' orbit. In fact, the pressure dependence of $F_{\alpha'}$, although rather strong (see below in this chapter), does not exceed that observed for F_{α} in the κ -Cl and κ -NCS salts [49, 69]. Finally, as it was found for the α frequencies in the sister compounds, the α' frequency *increases* with pressure and thus behaves, at least for pressures higher than 5 kbar where the α' oscillations are visible, in the opposite direction than would be expected within the present hypothesis.

Alternatively, to explain the α' oscillations, one could recall reports on similar very low-frequency oscillations, corresponding to $\sim 1\%$ or even less of the BZ cross-sectional area, observed in some other organic metals, β -(BEDT-TTF)₂X with X = I₃ and IBr₂ (see e.g. Ref. [107]), θ -(BEDT-TTF)₂I₃ [108], κ -(BEDT-TTF)₂Cu₂(CN)₃ [109], and κ -(BEDT-TSF)₂C(CN)₃ [110]. In most cases the angular dependence of the oscillation frequency revealed a small *three-dimensional*

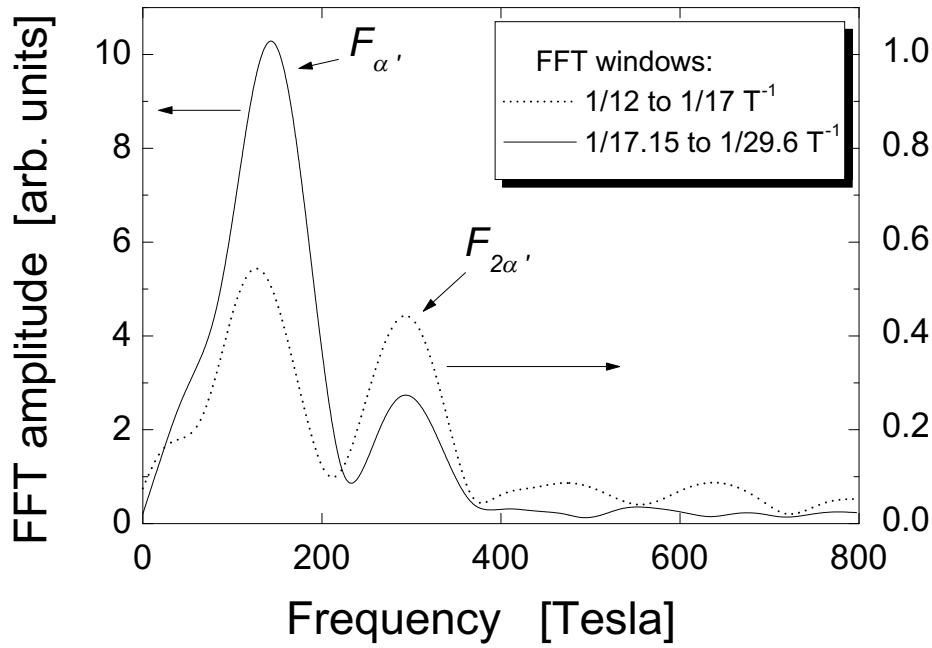


Figure 4.30: FFT spectra at 7 kbar taken in a high- and a low-field window of equal size in the inverse magnetic field scale.

FS pocket which could be associated with a contribution of the anion sheets to the conducting bands [107, 108, 109]. However, in the present compound the angular dependence of the α' frequency is typical of a cylindrical FS, at least up to tilt angles of $\sim 30^\circ$. The only resemblance to this situation is, to our knowledge, the case of β -(BEDT-TTF) $_2$ I $_3$ [107].

The hitherto mentioned scenarios take only account of the lowest-frequency α' oscillations that dominate in the spectrum but fail to explain the $2\alpha'$ oscillations. As was noted in Refs. [71, 34], the amplitude of the $2\alpha'$ frequency is too high to be interpreted as a second harmonic of the α' frequency. Moreover, it was found that its field dependence is drastically different from that expected for the second harmonic [81]. Fig. 4.30 shows the FFT spectra of the SdH oscillations at $p = 7$ kbar, $T = 0.6$ K, taken in different field windows of equal size in the inverse magnetic field scale. Whereas the contribution of the $2\alpha'$ oscillations is almost equal to that of the α' oscillations in the fields between 12 T and 17 T, it becomes by more than a factor of 3 smaller than the latter in the field window from 17.15 to 29.6 T. The relative decrease of the $2\alpha'$ contribution with increasing fields was reproduced at different pressures and on different samples.

One could suppose that the spin-splitting effect is responsible for the appearance of the $2\alpha'$ frequency. Indeed, when the spin-splitting damping factor, $\cos(\pi g m_{\alpha'}^*/2m_e)$, is close to zero, the amplitude of the fundamental frequency vanishes whilst the second harmonic is coming to its maximum amplitude. However, this could cause a relatively strong second harmonic content only at some specific pressure at which $\cos(\pi g m_{\alpha'}^*/2m_e) \approx 0$. In fact, the high ratio between the $2\alpha'$

and α' oscillation amplitudes is observed in a wide pressure range, between 5 kbar and 10 kbar; the spin-splitting damping factor, however, cannot remain very small at all the pressure values due to the changes in the effective mass $m_{\alpha'}^*$ with pressure (see below in this chapter). Moreover, the unusual field dependence of the ratio between the $2\alpha'$ and α' oscillation amplitudes (Fig. 4.30) as well as the monotonic angular dependence of the α' oscillation amplitude [34] evidence against the spin-splitting effect as a possible reason of the relatively strong amplitude of the $2\alpha'$ oscillations.

All oscillation parameters did not show any sharp transition or significantly strong changes under pressure that could indicate a pressure-induced phase transition being responsible for the drastic change in the frequency spectrum. Taking into account only moderate pressure dependences of the oscillation frequencies obtained in the present experiments, it is also unlikely that this unexpected behavior is caused by a gradual variation of the crystal lattice under pressure. Hence, the specific features characteristic of the FS found at ambient pressure [70] can be expected to remain the same at high pressures.

In the following, an alternative explanation of the experimental results is proposed [81, 106]. It is based on a superstructural transition below 200 K observed in an X-ray study at ambient pressure [55]. The superstructure found in that work causes a doubling of the high temperature lattice along the c direction. In the \mathbf{k} -space it consequently reduces the original BZ along the k_c -axis and gives rise to new BZ boundaries at $\pm k_c/4$. This should lead not only to a folding of the α pocket shown in Fig. 4.6, as suggested by Nogami *et al.* [55], but to a qualitative change in the entire FS topology. A two-dimensional representation of the modified FS obtained by application of the standard Harrison construction [111] to the original FS cylinder is shown in Fig. 4.31(a) in the reduced zone scheme. It reveals an electron-like “bone” in the center and a hole-like “star” and “pocket” in the corners of the reduced BZ. Special investigations are necessary to evaluate the interband gaps Δ_0 , Δ_1 , and Δ_2 [Fig. 4.31(a)]. One can suppose that Δ_0 is essentially the same as the gap between the open and closed parts of the unmodified FS, while Δ_1 and Δ_2 are totally governed by the superstructure and may be similar to each other in magnitude. All these gaps are likely small enough to allow strong MB effects at the present experimental conditions. The two-dimensional network of possible MB orbits in \mathbf{k} -space is shown in Fig. 4.31(b). Depending on the gap values as well as the magnetic field strength, several orbits can be realized. In order to explain the difference in the oscillation spectrum between the states at ambient pressure and under pressure within the present model, we can assume the gap Δ_0 to be larger than any other gap, $\Delta_0 > \Delta_1, \Delta_2$, at ambient pressure. In moderate magnetic fields, this would give rise to predominantly MB at Δ_1 and Δ_2 but Bragg reflection at Δ_0 and thus lead to the realization of the α orbit. At fields high enough to allow for MB also at Δ_0 , carriers will populate the β orbit and contribute to magneto-quantum oscillations, as well. Under pressure, at least the gap Δ_1 is suggested to become more significant, thus suppressing the α orbit and giving rise to new smaller orbits. For $\Delta_1 > \Delta_0, \Delta_2$ the main non-equivalent carrier orbits would be represented by the orbits 1 and 4 in Fig. 4.31(b) or, with

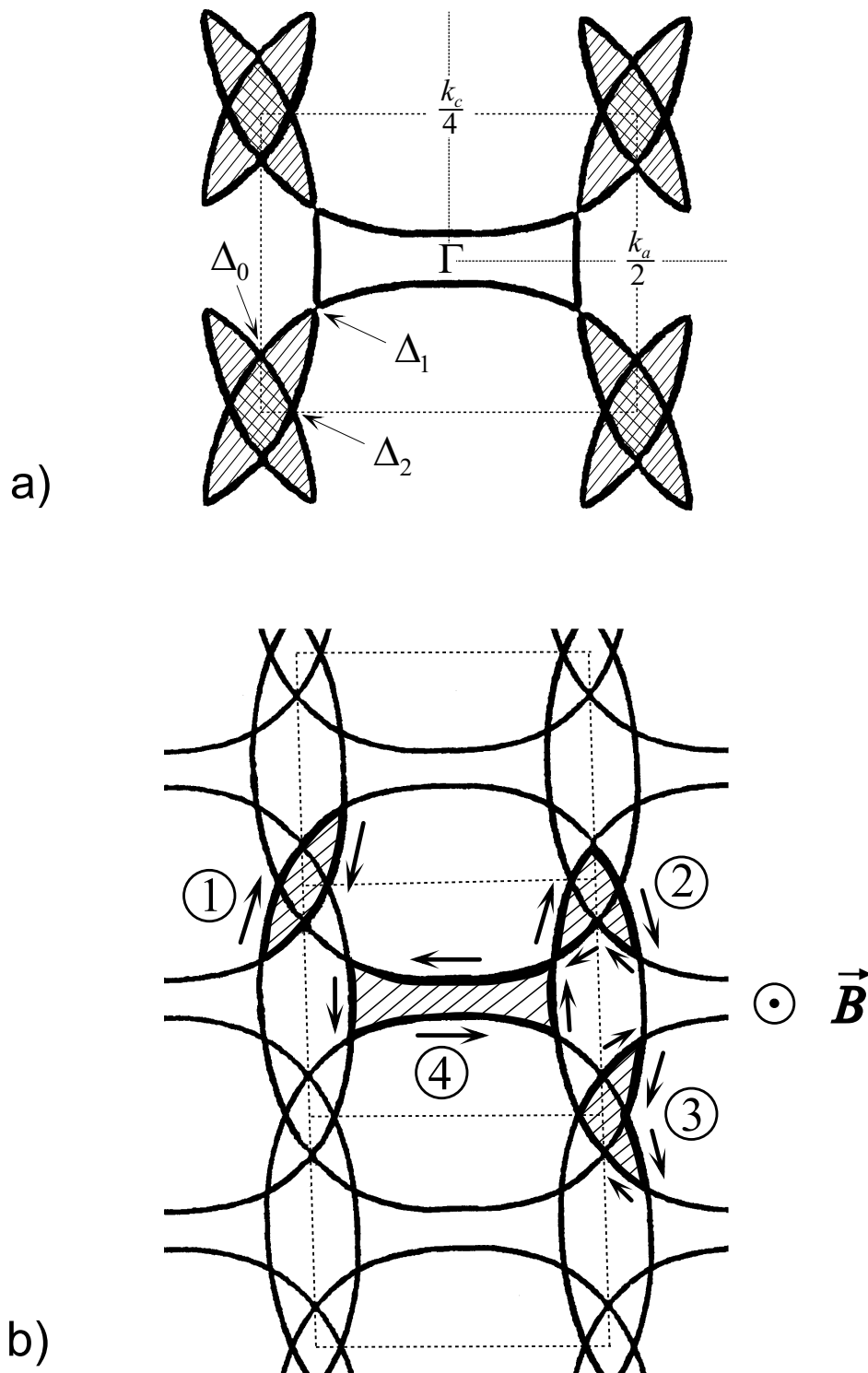


Figure 4.31: (a) New FS configuration caused by doubling the room-temperature c -axis. It consists of an electron-like “bone” around the center of the new BZ and a hole-like “star” (hatched and double-hatched areas) and a “pocket” (double-hatched area). (b) Possible orbits on the FS depicted in Fig. 4.31(a). The arrows indicate the carrier motion for a magnetic field pointing out of the plane.

$\Delta_0, \Delta_1 > \Delta_2$, by 2 and 4, or, with $\Delta_1, \Delta_2 > \Delta_0$, by 3 and 4.⁹ It is likely that combinations of several or even all the mentioned orbits are realized in the experiment. Based on the theoretically calculated FS [42] the orbits 1, 2 and 3 each enclose an area as large as $\approx 3.8\%$ of the cross-section of the reduced BZ. This is in excellent agreement with the experimental value $F_{\alpha'}$ extrapolated to low pressure. Further, if we conventionally assume that the κ -Br salt is a compensated metal, the area enclosed by orbit 4 turns out to amount to about 2 times the above value. This perfectly fits the observation of the $2\alpha'$ oscillations. Noteworthy, the increase of the magnetic field, entailing the increase of the MB probability, redistributes the relative weights of different orbits; in particular, the probability for the realization of orbit 1, involving 2 junctions at which carriers undergo Bragg-like reflection and 4 junctions at which they tunnel through the gap, decreases slower than the probability for the realization of the classical orbit 4 which requires the carriers to be reflected in all the 4 MB junctions. This can explain the relative reduction of the $F_{2\alpha'}$ amplitude with respect to that of $F_{\alpha'}$ in high fields (Fig. 4.30). In high enough magnetic fields, there is a finite probability for MB at all interband gaps and the β orbit will be realized in the same geometry as it is found at ambient pressure.

The present model is in line with the observation of β oscillations only at higher fields in κ -Br compared to the closest related compound κ -Cl. In the latter salt, β oscillations were found already at fields as low as ≈ 10 T under pressure of about 7 kbar and at 1.4 K [49], whereas in the κ -Br they appear not below 20 T at the same conditions. This may be explained by the fact that the β orbit of the reconstructed FS of κ -Br exhibits 16 junctions where MB or Bragg reflection can occur, whereas the β orbit of the κ -Cl compound contains only 4 such junctions. According to Eq. (2.18) we should thus indeed expect a much enhanced field threshold for the β oscillations in κ -Br if we assume the interband gaps to be of comparable size in both systems.

In the following, some pressure dependences obtained by the present study [71, 81, 106] are discussed, assuming the above given model to apply to the κ -Br system.

4.6.3 Pressure Dependences

Oscillation Amplitudes

The oscillation amplitudes of the α' and β oscillations follow opposite tendencies with varying pressure. Within the measured field and pressure intervals, the α' oscillation amplitude essentially grows with increasing pressure, whereas that of the β oscillations nearly linearly decreases from ambient pressure up to about 10 kbar. At higher pressures no β oscillations were observed. The ratio between both amplitudes, obtained by FFT's in the field window 17.5 T to 25.9 T is shown

⁹For the sake of clarity, only the non-equivalent MB orbits are shown in Fig. 4.31(b) but not MB orbits that can be obtained by mirror reflections of these orbits at the Brillouin zone boundaries; of course, they also contribute to the MB spectrum.

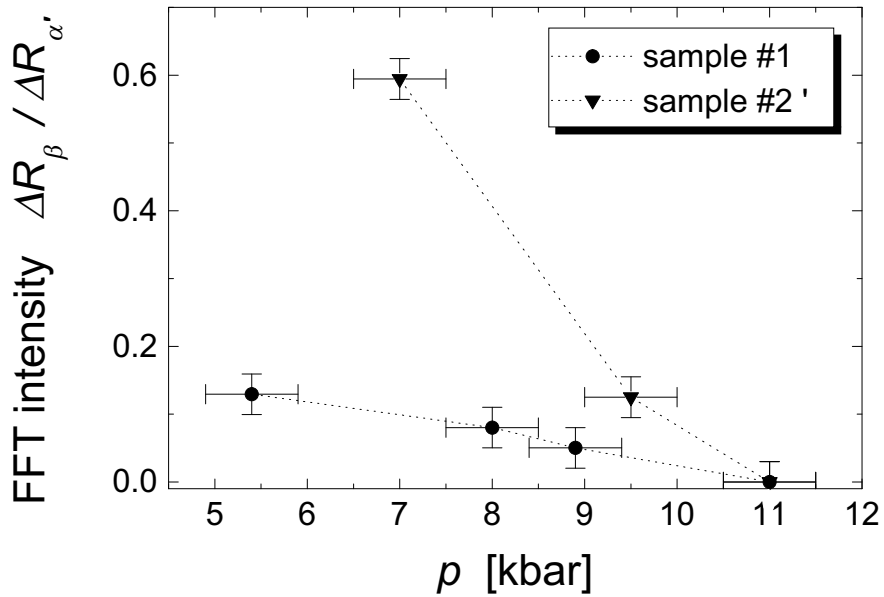


Figure 4.32: Ratio between the amplitude of the β and α' oscillations as a function of pressure. The ratio is obtained by comparing the height of the corresponding peak intensities of FFT's performed in the field window 17.5 T to 25.9 T.

in Fig. 4.32. The present behavior can be understood, assuming one or more of the interband gaps Δ to be continuously enlarged with pressure. Such feature may result from a reduction of the orthorhombic symmetry of the crystal structure with pressure. This would gradually suppress the MB probability at the respective junctions and let the β oscillations fade with pressure. The decrease in the MB probability would lead to an enhancement of the probability for Bragg reflection and thus entail the intensity increase of the smaller orbits, 1, 2, 3, and 4, as discussed in the previous section.

The amplitude of the $2\alpha'$ oscillations is most pronounced at pressures of about 6 kbar to 10 kbar. This may be a sign for the gap Δ_0 or Δ_2 increasing stronger with pressure than Δ_1 . At high pressures, this would favor the orbits 1, 2, or 3, that require at most two Bragg reflections at Δ_1 instead of four for orbit 4.

Summarizing, the interband gap Δ_0 is suggested to be the largest one at ambient pressure. At ambient pressure, its size allows for MB as well as Bragg reflection. With gradually increasing pressure, the gaps Δ_1 and Δ_2 continuously open up, that results in a distinct probability for Bragg reflection at these junctions. At the pressure threshold of ≈ 10 kbar, the size of one or several gaps is large enough to prevent the realization of the β orbit. The interband gaps Δ_0 and Δ_2 probably grow more rapidly with pressure than Δ_1 .

Compared to the sister compounds, the behavior found in κ -Br differs from that in κ -NCS [69] which shows a decrease of the gap Δ_0 (in the present notation) with increasing pressure. On the other hand, it resembles to the behavior of κ -Cl in which the amplitude of the β oscillations decreases with increasing pressure

[49]. Of course, it should be kept in mind that the gaps Δ_1 and Δ_2 have likely a different nature from the gap Δ_0 in the other κ -phase salts.

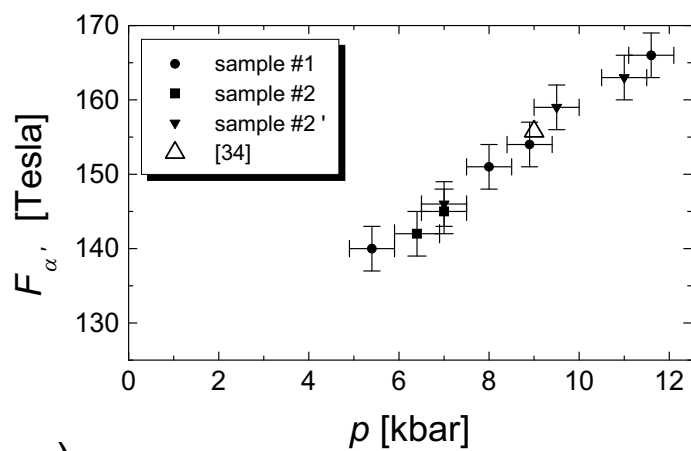
As it is seen in Fig. 4.32, the intensity ratio of the β and α' oscillations is different for different samples. At the same time the other electronic properties are essentially the same. More extensive comparative studies on different samples are needed to be able to find an answer to this behavior.

Oscillation Frequencies

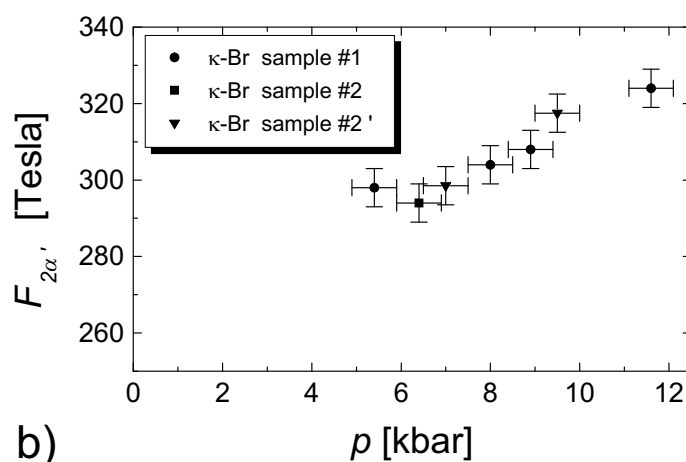
As compared to ordinary metals that usually exhibit quite weak relative dimensional changes with pressure and thus only slight changes in the quantum oscillation frequencies ($\Delta F/F \sim 1\%$ per 10 kbar) [9], the frequencies found in organic compounds are highly sensitive to pressure.

The pressure dependences of the α' , $2\alpha'$, and β oscillation frequencies of κ -Br are illustrated in Figs. 4.33(a), (b), and (c), respectively. Within the studied pressure range, all the three frequencies increase to a good approximation linear with increasing pressure. The frequency of the α' oscillations exhibits the highest rate, $d \ln F_{\alpha'}/dp \approx 0.03 \text{ kbar}^{-1}$. A slight decrease of the ratio between the frequencies $F_{2\alpha'}$ and $F_{\alpha'}$ with pressure was noticed. This tendency is smaller than the error bars and therefore needs further investigation for a reliable corroboration. However, it would represent another argument for the $2\alpha'$ frequency originating from a separate orbit rather than being the second harmonic of the α' oscillations. The relative pressure dependence of the β oscillation frequency is found to $d \ln F_{\beta}/dp \approx 3.8 \times 10^{-3} \text{ kbar}^{-1}$. It is thus almost by a factor of 10 weaker than that of $F_{\alpha'}$. Since the area enclosed by the β orbit is strictly determined by the BZ dimension and equals the double area of the modified BZ at all pressures, the pressure dependence of the β oscillation frequency is expected to follow the behavior of the crystal lattice compressibility component in the highly conducting plane. This supposition is justified, as the compressibilities of the crystallographic axes are highly isotropic [65, 112]. Indeed, the obtained value agrees with the compressibility typical of the κ -salts [65, 112].

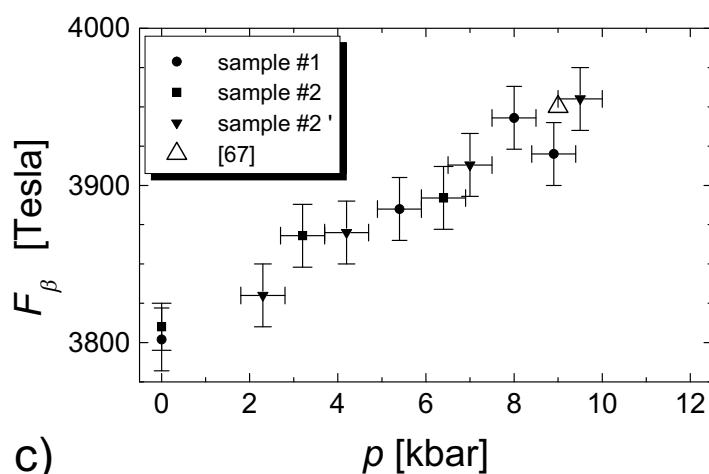
The pressure dependences of the α' and β oscillation frequencies in κ -Br closely resemble to those found in the sister compounds κ -Cl [49] and κ -NCS [69]. As it is seen in Fig. 4.34, especially the pressure dependence of the β oscillation frequency perfectly coincides with those reported for the κ -Cl [49] and κ -NCS [69] that were studied in the pressure ranges of 4 kbar to 9.7 kbar and from ambient pressure up to 16.3 kbar, respectively. In both sister compounds, the α oscillation frequency increases markedly stronger with pressure than the β frequency. In Ref. [69] it is argued that anisotropic changes of the FS shape with pressure that entail a gradual elongation of the β orbit along the direction of intercoupling between different β orbits in the extended zone scheme are responsible for this behavior. In the κ -Br compound, similar changes elongating the β orbit along the k_a direction are likely to enlarge the orbit 4 as well as the orbits 1, 2, and 3 with pressure to a higher extent than the β orbit. Regarding the slope of $F_{\alpha'}(p)$ in Fig. 4.34(a), the increase in the area of the α' and $2\alpha'$ orbits is considerably steeper than that of the



a)



b)



c)

Figure 4.33: Pressure dependences of the (a) α' , (b) $2\alpha'$, and (c) β oscillation frequencies. The values reported from the first successful measurements are included for comparison.

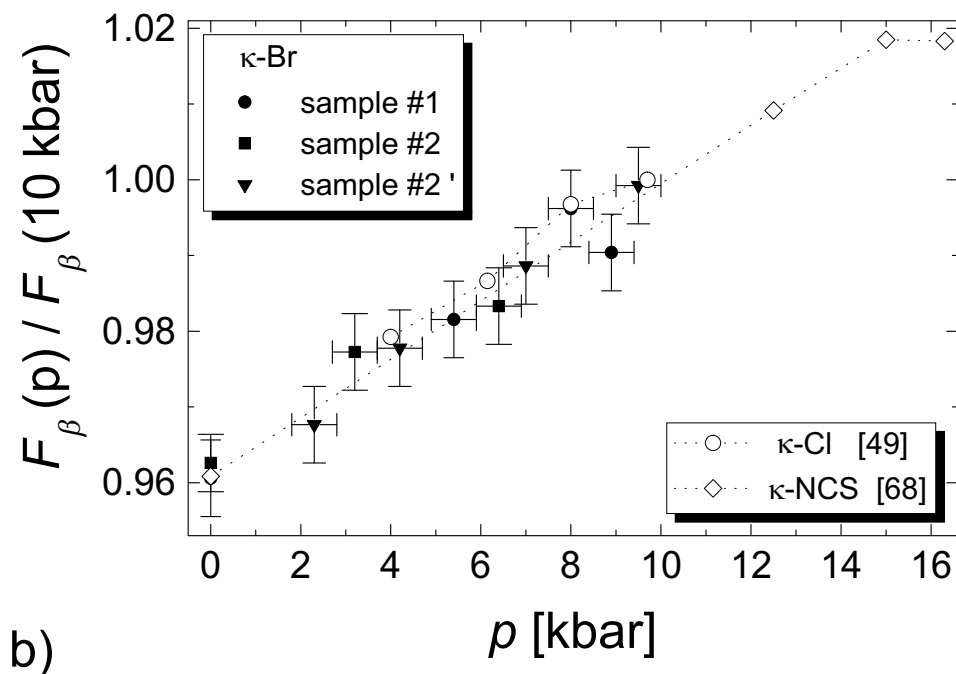
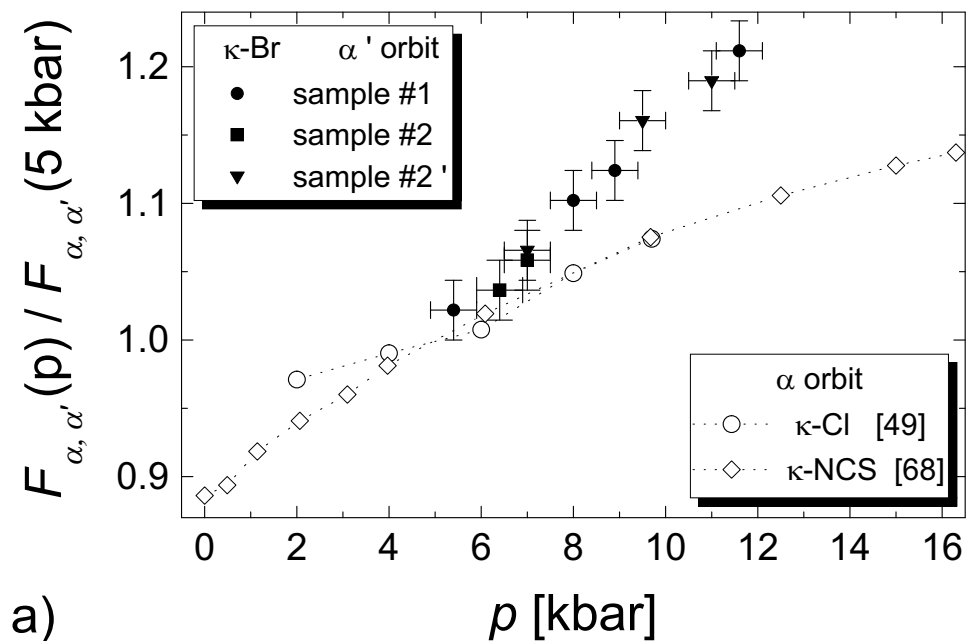


Figure 4.34: (a) Frequencies of the α' oscillations in κ -Br and of the α oscillations in κ -Cl and κ -NCS, normalized to the values at 5 kbar. (b) β oscillation frequencies of κ -Br, κ -Cl, and κ -NCS, normalized to the values at 10 kbar.

regular α orbit in the sister compounds. This may hint to an even more significant deformation of the β orbit with pressure in the κ -Br salt.

Effective Cyclotron Masses

The pressure dependence of the cyclotron mass of the carriers that trace the α' orbit is displayed in Fig. 4.35(a). The value at 9 kbar is nearly the same as reported earlier [34]. Like m_α^* in κ -NCS [69] and κ -Cl [91], $m_{\alpha'}^*$ monotonically decreases with increasing pressure. Compared to the cyclotron mass m_α^* in the κ -NCS salt [69], $m_{\alpha'}^*$ of the present compound is approximately two times smaller and lies also below the values which are found for m_α^* of κ -Cl [91].

As for the cyclotron mass of the electrons on the β orbit shown in Fig. 4.35(b), it is close to that in the κ -NCS salt at ambient pressure [73, 48, 82] and nearly equals m_β^* of κ -Cl at all pressures [91]. Starting from ambient pressure, m_β^* decreases by about 50% up to the pressure of 5-6 kbar and then remains nearly constant up to the highest pressure at which the β oscillations were visible.

The values found for $m_{\alpha'}^*$ and m_β^* fit well into the FS model given above: On the one hand, the main parameters of the β orbit, i.e., its area and m_β^* , are very close to the values obtained for κ -NCS and κ -Cl. On the other hand, $m_{\alpha'}^*$ is approximately two times smaller than m_α^* reported for the other two salts. In the approximation of parabolic energy band dispersion and neglecting any many-body interactions, the cyclotron mass is proportional to the square root of the orbit area. Then, the area of the α' orbit [orbits 1,2, and 3 in Fig. 4.31(b)] is expected to be approximately 4 times smaller than the area of the α orbit in the sister compounds, in agreement with the experimental result.

However, regarding the effective cyclotron mass associated with the $2\alpha'$ orbit, this approximation fails to provide a conclusive description. Fig. 4.36 displays $m_{2\alpha'}^*$ for several pressures. Although these values have a larger error bar, due to a lower oscillation amplitude, it can be seen that $m_{2\alpha'}^*$ follows a similar pressure dependence as $m_{\alpha'}^*$ but is nearly by a factor of 2 as high as $m_{\alpha'}^*$. The values of the effective cyclotron mass associated with the $2\alpha'$ orbit are thus in the range of the values for m_α^* found for the about two times larger α orbit in the sister compounds [Fig 4.35(b)]. At a first glance, this behavior would support the assumption that the $2\alpha'$ orbit is not an independent orbit rather than the second harmonic of the α' orbit. In this case, the effective cyclotron mass values of the second harmonic, treated as those of a fundamental, would amount to the double values of the actual fundamental. However, as detailed in the beginning of the present section, there is convincing evidence against the $2\alpha'$ oscillations being the second harmonic of the α' oscillations. Provided that the approximation of a parabolic energy band dispersion can be applied, the unusually enhanced value of $m_{2\alpha'}^*$ might thus more likely be an indication that the carriers on the $2\alpha'$ orbit are more strongly involved in many-body interactions than those tracing the α' orbit.

Fig. 4.35(a) and (b) indicate that the decrease in effective mass with increasing pressure seems to be a universal feature of the κ -phase BEDT-TTF salts; the values of m_β^* of the three different compounds shown in Fig. 4.35(b) even map onto

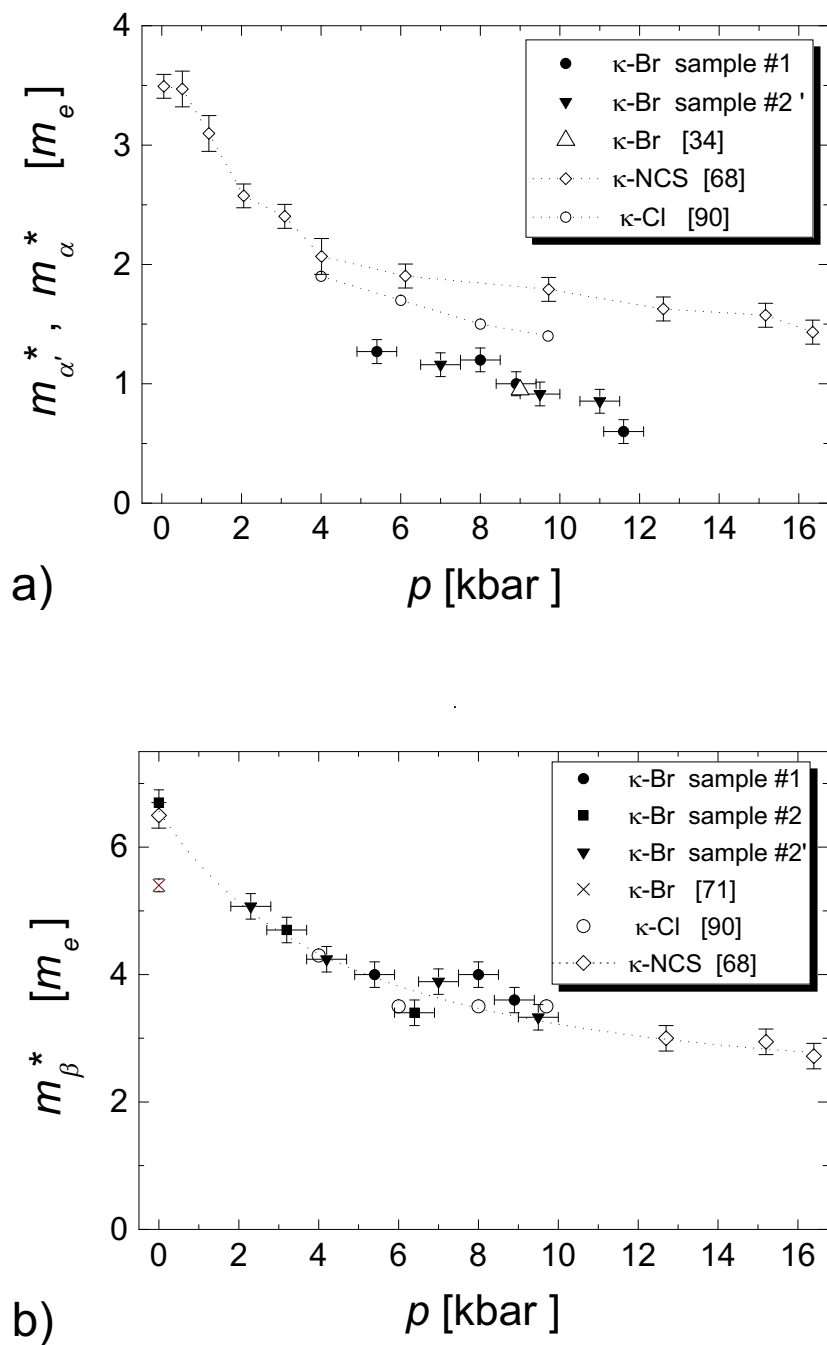


Figure 4.35: (a) Pressure dependence of the effective cyclotron mass of the electrons associated with the α' orbit. In addition to the mass $m_{\alpha'}^*$ of κ -Br, the cyclotron masses m_{α}^* of the compounds κ -NCS and κ -Cl are depicted for comparison. (b) Pressure dependence of the effective cyclotron mass of the electrons tracing the β orbit of κ -Br as well as of the sister compounds. The dotted line is a guideline corresponding to the data of κ -NCS that are available for ambient pressure and $p > 12$ kbar.

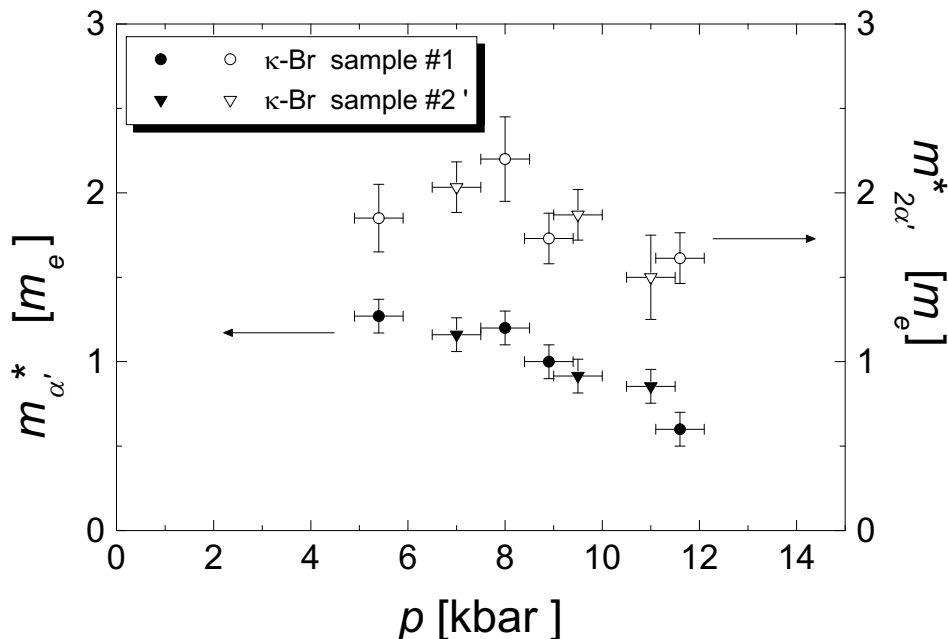


Figure 4.36: Pressure dependence of the effective cyclotron mass of the electrons associated with the $2\alpha'$ orbit (open symbols) along with the values for $m_{\alpha'}^*$ (solid symbols).

a common curve as a function of pressure. Inspired by the results obtained for the κ -NCS salt, Caulfield *et al.* [69] proposed to separate the pressure dependences of the effective cyclotron masses of the κ -phase salts into two distinct regimes. A low-pressure region exhibiting a strong approximately linear decrease of the effective cyclotron masses with pressure and another region at high pressures with a much lower value of dm^*/dp . Based on their finding that the effective mass enhancement is mainly due to carrier-carrier interactions [113, 69] these authors attribute the rapid variation of the effective cyclotron mass at low pressures to the suppression of a component of the carrier-carrier interactions which depends critically on the pressure dependent bandwidth. The further only very weak pressure dependence of m^* is considered to merely reflect the increasing bandwidth with pressure. They argue that the initial strong decrease of the effective cyclotron masses thus corresponds directly to the decrease of T_c which is connected to the effective masses via the carrier-phonon coupling constant λ . According to that work, this correlation should not only apply to the pressure dependence of T_c and m^* of one compound but also to the dependence of these quantities on the “chemical pressure” as represented by different compounds exhibiting different intermolecular coupling strengths that govern the bandwidth. Since changes in the effective mass should be proportional to changes in the electronic density of states at the Fermi surface, one should expect a general tendency of T_c increasing with the density of states at the Fermi level. Contrary to that, other works that compare the different densities of states at the Fermi level due to different strengths of intermolecular coupling in several quasi-two-dimensional organic su-

perconductors [114, 64], thus comparing different states of “chemical pressures”, indicate that there is no conclusive relationship between T_c and the density of states. A recent discussion of the structural principles exhibited by the κ -Br, κ -Cl, and κ -(BEDT-TTF)₂Cu[N(CN)₂]I salts and several of their mixed compounds [115] rather provided evidence for a strong control exerted by disorder of the ethylenedithio groups on the superconducting critical temperatures in the κ -phase salts. Hence, the interplay between T_c , the densities of states at the Fermi surface, and the effective cyclotron masses is likely not as straightforward as assumed by Caulfield *et al.*

It is not excluded that the decrease of m_β^* , observed in the present experiment, is related to the suppression of superconductivity. The data shown in Fig. 4.35(b) do not allow to definitely speak of a sharp crossover between a steep pressure dependence of the mass below and nearly constant mass above the pressure at which the superconducting critical temperature vanishes. A possible crossover may take place at $p = 6$ kbar. However, the superconductivity is already suppressed at $p \approx 5$ kbar. Concerning the effective cyclotron mass of the carriers tracing the α' orbit, it cannot be drawn any conclusion on this matter since no oscillations were observed in the pressure range below 5 kbar which exhibits the superconducting state at low temperatures.

Dingle Temperature

As already mentioned in connection with the dHvA measurement, the estimation of the Dingle temperature is limited in its accuracy for several reasons. The present analysis is therefore not primarily focussed onto an accurate determination of the Dingle temperature but rather aims to unveil its pressure dependence.

The β oscillations are likely affected by a beating effect not only at ambient pressure, as detailed in the previous section, but also under pressure, as will be shown below. Since no information about the beat frequency could be obtained, the actual Dingle damping factor for these oscillations cannot be reliably determined. Although the α' oscillations exhibit only a few periods within the studied field range, that leads to a not negligible statistical error in the analysis of the field dependence of the oscillations, they may provide a sufficiently reliable basis for the estimation of the Dingle temperature. Of course, as for the α oscillations at ambient pressure, an additional error may arise from a possible beating effect influencing the α' oscillations, even if it is not observed in the available field interval.

For the present analysis roughly two regimes have to be considered: The high-pressure region, where the MB β oscillations are nearly completely suppressed, and the region of intermediate pressure, where these oscillations are clearly visible. For the former pressure range the MB probability is sufficiently low to put the MB reduction factor (Eq. 2.18) for the α' orbit equal to unity. If we assume the MB field, B_0 , to be higher than 10 T, the Dingle temperature is thus underestimated by not more than ≈ 1 K. At intermediate pressures the breakdown field is believed to lie well below the MB field $B_0 = 30$ T which was found for the thoroughly

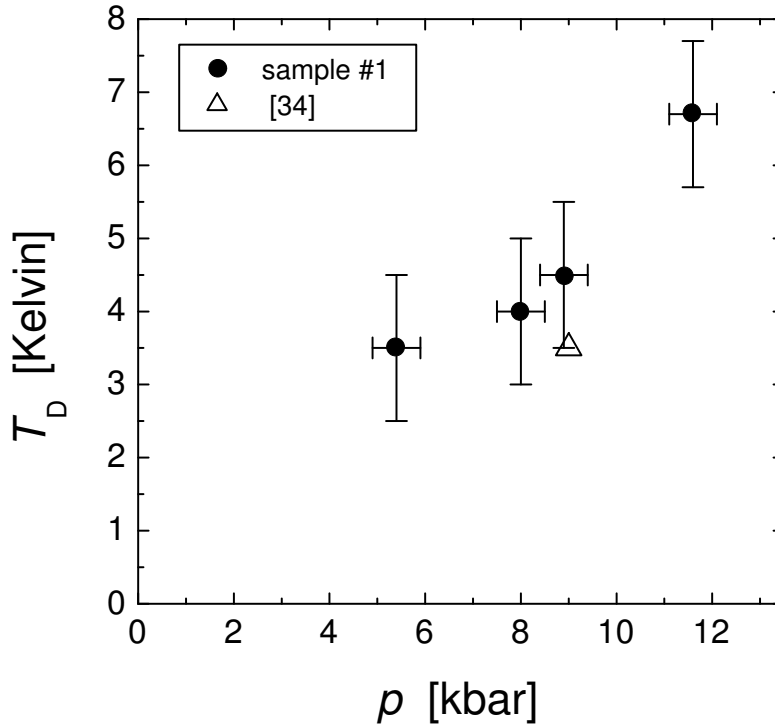


Figure 4.37: Pressure dependence of the Dingle temperature of the α' oscillations along with the value reported by Kartsovnik *et al.* [34].

investigated $\text{Cu}(\text{NCS})_2$ salt [82]. For possible MB field values between this maximum limit and 0.1 T, the Dingle temperature varies by less than 1 K. The same considerations apply for the $2\alpha'$ oscillations. For the correct estimation of the MB field reduction factor it has to be taken into account that for the $2\alpha'$ orbit the number of junctions, where Bragg reflection occurs, amounts to 4 instead of 2 or 3 for the α' orbit.

Since the oscillation frequencies of the α' and $2\alpha'$ oscillations is of the same order of magnitude, the magnetic field dependence of their oscillation amplitudes cannot be directly measured by the envelope of the oscillations. Hence FFT's over equivalent inverse magnetic field intervals, containing about three α' oscillation periods, were performed in steps of one oscillation period and the FFT intensities of the α' and $2\alpha'$ oscillations were measured. The resultant pressure dependence of the Dingle temperature of the α' oscillations is shown in Fig. 4.37.

$T_{D,\alpha'}$ clearly increases with pressure, that implies a carrier scattering time which decreases with pressure. Since the scattering time is renormalized by the cyclotron energy, we cannot directly infer a higher density of scattering centers from this result. Considering the decreasing effective cyclotron mass with pressure, we obtain a carrier velocity which grows with pressure. With regard to the mean free path, $l_{\alpha'}$, the increase in the carrier velocity is overcompensated by the strong decrease of the carrier scattering time. Altogether, we estimate $l_{\alpha'}$ to decrease by about 25% from 5 kbar to 12 kbar. An obvious explanation for this behavior is a

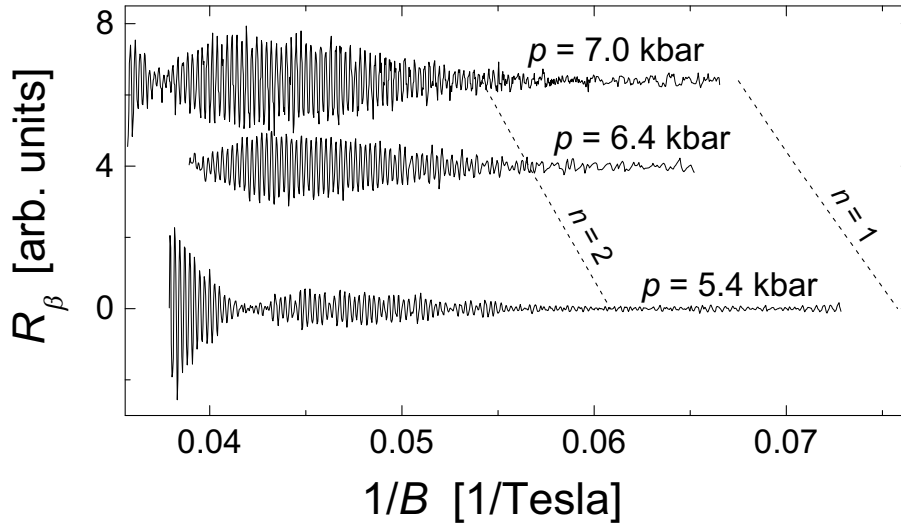


Figure 4.38: Beats in the β oscillations at different pressures. The values $R_\beta(B)$ are obtained by the inverse FFT's of the Fourier spectra of the original $R_{osc}(B)/R_0(B)$ curves [$R_0(B)$ is the background semi-classical resistance], after eliminating the low-frequency peaks. The dashed lines outline the next nearest node positions as they were expected if the observed node was the second node ($n = 1$) or the third node ($n = 2$) coming from high fields.

growing number of lattice defects such as inhomogeneous strain and dislocations as the pressure is gradually increased.

The analysis of the Dingle temperature of the $2\alpha'$ oscillations is less accurate than that of the α' oscillations, since the $2\alpha'$ oscillation amplitude is very weak in the available field interval. However, beyond the uncertainty of the enhanced error bar, it turns out that the value of $T_{D,2\alpha'}$ is by at least a factor of 2 lower than that of $T_{D,\alpha'}$ at all pressures. If we take account of the effective cyclotron mass values associated with the $2\alpha'$ orbit that are about two times higher than those associated with the α' orbit, and assume a parabolic energy dispersion, the mean free path $l_{2\alpha'}$ takes values that are in the same range as those of $l_{\alpha'}$. This estimation implies that the carriers on both orbits feel approximately the same density of scattering centers.

4.6.4 Beating Effect

In the pressure range between 5 kbar and 8 kbar the β oscillations show distinct beats [81], with the beat nodes shifting to higher fields with pressure. This is illustrated in Fig. 4.38 which presents the oscillatory signals of curves at different pressures after filtering out the low frequency components.

This beating effect is probably of the same origin as that found in the dHvA β oscillations at certain magnetic field directions [70] (see section 4.2.2). I.e., it is likely due to a warped structure of the FS along the k_b direction in the \mathbf{k} -space. As in the dHvA oscillations at ambient pressure, the beat frequency under

pressure was not high enough to allow the observation of more than one node in the field interval in which the β oscillations were observed. Nevertheless, if we assume the phase factor $\pm\pi/4$ in Eq. (2.9) to take the value $\mp\pi/4$ for the SdH oscillations, as it was suggested in Ref. [102], the beating behavior under pressure can be characterized in more detail. First, as was shown in section 4.4.2, with this assumption the first node ($n = 0$) coming from high fields should exist in the ambient pressure SdH oscillations above 100 T whereas the second node ($n = 1$) should lie at about 20 T, i.e., at a lower field than the node positions observed under pressure. Provided that the strength of warping exhibits a monotonic pressure dependence the nodes observed under pressure are thus characterized by $n \geq 1$. Further, if no abrupt changes occur in the pressure dependence of the strength of warping the observed node is the same ($n = \text{const.}$) at all pressures. Considering the smooth monotonic pressure dependence of the oscillation parameters these assumptions concerning the warping strength are the most natural ones. The observed positions of the nodes allow to calculate possible values for the beat frequencies, $\Delta F_\beta = B_{\text{node}}(4n + 1)/4$ [cf. Eq. (4.2) modified by the beating phase shift $\pi/2$ [102] suggested for the SdH oscillations], at every pressure. As indicated in Fig 4.38, only two values, $n = 1$ or $n = 2$, come into question. For these n the next nodes at lower fields are expected around 14 T and around 17.5 T, respectively. At ~ 14 T, no β oscillations could be observed at all. At ~ 17.5 T, β oscillations could be detected but no obvious node was observed. However, at this field the oscillation amplitude is too low to definitely decide about the existence of a node in the experimental data, especially when the maximum and minimum orbits contribute with slightly different oscillation amplitudes so that the amplitude at the node does not completely vanish. All values $n > 2$, however, can be certainly excluded since in these cases additional nodes should be clearly observed within the available field range. Fig. 4.39 shows the expected beat frequencies according to the possible values $n = 1$ or $n = 2$ for different pressures. If the node observed under pressure is characterized by $n = 1$, i.e., it is the second node coming from high fields, the warping strength would only slightly increase by about 20% from the ambient pressure value $\Delta S_\beta/S_\beta = 0.71\%$ up to 7 kbar. Moreover, a noticeable pressure dependence would set in only at high pressures. In the case that the observed node is the third node ($n = 2$) coming from high fields, the pressure dependence of the warping strength would be much stronger with $\Delta S_\beta/S_\beta$ growing approximately linear up to twice its ambient pressure value at 7 kbar, reflecting a doubling of the interlayer bandwidth within this pressure range.

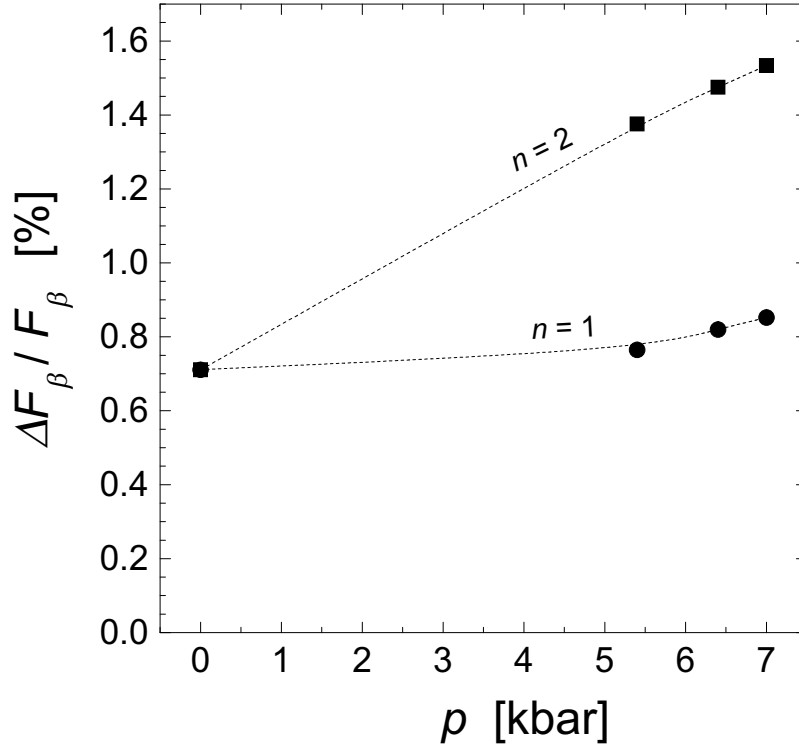


Figure 4.39: The two possible sets of values for the normalized SdH β oscillation beat frequency, based on the assumption that the SdH beat frequency is shifted by $\pi/2$ with respect to that expected from the LK formula [Eq. (2.9)]. The lower set corresponds to the situation where the observed node is characterized by $n = 1$, the upper one corresponds to $n = 2$. The dashed lines are tentatively suggested pressure dependences.

Chapter 5

de Haas-van Alphen Oscillations in NaBa_3N

5.1 The Sample

5.1.1 The Alkaline Earth Metal Subnitride NaBa_3N

For more than 20 years the unusual chemistry of alkali metal suboxides¹ seemed to be unique for its peculiar bonding situation. The members of this family contain oxide ions surrounded octahedrally by alkali metal atoms, where two or three octahedra are connected via common faces to form suboxide clusters. These clusters are strongly held together by ionic bonding inside the cluster whereas the bonding between different clusters is much like that of the native metal itself. Thus, these compounds may be described as complex metals where the single ion cores of the normal metal are replaced by clusters that are repulsive to the conduction electrons. Expressed in more vivid words, the ion clusters act as repulsive Coulomb bubbles to conduction electrons and make this material a foamed metal. This peculiar bonding situation has been shown to be responsible for noteworthy physical properties: the Fermi level of such a metal is raised and the work function is lowered. Thus, e.g., Cs_{11}O_3 has a lower work function than metallic Cs. Experimental evidence for this feature was found in specific heat [116], Raman [117], reflectivity [118] and photo electron spectroscopy [119] studies. Calculations for a simplified model of a void metal show this effect to be due to a quantum size effect [120]. The quantum confinement of the electron gas to the intercluster region raises the electron kinetic energy and thus the Fermi energy with respect to the vacuum level. As a practical application, this effect is widely used since more than 50 years in infrared photocathodes, where suboxide formation plays a crucial role in the active surface material.

By way of attempting an extension of the structural principles of alkali metal suboxides to alkaline earth metal subnitrides, first the discovery of NaBa_3N [121]

¹The term *suboxide* indicates that the stoichiometry of the compound exhibits a deficiency of oxygen compared to the metal in its normal oxidation state. These materials are therefore also called metal rich compounds.

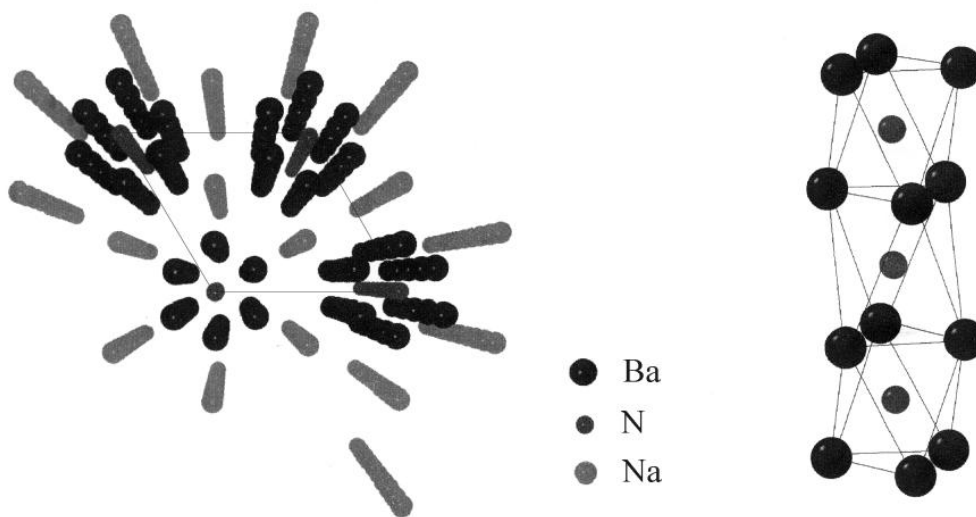


Figure 5.1: Crystal structure of NaBa₃N projected along the hexagonal c axis [121]. The rhomb outlines the basal plane of the unit cell. For clarity, the Ba₃N chain is shown in an enlarged side view.

and then that of further compounds with the general structures Na _{x} Ba _{y} N [122, 123, 124, 125] and also Na _{x} Ba₁₄CaN₆ [126, 127, 128] has opened the door for an even more colorful chemistry. In close analogy to the alkali metal suboxides, the family of alkaline earth metal subnitrides yields structures of discrete clusters but also infinitely extended one-dimensional chain configurations embedded in a metallic matrix.

The compound NaBa₃N contains parallel chains of Ba₃N, where the Ba₆N units in the chain are deformed into elongated trigonal antiprisms due to Coulomb repulsion between the N³⁻ ions (Fig. 5.1). Counting of valence electrons in the NaBa₃N compound leads to a Na⁺{[Ba²⁺]₃N³⁻}·4e⁻ charge formulation. According to this formula, the bonding between barium and nitrogen is predominantly ionic, while the remaining conduction electrons are delocalized over the rest of the space and are responsible for the metallic properties of the whole system. This view of the bonding situation in NaBa₃N finds additional support in structural properties: The Ba-N distance is indeed characteristic of heteropolar bonds whereas the sodium atoms exhibit metal-like interatomic distances. The sodium atoms are distributed in the periphery of the chains corresponding to most effective space filling and contribute a constant volume independently from the stoichiometric composition of Na _{x} Ba _{y} N and Na _{x} Ba₁₄CaN₆. This indicates that the sodium atoms are not involved in any electron transfer to nitrogen atoms but are of purely metallic nature. Analogously to the alkali metal suboxides one may visualize the NaBa₃N compound as a metal drilled with a periodic array of atomic scale bores that are expected to be repulsive to conduction electrons. This system would thus represent the first example of an anti-quantumwire configuration, the antitype to the widely investigated class of one-dimensional metals.

Although a void metal structure, characterized by separated regions of ionic

and metallic bonding, is the most likely one for the NaBa_3N as well as for the alkali metal subnitrides in general, it is still hypothetical so far. The investigation of physical properties that are closely related to the crystal and electronic structure is needed to put this view of bonding on safe quantitative ground. The search for the occurrence of the quantum size effect as it was found in alkali metal suboxides is certainly of special interest. Appropriate experiments would be optical electron spectroscopy and specific heat measurements as they were done for the discrete cluster structured alkali metal suboxides Rb_9O_2 and Cs_{11}O_3 [116, 117, 118, 119]. Photoemission studies on the NaBa_3N were recently carried out [129] but did not yield conclusive evidence for the lowering of the work function, mainly due to experimental difficulties.

Since, in contrast to other subnitrides, NaBa_3N can be prepared as stable high quality single crystals in appreciable size, it was challenging to search for magneto-quantum oscillations in this compound. In the present study [130] this most direct way of probing the electronic structure was chosen with the aim to elucidate the details of the FS of NaBa_3N and to obtain information about its electronic properties. Moreover, a quantitative comparison of the experimental data with those resulting from band structure calculations, carried out at the same time as the experiments, was envisaged.

5.1.2 Synthesis and Crystal Structure

The NaBa_3N crystal used for the experiment was produced by U. Steinbrenner at the Max-Planck-Institut für Festkörperforschung in Stuttgart following a previously described procedure [131]:

Crystals of NaBa_3N were prepared from elemental barium, nitrogen, and liquid Na-K alloy. Due to extremely high sensitivity of the materials to air and moisture, all preparations were carried out either in an argon-filled glove box or on a vacuum line (10^{-6} mbar to 10^{-5} mbar) using Schlenk-technique. Tantalum reaction containers were first cleaned using a 3:1 mixture of concentrated HNO_3 and HF, then heated in vacuum to 1000°C . Metallic barium (Merck, 99.0%) was purified by distilling it twice in vacuum from tantalum crucibles with heating to 1000°C in a closed tantalum container between the distillations in order to ensure absence of hydrogen. Nitrogen (Messer-Griesheim, 99.996%) was first dried by passing through blue-gel (silica gel with CoCl_2 as indicator) followed by molecular sieve (3 Å to 5 Å), then traces of oxygen were removed by passing the gas through BTS-catalyst (BASF) and Oxisorb-catalyst (Cr^{2+} on silica gel). Sodium (Merck, 99%) and potassium (Merck, 98%) were cleaned by cutting off the oxide layer, then melted together in the flow of argon and filtered through a glass frit.

In a first step, barium was reacted with a stoichiometric amount of nitrogen in a tantalum container by slowly heating to 400°C . After all nitrogen was absorbed, the reaction mixture was cooled to room temperature, transferred to another tantalum container, and sealed after adding Na-K alloy. The new mixture was heated at 320°C for three weeks and then slowly ($0.2^\circ\text{C}/\text{hour}$) cooled. A typical experiment involved about 5 g Ba, 1 g Na, 2 g K, and the appropriate amount of nitrogen

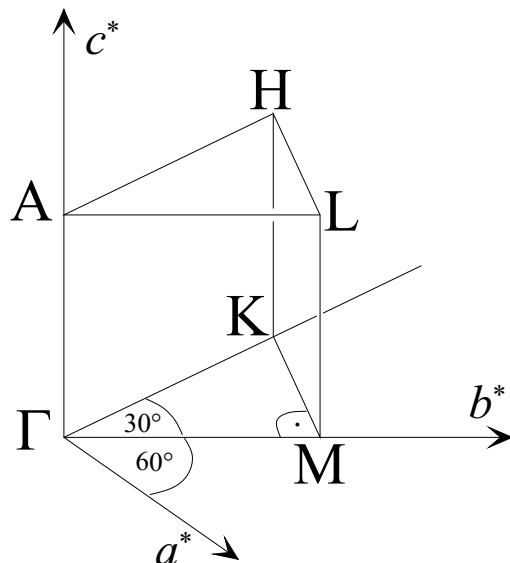


Figure 5.2: Irreducible wedge of the Brillouin zone indicating the symmetry points in \mathbf{k} -space: $\Gamma(0, 0, 0)$, $K(-1/3, 2/3, 0)$, $M(0, 1/2, 0)$, $A(0, 0, 1/2)$, $H(-1/3, 2/3, 1/2)$, and $L(0, 1/2, 1/2)$, where k_a , k_b , and k_c are given in parentheses as fractions of the reciprocal lattice parameters a^* , b^* , and c^* .

measured using a flask of a known volume with a manometer.

NaBa₃N single crystals in the form of rather large needles (up to 1 mm in diameter and up to 1 cm in length) could be obtained in this fashion. Two such crystals (0.3 mm to 0.5 mm in diameter, 2 mm to 3 mm in length) were selected for further studies and were sealed under argon in quartz glass capillaries. As already mentioned in chapter 3, due to the special preparation under protective inert-gas atmosphere only magnetic torque and no transport measurements were carried out. The orientations of the crystal symmetry axes were determined using precession photographs; these also confirmed the identity of the crystals. One crystal was used for two series of dHvA experiments within a 10 months time interval. No deterioration in the sample quality was found from one experiment to the other.

The title compound crystallizes hexagonally in the space group $P6_3/mmc$. The unit cell contains two NaBa₃N units and is determined by the lattice parameters $a = 8.4414(6)$ Å and $c = 6.9817(8)$ Å. The special symmetry points of the Brillouin zone in \mathbf{k} -space are sketched in Fig. 5.2.

5.1.3 Electronic Structure

Band structure, density of states, charge density, and Fermi surface calculations for NaBa₃N were carried out by G. V. Vajenine at the Max-Planck-Institut für Festkörperforschung in Stuttgart [130]. In order to provide the best possible basis for the understanding of the experimental results these calculations are presented and discussed in some detail in this section.

The computational procedure was based on the *Tight Binding Linear Muffin Tin*

Orbital method in the Atomic Sphere Approximation (TB-LMTO-ASA)². The program was allowed to insert rather large empty spheres (slightly over 5 atomic units in radius) in the rather open structure of the subnitride. A $24 \times 24 \times 24$ \mathbf{k} -point mesh (793 irreducible \mathbf{k} -points) was employed, the difference in results obtained with this mesh and with the $12 \times 12 \times 12$ mesh being negligible. A Scalar relativistic correction was found to be necessary in order to obtain realistic results. On the other side, turning on non-local exchange-correlation potentials was found to have little effect on the resulting band structure. The default setting (von Barth-Hedin local exchange-correlation potential) was employed to obtain all results presented below. Spin-polarized calculations were found, as expected for metallic NaBa₃N, to converge to the same results as non-spin-polarized calculations.

Since spin-orbit coupling plays a crucial role in determining the shape of the Fermi surface, the explicitly relativistic full-potential LMTO method³ was used to calculate the electronic structure of NaBa₃N as well. The band structures obtained with the two methods were found to be very similar around the Fermi level; the latter method also yielded the strength of the spin-orbit coupling in the ALH plane.

The results of the electronic structure calculations for NaBa₃N are in accordance with the above-mentioned simple formal electron distribution: Na⁺{[Ba²⁺]₃N³⁻}·4e⁻. That is, the 2s and 2p levels of the nitride anion are expected to be filled and to lie well below the Fermi level, followed by the partially filled conduction band comprised of sodium and barium states. The computed band structure, shown in Fig. 5.3(a) with the energy window chosen in the vicinity of the Fermi level, supports this viewpoint. Eight conduction electrons (there are two NaBa₃N formula units in the unit cell) fill the bands centered primarily on barium atoms and empty spheres, with small sodium contributions as well. The band shapes, especially around the bottom of the conduction band, are very similar to what one would expect from the simplest free-electron model [Fig. 5.3(b)]. The band structure around the Fermi level, however, is rather different from that expected based on the free-electron approximation: four bands crossing the Fermi level (bands 3, 4, 5, and 6 if counted from the bottom of the conduction band) are responsible for a very complex Fermi surface. Numerous electron- and hole-pockets result. An additional complication is due to the presence of the 6₃ screw axis. This leads to pairwise orbital degeneracy of bands 3-4 and 5-6 in the ALH plane. This degeneracy, however, is removed when weak spin-orbit coupling is taken into account. The arising small gaps open the possibility for the phenomenon of MB in high magnetic fields.

Owing to the similarity of the overall shape of the band structures shown in Figs. 5.3(a) and (b), especially around the bottom of the conduction band, the

²The Stuttgart TB-LMTO-ASA package, version 4.7 (<http://www.mpi-stuttgart.mpg.de/ANDERSEN/LMTODOC/LMTODOC.html>) [132].

³In this method the nonspherical terms of the density and the potential are represented as one-center spherical-harmonics expansions inside non-overlapping muffin-tin spheres and are expanded in plane waves in the interstitial region. The method is analogous to that developed by Weyrich [133] and Wills [134]. A brief description of the present implementation can be found in Ref. [135].

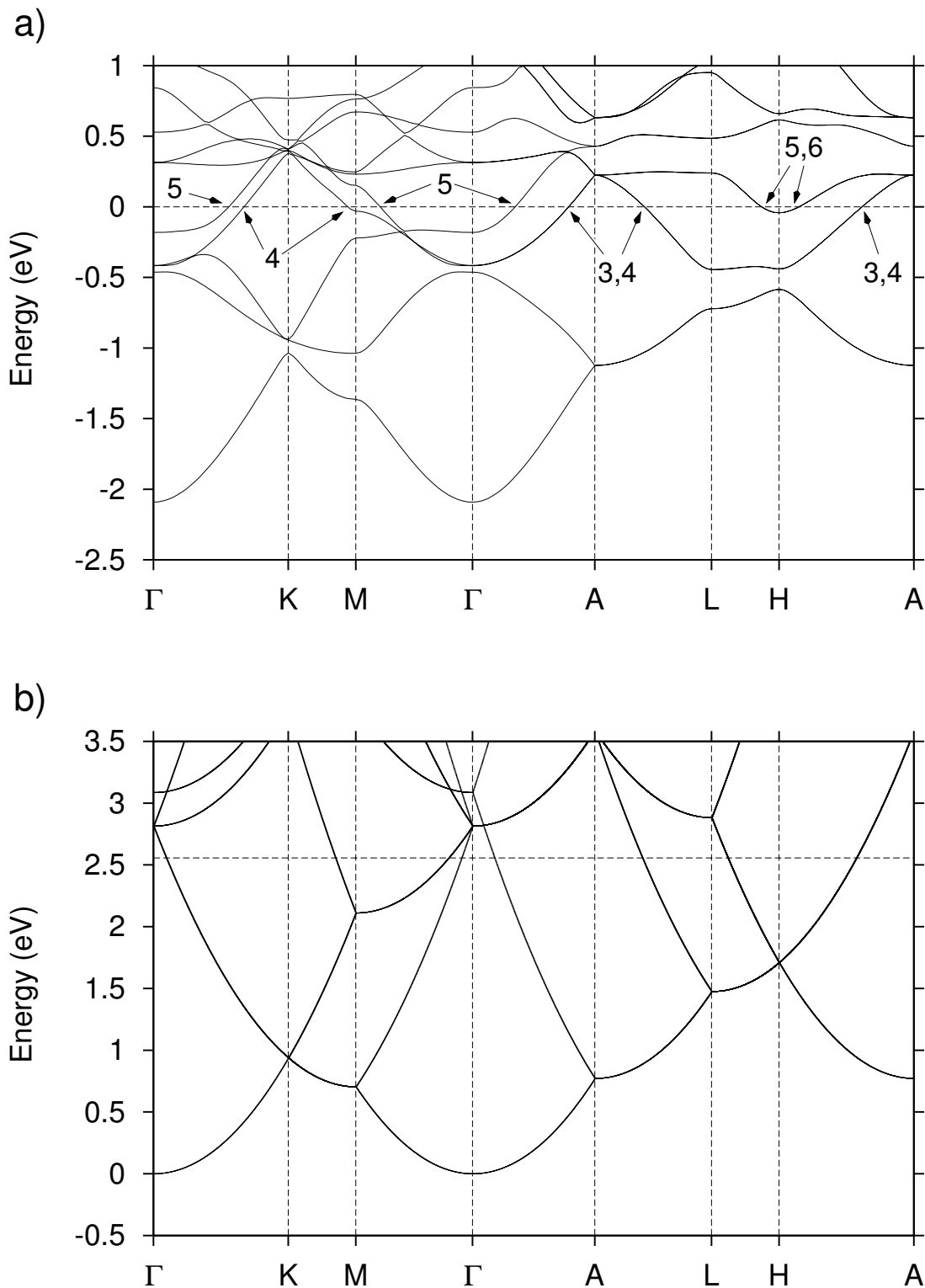


Figure 5.3: (a) Band structure of NaBa_3N computed using the TB-LMTO-ASA package. The bands are numbered from the bottom of the conduction band. The bands 3 to 6 cross the Fermi level which is set to 0 eV. (b) Energy dispersion for the model of a free-electron gas in the unit cell of NaBa_3N with the Fermi level corresponding to eight conduction electrons per unit cell. The energy at the bottom of the conduction band is set to 0 eV. [130]

free-electron model is regarded as a fair approximation of the system. Therefore, although the details of the band structure around the Fermi level are far beyond the reach of such a simple model, the overall NaBa₃N can be described as a nearly free-electron metal.

As outlined in the beginning of this chapter one of the main reasons for increased interest in the subnitrides and suboxides in general is the idea of treating these metallic compounds as *void metals* with repulsive centers (negatively charged oxide or nitride anions) periodically arranged in a nearly free-electron gas. As a consequence of such arrangement, mainly through the quantum size effect (exclusion of conduction electrons from the repulsive regions) the Fermi energy is raised (and the work function of the material is lowered, as was shown for the suboxides). The results of the calculations were analyzed with regard to the following features expected for a void metal: increased and nearly uniform electron density in the regions of space between the repulsive nitride anions, steeper bands due to the quantum size effect, and raising of the Fermi energy.

An analysis of the electron density originating from the conduction band confirms the first rather trivial feature: conduction electrons are indeed pushed away from the nitride centers and concentrate in the space between the Ba₃N chains with slight maxima between pairs of such chains. This charge density remains rather constant along the *c*-axis. This simple picture is somewhat complicated in two ways. Firstly, some conduction electron density is still located on the nitride anions due to mixing of the nitrogen 2s and 2p states in the conduction band. Secondly, the conduction electron density is strongly perturbed in the vicinity of the Na and Ba cores.

Reduction of the space available to the nearly free conduction electrons in NaBa₃N, effectively corresponding to a reduction in the lattice constant, could lead to steeper bands. The calculation of the curvature of the lowest conduction band around the Γ point reveals a curvature increase with respect to the value expected for free electrons by a factor of 1.7 perpendicular to the *c**-axis and by a factor of 2.0 along the *c**-axis. This, however, cannot be used as an argument in favor of the quantum-size effect in this case because a test calculation for metallic bcc barium at the same level of theory (TB-LMTO-ASA) yielded a similar increase (factor of 1.6) in the band curvature around Γ with respect to the free-electron value.

The computed Fermi energy for the NaBa₃N (the energy difference between the Fermi level and the bottom of the conduction band) is 2.09 eV. It is impossible to have an accurate comparison to an equivalent compound *without* the repulsive centers, so it may again be compared with metallic barium. For this metal the Fermi energy is calculated to 2.79 eV, that is clearly larger than for the void metal NaBa₃N. We have to remember though that there are only four conduction electrons per four metal atoms in NaBa₃N, while there are two conduction electrons per atom in elemental barium. Therefore, even if the bands in the NaBa₃N are steeper than those in barium, this should not necessarily lead to larger values of the Fermi energy.

5.2 Experimental Results and Discussion

The glass capillary containing the NaBa₃N crystal could be directly mounted onto the torquemeter as the quartz glass does not interact with a magnetic field. Detailed magnetic torque measurements were performed for different rotational angles around the a -, a' -, and c -axes,⁴ respectively, in angular steps of typically 4°. In the following notation, the orientation of the magnetic field is given by the angles θ and ϕ . θ denotes the angle between the magnetic field and the crystallographic c -axis and ϕ the angle between the magnetic field component in the (aa') -plane and the a -axis. The error in the angular resolution, that was dominated by the error made at the initial positioning of the crystal, could be limited to $\simeq 1^\circ$ by rescaling the results on the basis of symmetry considerations.

5.2.1 dHvA Oscillation Frequencies - Fermi Surface Topology

Pronounced oscillations in the magnetic torque were found at all magnetic field orientations with respect to the three main crystallographic axes of the sample. Fig. 5.4 illustrates the torque signal for a set of angles θ with the magnetic field perpendicular to the crystal a -axis. Since the oscillations are periodic in the inverse magnetic field scale, become stronger with lowering the temperature, and exhibit a temperature independent phase, they can be unambiguously attributed to the dHvA effect. At any magnetic field orientation a superposition of different oscillation frequencies was observed. In order to resolve the different dHvA oscillation frequencies the slowly varying background magnetization was subtracted and a Fourier transform of the field inverted curves was performed. Frequencies up to 3500 Tesla were detected. As a representative example, the frequency spectra of the curves displayed in Fig. 5.4(a) are shown in Fig. 5.5. The systematic study of the oscillation frequencies for every magnetic field orientation leads to a map of the angle dependent cross-sectional areas of the different parts of the FS. All the results are put together in Fig. 5.6 for rotations of the crystal around the a -, a' -, and c -axes, respectively. Those frequencies that can be clearly found in every plot are denoted by α , β , γ , δ , ε , ζ , η , and κ , in the order of increasing frequency: $F_\alpha(\phi = 120^\circ, \theta = 90^\circ) = 210 \pm 1$ Tesla, $F_\beta(\phi = 120^\circ, \theta = 0^\circ) = 491 \pm 2$ Tesla, $F_\gamma(\phi = 120^\circ, \theta = 0^\circ) = 750 \pm 6$ Tesla, $F_\delta(\phi = 120^\circ, \theta = 0^\circ) = 801 \pm 2$ Tesla, $F_\varepsilon(\phi = 120^\circ, \theta = 0^\circ) = 1152 \pm 5$ Tesla, $F_\zeta(\phi = 120^\circ, \theta = 0^\circ) = 1222 \pm 10$ Tesla, $F_\eta(\phi = 120^\circ, \theta = 0^\circ) = 1558 \pm 5$ Tesla, and $F_\kappa(\phi = 120^\circ, \theta = 90^\circ) = 2540 \pm 20$ Tesla. Of course, the chosen presentations of the plots may be regarded as tentative versions of the actual frequency paths. As could be expected from the hexagonal crystal structure, the $F(\theta)$ plots obtained for successive rotations around the a - and a' -axes are very similar to each other but both clearly differ from the $F(\phi)$ plot found for rotations around the c -axis.

⁴ a' is not shown in Fig. 1; it denotes the lattice direction in the (ab) -plane which lies at an angle of 30° to the a -axis, coinciding with the a^* direction in the reciprocal space.

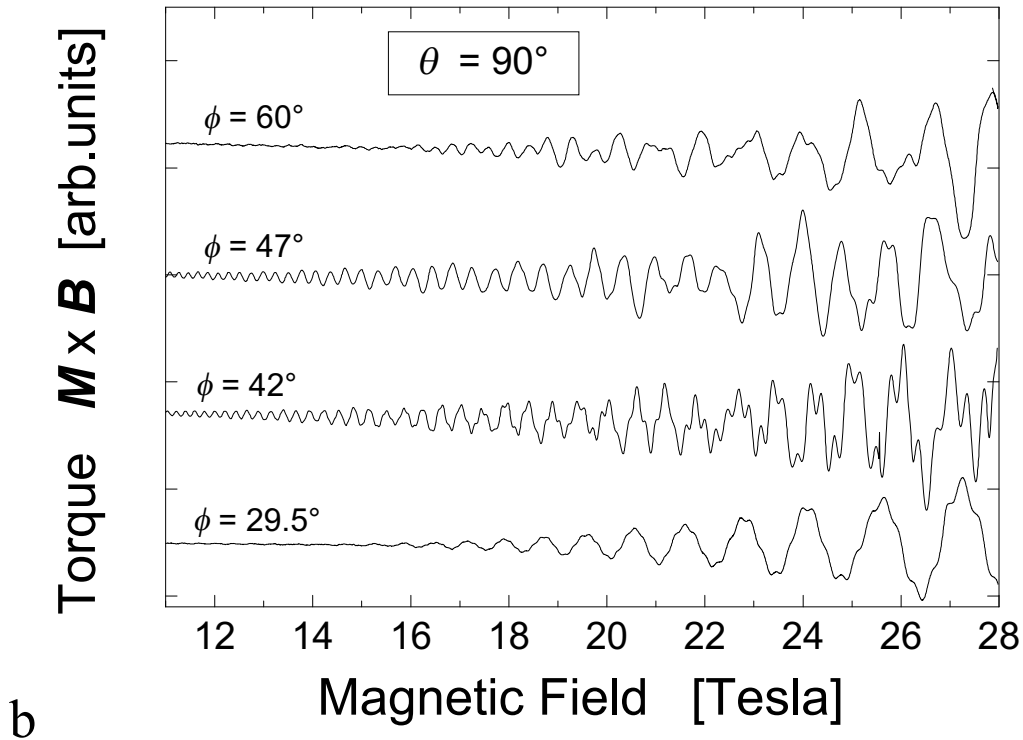
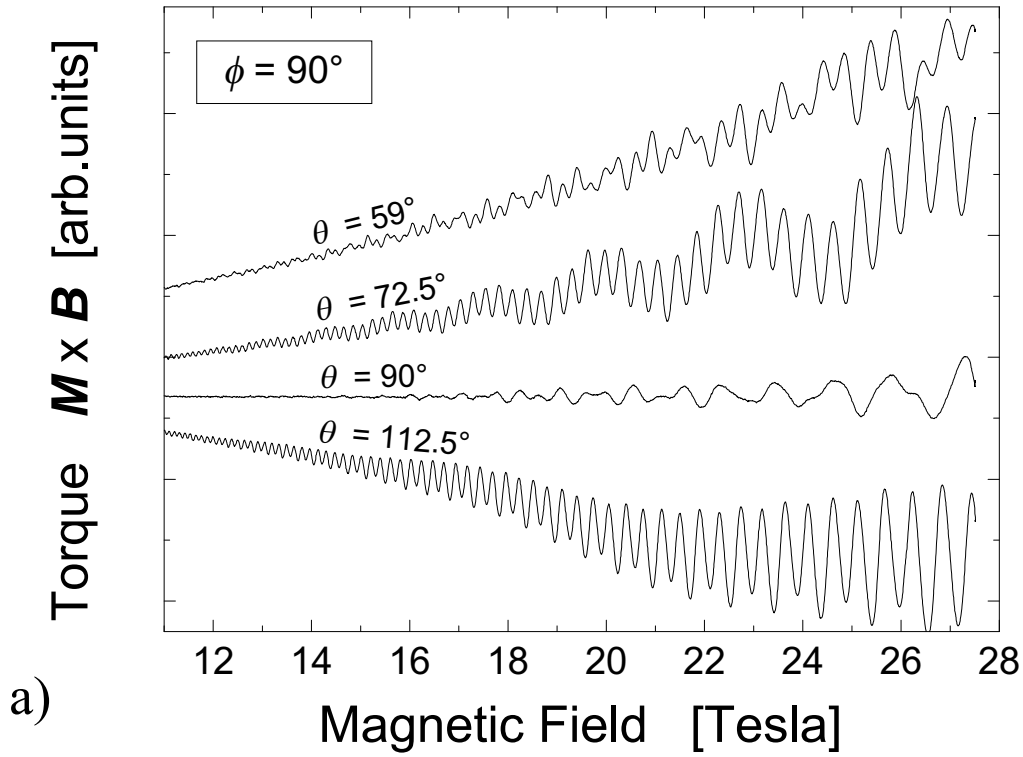


Figure 5.4: Examples for de Haas-van Alphen oscillations at several orientations of the magnetic field, with the field perpendicular to the (a) a -axis and (b) c -axis. For the curves of the latter graph, the steady background magnetization is subtracted. In both graphs, the curves are offset for clarity.

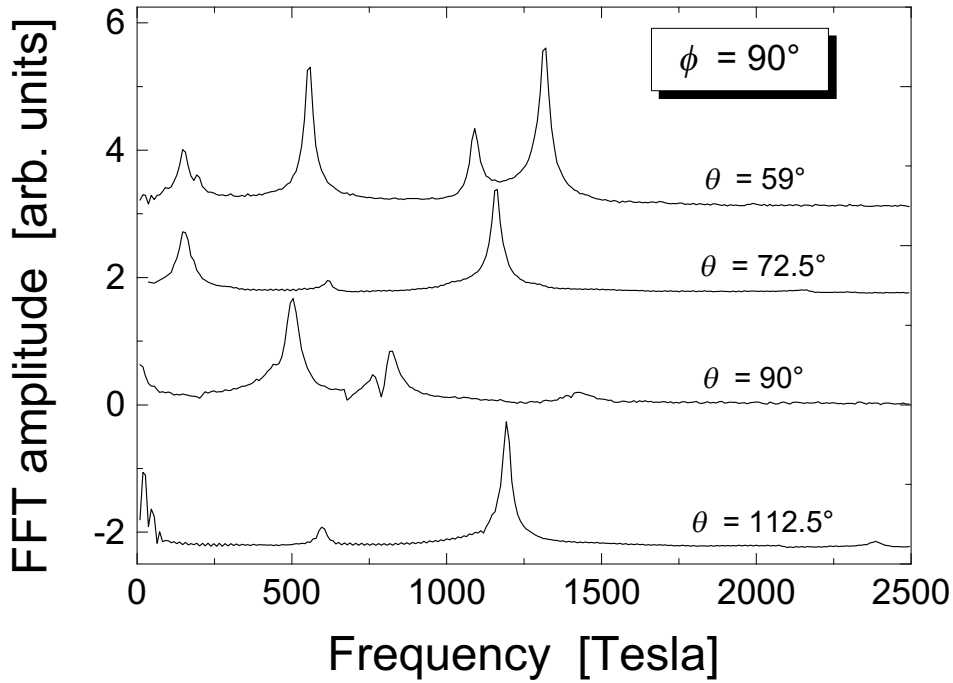
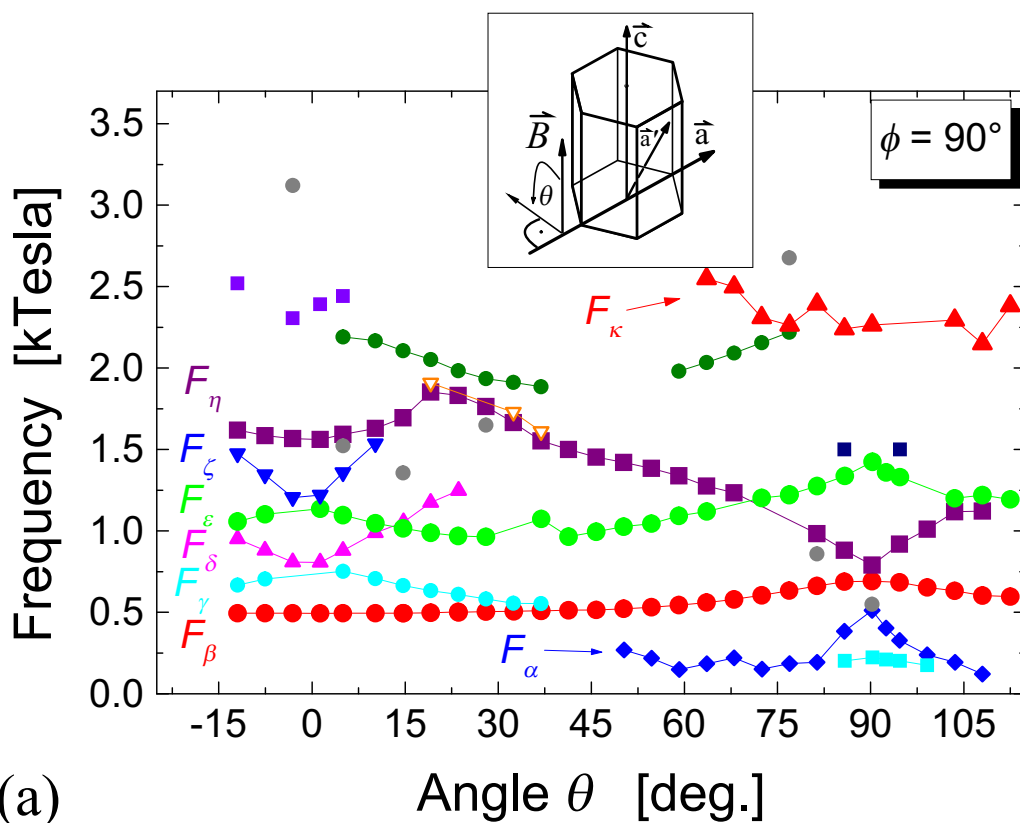


Figure 5.5: Fast Fourier transformations of the curves shown in Fig. 5.4(a). The curves are offset for clarity.

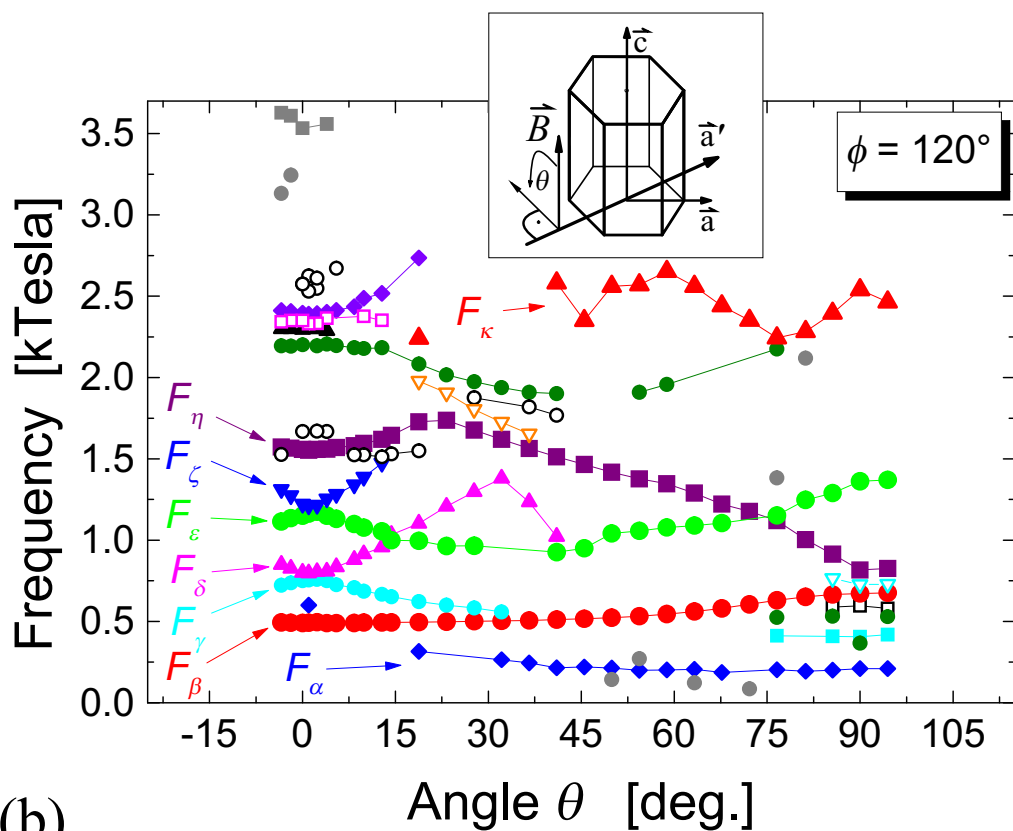
A comparison of the experimentally observed frequencies and their angular dependence does not reveal fully satisfying coincidence with the computed FS. However, some characteristic features can, at least qualitatively, be well described by the theoretical results. These are the two frequency crossings observed around $\theta = 0^\circ$ at ~ 1150 Tesla between F_ϵ and F_ζ and at ~ 750 Tesla between F_γ and F_δ [Fig. 5.6(a) and (b)]. They likely have their origin in the pockets centered in the ALH plane, i.e., the lens-shaped pockets of holes around A from bands 3 and 4 as well as lens-shaped pockets of electrons around H from bands 5 and 6 shown in Fig. 5.3. All other features of the computed Fermi surface could not as yet be assigned to observed oscillations, presumably due to insufficient accuracy of the computational method. Below, we concentrate on the above-mentioned hole-like A-pockets and electron-like H-pockets.

The A- and H-pockets themselves can be viewed as a result of folding-back of the Fermi surface due to the effective doubling of the basic electronic unit cell along the c -axis. This doubling takes place, however, not in the sense of translation but rather as a consequence of the 6_3 screw axis in the c -direction. Fig. 5.7 and Fig. 5.8(a) show how the folding-back of the Fermi surface leads to the pocket formation.

Due to the presence of spin-orbit coupling the resulting orbits in reciprocal space are influenced by the strength of the applied magnetic field. In the low field mode (no MB) the small spin-orbit interaction gap between the two bands in the ALH plane changes the topology of the Fermi surface so that a lens and



(a)



(b)

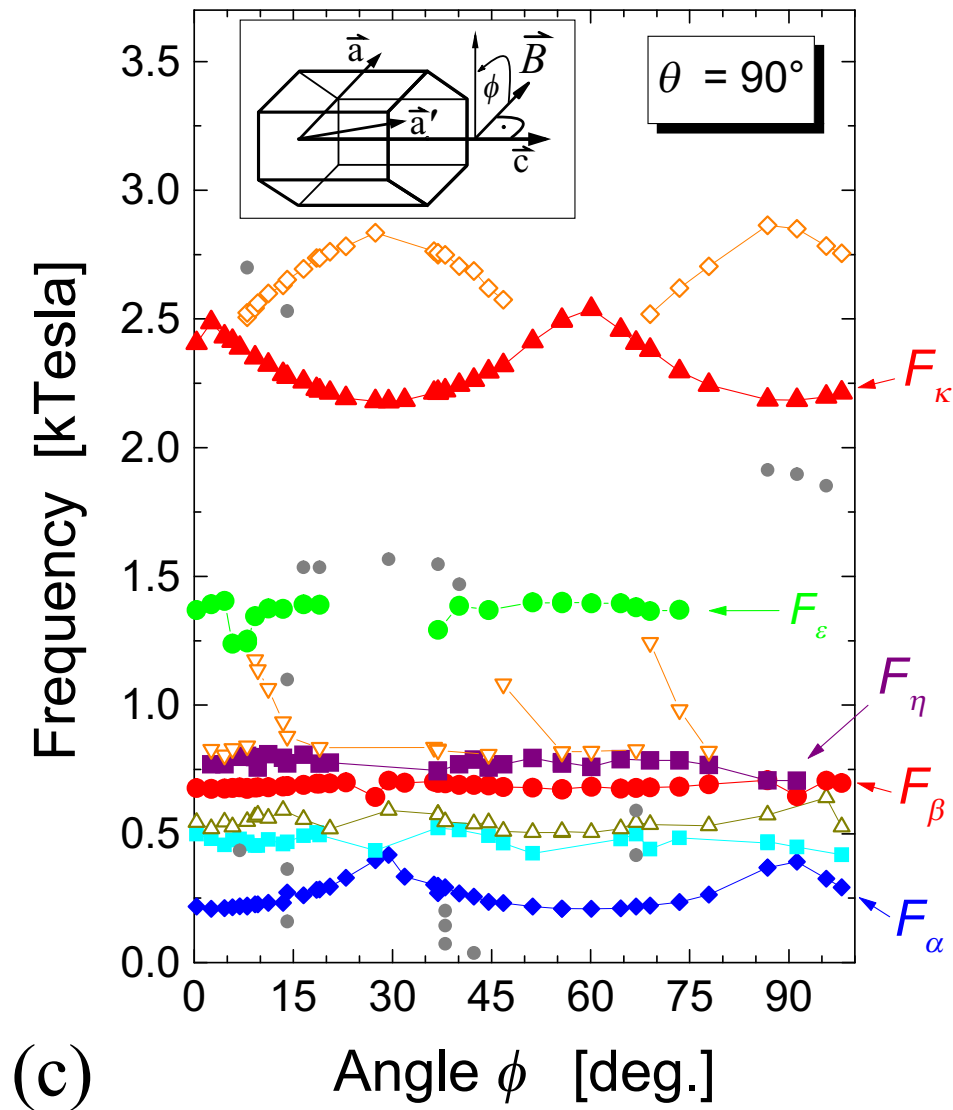


Figure 5.6: DHvA oscillation frequencies in dependence of the field orientation for rotations of the crystal around the crystal a -axis (a), a' -axis (b), and c -axis (c).

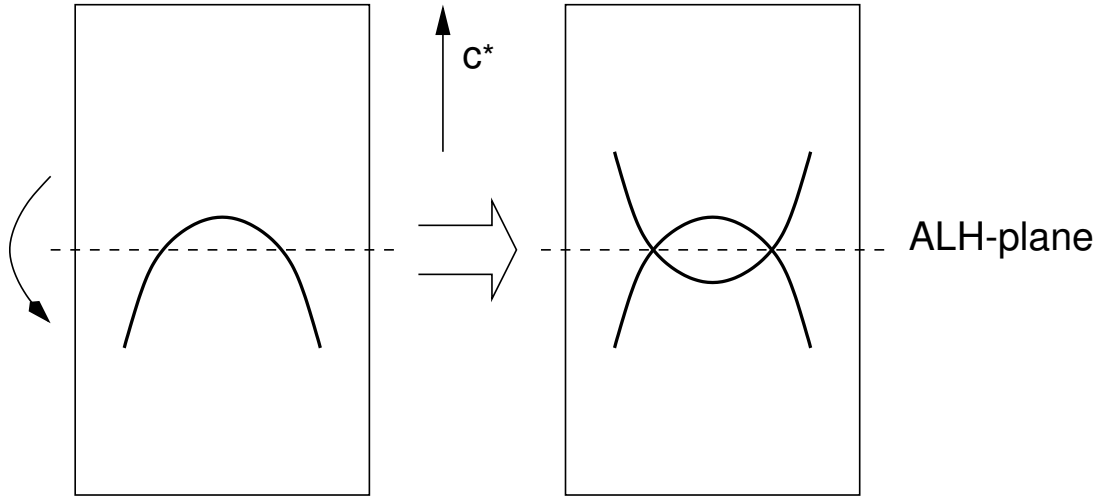


Figure 5.7: Schematic illustration of the formation of FS pockets around the A and H points due to back-folding of the FS caused by the presence of the 6_3 screw axis parallel to the c -axis.

a hyperbolic surface are formed [Fig. 5.8(b)]. When the magnetic field is parallel to the c -axis, two extremal cross-sections, one from the lens and one from the hyperboloid, lead to distinct dHvA oscillation frequencies. When the direction of the field rotates away from the c -axis, the area spanned by the extremal lens orbit becomes smaller while the extremal cross-sectional area of the hyperboloid is gradually enlarged. Thus, the lens frequency decreases and the hyperboloid frequency increases with increasing angle θ . This situation leads to an apparent crossing in the $F(\theta)$ plot as outlined in the right part of Fig 5.8(b).

The high-field mode (case of MB) is reached when the magnetic field is strong enough so that the orbits in the reciprocal space tunnel through the small gap in the ALH plane [Fig. 5.8(a)]. In this case the orbits on the FS would look as if the backfolding depicted in Fig. 5.7 did not take place. Therefore no extremal orbits would be expected in the vicinity of $\theta = 0^\circ$, with the exception of the case when θ is exactly zero: for this magnetic field orientation the k_c components of the orbits are absent and no high-curvature regions are encountered by an electron moving along these orbits. Hence, no effect of MB on these special orbits would be found. This precise orientation is though unlikely to be realized due to the above mentioned errors in the crystal orientation.

These conclusions are valid for both the A- and the H-pockets. The former have D_{6h} (6m) site symmetry, while the latter have lower D_{3h} (3m) site symmetry. Both types of pockets, however, deviate little from the ideal round shape suggested in Fig. 5.8.

A full-potential LMTO calculation was carried out in order to assess the magnitude of the spin-orbit interactions for the A- and H-pockets in the ALH plane. The size of the resulting gap was found to vary along both orbits, with average values of 0.005 eV for the A-pockets and 0.01 eV for the H-pockets. With regard

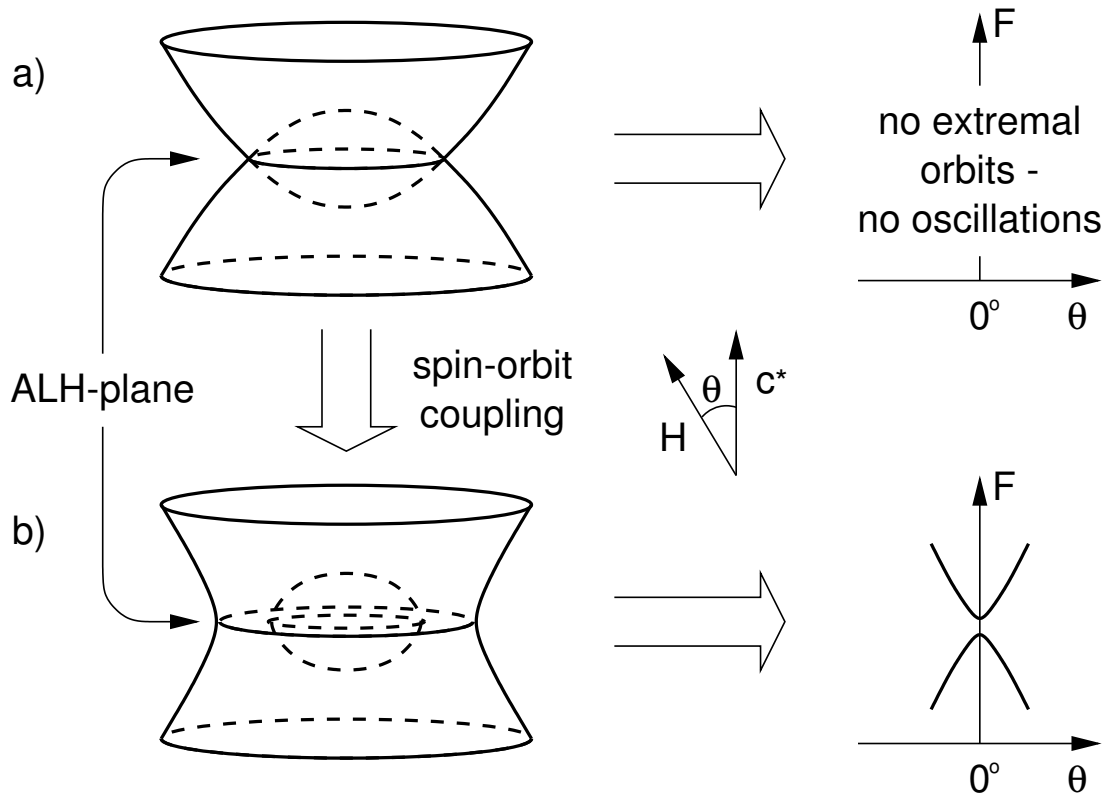


Figure 5.8: Schematic view of A- and H-pockets along with the $F(\theta)$ characteristics for the cases without (a) and including (b) spin-orbit coupling (the MB and no-MB modes, respectively).

to such small band separations compared to the Fermi energy and the cyclotron energies within the available field range one could expect the manifestation of MB.

However, frequency crossings, as sketched in Fig. 5.8(b), are observed in the $F(\theta)$ plots at the frequency pairs F_γ - F_δ (~ 750 Tesla) and F_ε - F_ζ (~ 1150) Tesla around $\theta = 0^\circ$ [Fig. 5.6(a) and (b)], that indicate well defined extremal orbits originating from clearly separated FS sheets of the lens shaped FS and the hyperboloid around H and A, respectively. Underestimated strength of the spin-orbit coupling in the full-potential LMTO calculations is seen to be the cause for this discrepancy between the theoretical predictions and the experimental results. We note that in order for the magnetic breakdown *not* to take place at 28 Tesla, the spin-orbit interaction must create a gap of at least ~ 0.05 eV.

From the computed band structure in the no-breakdown mode the frequencies of ~ 150 T and ~ 900 T are expected for the extremal orbits of the H- and A-pockets in the ALH plane, respectively. These values are markedly lower than found for the frequency pairs F_γ - F_δ and F_ε - F_ζ in the experiment. Owing to the identification of these orbits in the present study the experimental values may provide the main reference for further improvements of the computational procedure.

5.2.2 Effective Cyclotron Masses

The temperature dependence of the dHvA oscillation amplitudes fits to the behavior predicted by Lifshitz and Kosevich (2.9)/(2.11)). Fig. 5.9 shows the temperature dependence of the α and κ oscillation amplitudes as representative examples, fitted by the LK formula. The decrease of the amplitudes with increasing temperature turned out to be generally very weak. That indicates low effective cyclotron masses, m^* , of the charge carriers. In the average over all magnetic field orientations, the fits according to the LK formalism yield cyclotron masses associated with the orbits α , β , ε , η , and κ , $m_\alpha^* = 0.60 \pm 0.10 m_e$, $m_\beta^* = 0.51 \pm 0.10 m_e$, $m_\varepsilon^* = 0.64 \pm 0.10 m_e$, $m_\eta^* = 0.83 \pm 0.10 m_e$, and $m_\kappa^* = 1.04 \pm 0.10 m_e$, where m_e denotes the free electron mass. These rather low effective cyclotron mass values are indicative of steeper energy bands and stronger band curvature than in the free-electron case, as was discussed above with regard to the quantum size effect. A tendency of increasing mass values with oscillation frequency, $dm^*/dF \sim 0.25m_e/\text{kTesla}$, was noticed within the observed frequency range. Thus, the cyclotron masses are higher for carriers occupying large FS orbits. In the approximation of parabolic energy band dispersion the cyclotron mass is related to the quantum oscillation frequency as $m^* \propto \sqrt{F}$. This dependence describes the observed increase of the cyclotron mass with the oscillation frequency fairly well. However, from the present data we can not distinguish between a linear and square-root behavior of the cyclotron masses since both fits lie close to each other in the observed frequency range. The fact that the frequency dependence of the cyclotron mass does not contradict a $m^* \propto \sqrt{F}$ behavior suggests that the effective cyclotron mass values, including possible corrections due to many-body interactions, are isotropically distributed over the entire FS.

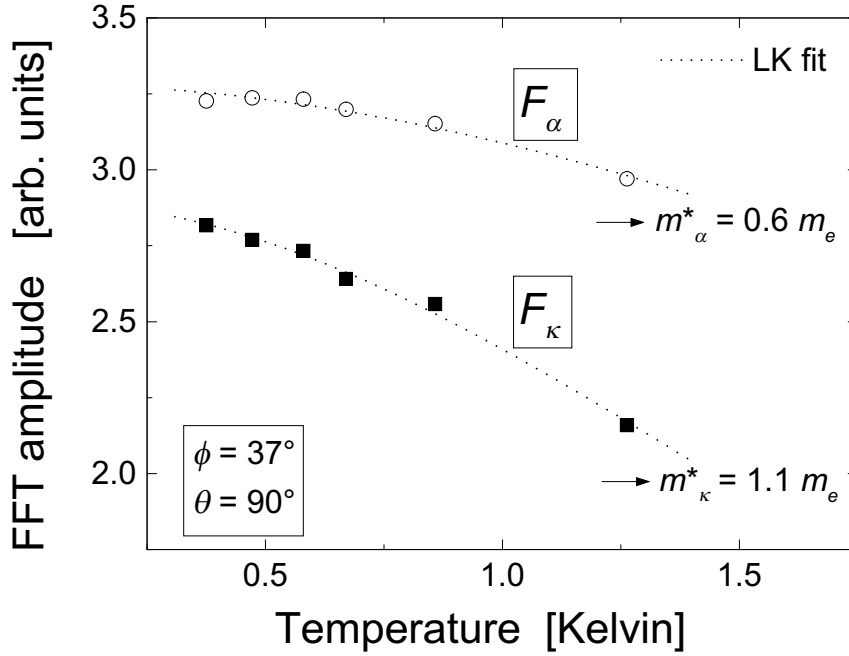


Figure 5.9: Temperature dependence of the oscillation amplitudes corresponding to the dHvA frequencies F_α and F_κ at the special orientation $\phi = 37^\circ$, $\theta = 90^\circ$. The fits according to the LK formula (2.9)/(2.11) are shown along with the resulting cyclotron mass values.

5.2.3 Dingle Temperature

With the experimental value for the carrier cyclotron mass of each orbit the Dingle temperatures could be extracted from the magnetic field dependence of the dHvA oscillation amplitude (2.9)/(2.13). For the determination of the different oscillation amplitudes FFT's were performed for 10 different inverse field intervals of equal size within the field range 10 T to 28 T. Two representative examples of Dingle plots are shown in Fig. 5.10 for the low-frequency α and the high-frequency κ oscillations. The linear behavior demonstrates that the observed field dependences are well described by the LK formalism. The values estimated for T_D associated with the orbits α to κ are in the range of 6.5 K down to 3.5 K with error bars of ± 1.5 K. Contrary to the cyclotron masses, the Dingle temperatures decrease with increasing oscillation frequency, $dT_D/dF \sim -1$ K/kTesla. According to Eq. (2.12) T_D is directly proportional to the inverse scattering time. With the values given above, we obtain scattering times of 2×10^{-13} s to 4×10^{-13} s. Especially in the present case of very low effective cyclotron masses, the Dingle temperature alone can be a misleading parameter since it is renormalized by the cyclotron energy. A more meaningful quantity is given by the carrier mean free path, l . Due to the present frequency dependence of the effective cyclotron mass values the carrier velocity at the Fermi energy decreases with the oscillation frequency, that compensates the frequency dependence of the scattering time and leads to a carrier mean free path, $l = 300 \pm 100$ nm, which is approximately constant within

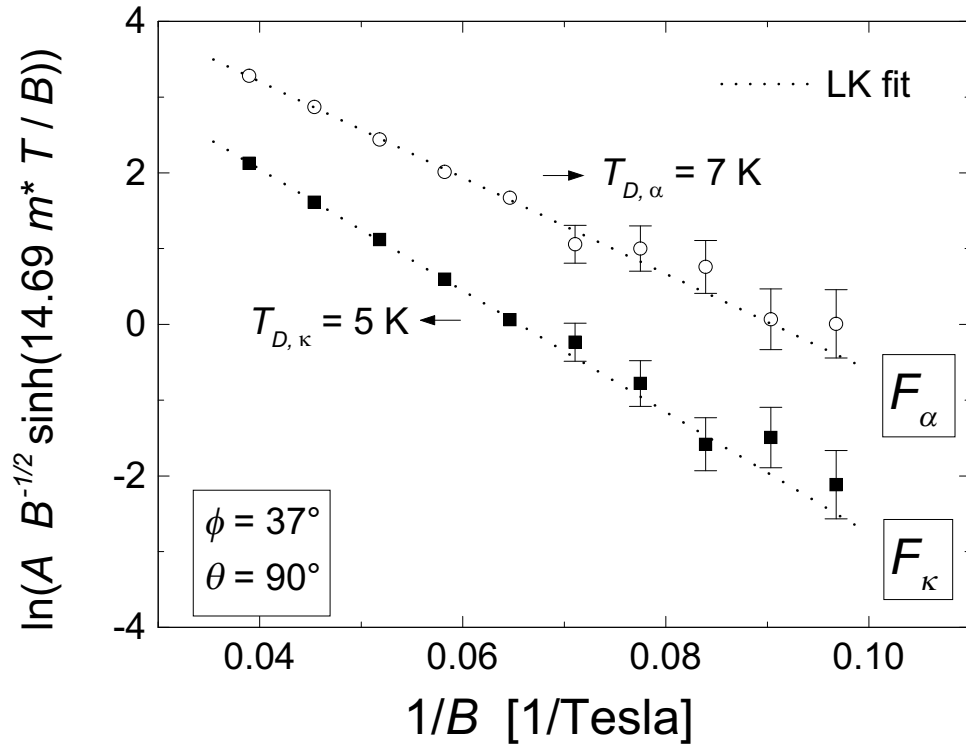


Figure 5.10: Dingle plots for the α and κ oscillations along with the fits according to the LK formula (2.9)/(2.13)

the whole frequency range. This mean free path is an order of magnitude higher than the length of the real space orbits and coincides well with those found in pure conventional metals.

If the real space trajectories of electrons were classical and circular, one could expect a dependence of l upon the crystal orientation with respect to the magnetic field: some orbits could remain unperturbed by the chains of repulsive nitride anions, while electrons on other orbits would be more likely to run into the repulsive centers and be scattered by those. However, no dependence of l upon the crystal orientation was noticed within the experimental error bar.

Chapter 6

Summary

The aim of the present work is the investigation of the electronic structures of two different solid systems by employing the versatile tool of magneto-quantum oscillations.

- The organic superconductor κ -(BEDT-TTF)₂Cu[N(CN)₂]Br consists of a layered structure which causes a highly two-dimensional character of electronic conduction. Making use of the de Haas-van Alphen (dHvA) as well as of the Shubnikov-de Haas (SdH) effect this compound was studied by means of the magnetic torque and four-probe magnetotransport techniques, respectively. This work reports on the first observation of quantum oscillations in κ -(BEDT-TTF)₂Cu[N(CN)₂]Br at ambient pressure, that opened the door for a detailed characterization of its electronic ground state. SdH measurements were carried out under various quasi-hydrostatic pressure up to 12 kbar and led to a comprehensive description of the pressure dependences of the electronic properties.
- The earth alkaline subnitride NaBa₃N is supposed to exhibit a void structure where hexagonally ordered quasi-one-dimensional chains of Ba₃N embedded in a metallic matrix are repulsive to conduction electrons and confine them to atomic scale regions between the chains. As a consequence, quantum size effects are expected to occur in this compound. DHvA oscillations could be detected in NaBa₃N by use of the torque method. They allowed to explore the electronic structure and properties of this system, as well as to compare the experimental results with very recent band structure calculations.

In accordance with theoretical predictions, the study on the organic superconductor κ -(BEDT-TTF)₂Cu[N(CN)₂]Br unveiled a Fermi surface characteristic of the quasi-two-dimensional κ -type BEDT-TTF compounds. The quantum oscillation frequency $F_\beta \simeq 3790$ T corresponds to the first Brillouin zone cross-sectional area and originates from the cross-sectional area of a nearly circular Fermi surface cylinder. The coupling of these cylinders along the k_a direction in the extended zone scheme gives rise to the small α orbit centered at the Brillouin zone boundary. With the oscillation frequency $F_\alpha \simeq 530$ T the α orbit is estimated to enclose about 14% of the first Brillouin zone cross-sectional area. The coexistence of the α and β frequencies suggests a small gap to open up at the points of intersection be-

tween adjacent Fermi surface cylinders at the Brillouin zone boundary and implies the β orbit to be governed by magnetic breakdown. Similar to the sister systems, the oscillation parameters yield strongly enhanced effective cyclotron mass values, $m_\alpha^* \simeq 3.1m_e$ and $m_\beta^* \simeq 6.6m_e$, indicating the presence of significant many-body interactions. Noticeably different to the results found in other κ -phase salts are the very weak oscillation amplitudes and a high Dingle temperature, $T_D \sim 2$ K, which indicates a markedly short mean free path. A clue for the understanding of these phenomena may lie in the particular sensitivity of the present system to the cooling procedure. A systematic thermal treatment revealed indeed a pronounced reduction of the oscillation amplitude upon driving the system from an annealed state to a probably more disordered state. The other oscillation parameters, however, did not show any strong changes. This might be explained by the existence of two spatially separated subphases, an ordered and a disordered one, where only the ordered phase contributes to the oscillations and supersedes the disordered fraction upon annealing. The observed features may be a result of the ground state of the κ -(BEDT-TTF)₂Cu[N(CN)₂]Br salt lying in closest vicinity to a metal-insulator transition and could indicate the presence of fluctuations associated with the insulating state. Further detailed studies are needed to uncover a probable relation between the oscillation amplitude, the mean free path, and thermal history.

Distinct beating behavior of the β oscillations attributed to a warped structure of the β orbit cylinder was found in the dHvA oscillations. The relative variation of the cross-sectional area along the cylinder axis is estimated to 0.71% that indicates a finite interlayer bandwidth of about $7 \cdot 10^{-3} \epsilon_{Fermi}$. Most strikingly, in separate SdH measurements as well as in simultaneous dHvA and SdH measurements, the beats are not analogously observed in the SdH oscillations. The SdH oscillation parameters hint to beats existing also in the SdH oscillations, with a beat phase shifted with respect to that of the dHvA oscillations. Such behavior represents a fundamental contradiction to the current understanding of magneto-quantum oscillations and indicates that the analogy of the SdH effect to the dHvA effect is not as straightforward as was hitherto usually assumed. This unexpected feature might arise from the highly two-dimensional electronic structure of the investigated system. The present observation should be an exciting starting point for the elaboration of a quantitative description of the SdH effect with special attention to the low-dimensional case.

Under high pressure, a marked change in the quantum oscillation frequency spectrum was observed. Instead of the α frequency found at ambient pressure two independent much lower frequencies, $F_{\alpha'} \approx 150$ T and $F_{2\alpha'} \approx 300$ T, appeared above 5 kbar. In order to understand this result, we propose to take into account a crystal lattice superstructure arising below 200 K in κ -(BEDT-TTF)₂Cu[N(CN)₂]Br as it was found in previous X-ray experiments. Introducing the new periodicity into the original Brillouin zone we obtain considerable topological changes of the initially proposed Fermi surface. If all involved interband gaps are taken into account, this model does not only explain the newly arising oscillation frequencies but also the evolution of the whole oscillation spectrum from

ambient pressure up to high pressure.

Beats very similar to those found in the dHvA oscillations were observed in the SdH oscillations under pressure. From the pressure dependence of the beat node position, possible values for the sensitivity of the interlayer bandwidth to pressure could be estimated.

The dHvA study on the metallic subnitride NaBa_3N unveiled a rich spectrum of oscillation frequencies. A systematic investigation of their dependence on the crystal orientation allowed to map the extremal cross-sectional areas of the whole Fermi surface. Two pairs of oscillation frequencies, F_γ - F_δ (~ 750 Tesla) and F_ε - F_ζ (~ 1150 Tesla), could be related to features of the predicted Fermi surface, namely to two types of nearly round lens-shaped pockets at H (electrons) and A (holes) points of the Brillouin zone. At these parts of the Fermi surface, weak splitting of energy levels in the ALH plane due to spin-orbit interactions was resolved. The oscillation parameters revealed very low effective cyclotron masses in the range of $0.5 m_e$ to $1.0 m_e$ increasing with the size of the associated \mathbf{k} -space orbits, as well as an isotropic carrier mean free path of about 300 nm. According to the band structure calculations, the charge density of conduction electrons is pushed away from the repulsive nitride anions. However, from the experimental data it was not possible to extract solid evidence for or against the occurrence of possible quantum size effects in NaBa_3N .

The theoretical methods employed for the currently available band structure predictions are at their accuracy limit (errors in band energy of as little as 0.05 eV could lead to a wrong Fermi surface topology); although the computed complex Fermi surface of NaBa_3N could be partially matched to the experimental data, in other respects the explanation of a part of the experimental results requires a refined theoretical treatment. The detailed characterization of the electronic properties accomplished in this work may serve as a reference for a further development of computational methods in order to understand the remaining details of the electronic structure of NaBa_3N and related materials.

Zusammenfassung

Das Ziel der vorliegenden Arbeit ist die Untersuchung der elektronischen Strukturen zweier unterschiedlicher Festkörpersysteme auf der Grundlage magnetischer Quantenoszillationen.

- Der organische Supraleiter κ -(BEDT-TTF)₂Cu[N(CN)₂]Br besteht aus einer Schichtstruktur, die zu einer hochgradig zweidimensionalen elektronischen Leitfähigkeit führt. Unter Ausnutzung des de Haas-van Alphen (dHvA) sowie des Shubnikov-de Haas (SdH) Effekts wurde diese Substanz mittels magnetischer Drehmoment beziehungsweise Vierpunkt-Magnetotransport Messungen untersucht. Im Rahmen dieser Arbeit konnten erstmals Quantenoszillationen in κ -(BEDT-TTF)₂Cu[N(CN)₂]Br bei Umgebungsdruck beobachtet werden, was eine ausführliche Charakterisierung des elektronischen Grundzustandes ermöglichte. SdH Messungen wurden unter verschiedenem quasi-hydrostatischem Druck bis zu 12 kbar durchgeführt, mit dem Ergebnis einer umfassenden Beschreibung der Druckabhängigkeiten der elektronischen Eigenschaften.

- Das Erdalkali Subnitrid NaBa₃N kann nach gegenwärtiger Vorstellung als „mikroskopisch geschäumtes Metall“ angesehen werden, in dem hexagonal angeordnete quasi-eindimensionale Ketten von ionisch gebundenem Ba₃N in eine metallische Matrix eingebettet sind und abstoßend auf Leitungselektronen wirken. Als Folge dieser Bindungsverhältnisse sollten die Aufenthaltsorte der Leitungselektronen auf die atomar schmalen Bereiche zwischen den Ketten eingeschränkt sein, was Quantisierungseffekte erwarten läßt. DHvA Oszillationen konnten mit Hilfe der Drehmoment Methode in NaBa₃N beobachtet werden. Dies erlaubte eine Untersuchung der elektronischen Strukturen und Eigenschaften des Systems sowie einen Vergleich der experimentellen Ergebnisse mit jüngsten Bandstrukturrechnungen.

In Übereinstimmung mit theoretischen Vorhersagen erbrachte die Untersuchung des organischen Supraleiters κ -(BEDT-TTF)₂Cu[N(CN)₂]Br eine Fermifläche die kennzeichnend für quasi-zwei-dimensionale BEDT-TTF Salze des κ -Typs ist. Die Quantenoszillationsfrequenz $F_\beta \simeq 3790$ T entspricht der Querschnittsfläche der ersten Brillouin-Zone und ist auf die Grundfläche eines näherungsweise kreisförmigen Fermiflächen Zylinders zurückzuführen. Die Kopplung dieser Zylinder entlang der k_a Richtung im ausgedehnten Zonenschema läßt den kleinen α -Orbit entstehen, dessen Zentrum an der Brillouin-Zonen Grenze liegt. Mit der Oszillationsfrequenz $F_\alpha \simeq 530$ T schließt der α -Orbit etwa 14% der Querschnittsfläche der ersten Brillouin-Zone ein. Das gleichzeitige Auftreten der α und β Frequenzen

weist auf eine kleine Lücke an den Kreuzungspunkten zwischen benachbarten Fermiflächen Zylindern an der Brillouin-Zonengrenze hin. Dies bedeutet, daß der β -Orbit erst durch magnetischen Zusammenbruch realisiert wird. Ähnlich wie in den verwandten Systemen, ergaben die Oszillationsparameter stark erhöhte Werte der effektiven Zyklotronmassen, $m_\alpha^* \simeq 3.1m_e$ und $m_\beta^* \simeq 6.6m_e$, die auf starke Vielteilchenwechselwirkungen hinweisen. In deutlichem Gegensatz zu den Ergebnissen, die in anderen Salzen der κ -Phase gefunden wurden, stehen sehr niedrige Oszillationsamplituden und eine hohe Dingle Temperatur, $T_D \sim 2$ K, die eine außergewöhnlich kurze mittlere freie Weglänge anzeigt. Ein Anhaltspunkt für das Verständnis dieser Phänomene ist möglicherweise in der hohen Empfindlichkeit des Systems auf das Abkühlverfahren gegeben. Systematische thermische Verfahrenszyklen ergaben tatsächlich eine deutliche Dämpfung der Oszillationsamplitude für den Fall, daß das System von einem *annealten* in einen vermutlich ungeordneteren Zustand übergeführt wurde. Alle anderen Oszillationsparameter zeigten jedoch keine auffallenden Änderungen. Dies könnte auf die Existenz zweier räumlich getrennter Subphasen, einer geordneten und einer ungeordneten, zurückzuführen sein, wobei nur die geordnete Phase einen Beitrag zu den Oszillationen leistet und den Anteil der ungeordneten Phase beim *annealing* Prozeß verdrängt. Das beobachtete Verhalten kann möglicherweise als Folge dafür gesehen werden, daß der Grundzustand des κ -(BEDT-TTF)₂Cu[N(CN)₂]Br Salzes sehr nahe an einem Metall-Isolator Übergang liegt und die Anwesenheit von Fluktuationen anzeigen, die mit dem isolierenden Zustand verbunden sind. Weitere umfangreiche Experimente sind notwendig, um die genauen Zusammenhänge zwischen der Oszillationsamplitude, der mittleren freien Weglänge und der thermischen Vorbehandlung aufzuklären.

Klar erkennbare Schwebungen in den β Oszillationen, die einer gewellten Struktur des β Orbit Zylinders zugeschrieben werden können, wurden in den dHvA Oszillationen beobachtet. Die relative Variation der Querschnittsfläche entlang der Zylinderachse konnte daraus zu 0.71% abgeschätzt werden, was einer endlichen Energiebandbreite in der Richtung senkrecht zu den hochleitfähigen Schichten von $7 \cdot 10^{-3} \epsilon_{Fermi}$ entspricht. Überraschenderweise wurden in separaten SdH Messungen sowie in simultanen dHvA und SdH Messungen die Schwebungen nicht in analoger Weise in den SdH Oszillationen beobachtet. Die SdH Oszillationsparameter deuten darauf hin, daß in den SdH Oszillationen ebenfalls Schwebungen auftreten, diese jedoch eine Phase aufweisen, die in Bezug auf die der dHvA Oszillationen verschoben ist. Ein derartiges Verhalten steht in grundlegendem Widerspruch zum gegenwärtigen Verständnis von Magneto-Quantenoszillationen und zeigt, daß die Analogie zwischen SdH und dHvA Effekt nicht so einfach und direkt ist, wie bisher angenommen. Es ist denkbar, daß dieses unerwartete Resultat mit der hoch zweidimensionalen Elektronstruktur des untersuchten Systems in Zusammenhang steht. Auf jeden Fall sollte diese Beobachtung ein interessanter Anstoß zur Erarbeitung einer quantitativen Beschreibung des SdH Effekts unter besonderer Beachtung der niedrigen Dimensionalität sein.

Unter hohem Druck wurde eine markante Änderung im Frequenzspektrum der Quantenoszillationen beobachtet. Anstelle der α Frequenz, die bei Umgebungs-

druck beobachtet wurde, traten oberhalb eines Druckes von 5 kbar zwei unabhängige, deutlich niedrigere Frequenzen, $F_{\alpha'} \approx 150$ T und $F_{2\alpha'} \approx 300$ T, auf. Um dieses Ergebnis zu verstehen, wird eine Überstruktur des Kristallgitters in Betracht gezogen, die, wie aus früheren Röntgenstrukturanalysen hervorgeht, unterhalb 200 K in κ -(BEDT-TTF)₂Cu[N(CN)₂]Br auftritt. Führt man die neue Periodizität in die ursprüngliche Brillouin-Zone ein, so ergeben sich massive Änderungen der ursprünglich vorgeschlagenen Fermiflächentopologie. Bei Berücksichtigung aller beteiligten Interbandlücken erklärt dieses Modell nicht nur das Auftreten neuer Oszillationsfrequenzen sondern auch die Entwicklung des Oszillationsspektrums von Umgebungsdruck bis zu hohem Druck.

In den SdH β Oszillationen wurden unter Druck Schwebungen beobachtet, die eine hohe Ähnlichkeit mit den unter Umgebungsdruck in den dHvA Oszillationen gefundenen Schwebungen aufweisen. Aus der Druckabhängigkeit der Position des Schwebungsknotens konnten mögliche Werte der Druckempfindlichkeit der Energiebandbreite in der Richtung senkrecht zu den hochleitfähigen Schichten abgeschätzt werden.

Die dHvA Experimente am Metallsubnitrid NaBa₃N brachten ein reichhaltiges Spektrum von Oszillationsfrequenzen in dieser Substanz zutage. Eine systematische Untersuchung ihrer Abhängigkeit von der Kristallorientierung erlaubte die Ausmessung der extremalen Querschnittsflächen der gesamte Fermifläche. Zwei Paare von Oszillationsfrequenzen, $F_{\gamma}-F_{\delta}$ (~ 750 Tesla) und $F_{\epsilon}-F_{\zeta}$ (~ 1150 Tesla), konnten Merkmalen der vorhergesagten Fermifläche zugeordnet werden. Dies sind zwei näherungsweise linsenförmige Ellipsoidtaschen an den Punkten H (Elektronen) und A (Löcher) der Brillouin-Zone. An diesen Teilen der Fermifläche wurde eine schwache Aufspaltung der Energieniveaus in der ALH Ebene aufgrund von Spin-Bahn Wechselwirkungen nachgewiesen. Die Oszillationsparameter ergaben sehr niedrige effektive Zyklotronmassen im Bereich von $0.5 m_e$ bis $1.0 m_e$, die mit der Größe der jeweiligen Orbits im \mathbf{k} -Raum zunehmen, sowie eine isotrope mittlere freie Weglänge von etwa 300 nm. Den Bandstruktur Rechnungen zufolge wird die Leitungselektronendichte von den Orten der ionisch gebundenen Nitrid Anionen verdrängt. Auf der Grundlage der gewonnenen experimentellen Daten war es jedoch nicht möglich, einen verlässlichen Beweis für oder gegen das Auftreten möglicher Quantisierungseffekte in NaBa₃N zu liefern.

Die theoretischen Methoden, die für die bis dato ausgeführten Bandstrukturrechnungen eingesetzt wurden, sind an ihrer Genauigkeitsgrenze angelangt (bereits Fehler in der Bandenergie von 0.05 eV können eine falsche Fermiflächentopologie ergeben); auch wenn die Resultate der Berechnung der sehr umfangreichen Fermifläche von NaBa₃N teilweise eine gute Übereinstimmung mit den experimentellen Daten liefern, so erfordert die Erklärung eines Teiles der experimentellen Ergebnisse in anderer Hinsicht doch eine verfeinerte theoretische Behandlung. Die im Rahmen dieser Arbeit durchgeführte detaillierte Charakterisierung der elektronischen Eigenschaften von NaBa₃N möge als Anhaltspunkt für eine Weiterentwicklung der Rechenmethoden dienen, um die noch unklaren Details der elektronischen Struktur von NaBa₃N und verwandter Substanzen aufzuklären.

Bibliography

- [1] L. W. Schubnikow and W. J. de Haas *Proc. Netherlands Roy. Acad. Sci.*, vol. **33**, p. 130 and 163, 1930.
- [2] W. J. de Haas and P. M. van Alphen *Proc. Netherlands Roy. Acad. Sci.*, vol. **33**, p. 1106, 1930.
- [3] L. D. Landau *Z. Phys.*, vol. **64**, p. 629, 1930.
- [4] I. M. Lifshitz unpublished lecture, 1950.
- [5] L. Onsager *Phil. Mag.*, vol. **43**, p. 1006, 1952.
- [6] I. M. Lifshitz and A. M. Kosevich *Sov. JETP*, vol. **2**, p. 636, 1956.
- [7] D. Shoenberg *PM*, p. 62, 1969.
- [8] A. V. Gold, *Electrons in Metals*, vol. **1** of *Solid State Physics*, p. 39. New York: Gordon and Breach, 1968.
- [9] D. Shoenberg, *Magnetic Oscillations in Metals*. Cambridge University Press, 1984.
- [10] E. N. Adams and T. D. Holstein *J. Phys. Chem. Sol.*, vol. **10**, p. 254, 1959.
- [11] D. Shoenberg *Proc. Roy. Soc.*, vol. **A170**, p. 341, 1939.
- [12] J. M. Luttinger *Phys. Rev.*, vol. **121**, p. 1251, 1961.
- [13] R. B. Dingle *Proc. Roy. Soc. London Ser.*, vol. **A 211**, p. 517, 1952.
- [14] A. Wasserman and M. Springford *Adv. Phys.*, vol. **45**, p. 471, 1996.
- [15] M. Springford, *Electrons at the Fermi surface*. Cambridge University Press, 1980.
- [16] E. I. Blount *Phys. Rev. Lett.*, vol. **126**, p. 1636, 1962.
- [17] A. B. Pippard *Proc. Roy Soc. A*, vol. **270**, p. 1, 1962.
- [18] A. B. Pippard *Phil. Trans. Roy. Soc. A*, vol. **265**, p. 317, 1964.
- [19] L. M. Falicov and H. Stachowiak *Phys. Rev.*, vol. **147**, p. 505, 1966.

- [20] A. B. Pippard, *The Dynamics of Conduction Electrons*. Glasgow: Blackie and Son, 1965.
- [21] I. D. Vagner, T. Maniv, and E. Ehrenfreud *Phys. Rev. Lett.*, vol. **51**, p. 1700, 1983.
- [22] I. D. Vagner and T. Maniv *Phys. Rev. B*, vol. **32**, p. 8398, 1985.
- [23] K. Jauregui, V. I. Marchenko, and I. D. Vagner *Phys. Rev. B*, vol. **41**, p. 12 922, 1990.
- [24] M. A. Itskovsky, T. Maniv, and I. D. Vagner *Z. Phys. B: Condens. Matter*, vol. **101**, p. 13, 1996.
- [25] M. A. Itskovsky, T. Maniv, and I. D. Vagner *Phys. Rev. B*, vol. **61**, p. 14 616, 2000.
- [26] N. Harrison, R. Bogaerts, P. Reinders, J. Singleton, S. J. Blundell, and F. Herlach *Phys. Rev. B*, vol. **54**, p. 9977, 1996.
- [27] P. D. Grigoriev and I. D. Vagner *JETP Lett.*, vol. **69**, p. 139, 1999.
- [28] F. Bitter *Rev. Sci. Instr.*, p. 486, 1936.
- [29] R. Boissier, F. Brichant, J. Goyer, J. Fournier, R. Ricque, J. L. Féron, R. Pauthenet, and J. C. Picoche, "Les Champs Magnétiques Intenses - leur production et leurs applications," Colloques Internationaux du CNRS **166**, (Editions du CNRS, 1967), p. 83, Grenoble, 12-14 Sept. 1966.
- [30] M. Wood, *High Magnetic Fields*. Cambridge: MIT Press, Mass. 1996.
- [31] M. Wood and B. Montymery, *Combined Superconducting and Conventional Magnets*. Les Champs Magnétiques Intenses. Series **B**, Plenum, 1996.
- [32] P. Christ *Diplomarbeit, Technische Universität München, München*, 1993.
- [33] P. Christ, W. Biberacher, H. Müller, and K. Andres *Solid State Commun.*, vol. **91**, p. 451, 1994.
- [34] M. V. Kartsovnik, G. Y. Logvenov, H. Ito, T. Ishiguro, and G. Saito *Phys. Rev. B*, vol. **52**, p. R15 715, 1995.
- [35] J. D. Thompson *Rev. Sci. Instrum.*, vol. **55**, p. 231, 1984.
- [36] W. A. Little *Phys. Rev.*, vol. **134A**, p. 1416, 1964.
- [37] H. W. Kroto, J. R. Heath, S. C. O'Brien, and R. F. Curl *Nature*, vol. **318**, p. 165, 1985.
- [38] S. Iijima *Nature*, vol. **354**, p. 56, 1991.

- [39] R. E. Peierls, *Quantum Theory of Solids*. Oxford: Clarendon Press, 1953.
- [40] T. Ishiguro, K. Yamaji, and G. Saito, *Organic Superconductors*. Berlin, Heidelberg: Springer-Verlag, 2nd ed., 1998.
- [41] H. Urayama, H. Yamochi, G. Saito, K. Nozawa, T. Sugano, M. Kinoshita, S. Saito, K. Oshima, A. Kawamoto, and J. Tanaka *Chem. Lett.*, vol. **1988**, p. 55, 1988.
- [42] A. M. Kini, U. Geiser, H. H. Wang, K. D. Carlson, J. M. Williams, W. K. Kwok, K. G. Vandervoort, J. E. Thompson, D. L. Stupka, D. Jung, and M.-H. Whangbo *Inorg. Chem.*, vol. **29**, p. 2555, 1990.
- [43] J. M. Williams, A. M. Kini, H. H. Wang, K. D. Carlson, U. Geiser, L. K. Montgomery, G. J. Pyrka, D. M. Watkins, J. M. Kommers, S. J. Boryschuk, A. V. S. Crouch, W. K. Kwok, J. E. Schirber, D. L. Overmyer, D. Jung, and M.-H. Whangbo *Inorg. Chem.*, vol. **29**, p. 3272, 1990.
- [44] K. Kanoda *Hyperfine Interact.*, vol. **104**, p. 235, 1997.
- [45] H. Mayaffre, P. Wzietek, S. Charfi-Kaddour, C. Lenoir, D. Jerome, and P. Batail *Physica B*, vol. **206-207**, p. 767, 1995.
- [46] K. Miyagawa, A. Kawamoto, Y. Nakazawa, and K. Kanoda *Phys. Rev. Lett.*, vol. **75**, p. 1174, 1995.
- [47] K. Oshima, T. Mori, H. Inokuchi, H. Urayama, H. Yamochi, and G. Saito *Phys. Rev. B*, vol. **38**, p. 938, 1988.
- [48] C.-P. Heidmann, H. Müller, W. Biberacher, K. Neumaier, C. Probst, K. Andres, A. G. M. Jansen, and W. Joss *Synth. Met.*, vol. **41-43**, p. 2029, 1991.
- [49] M. V. Kartsovnik, W. Biberacher, K. Andres, and N. D. Kushch *JETP Lett.*, vol. **62**, p. 905, 1995.
- [50] Y. C. Jean, Y. Lou, H. L. Yen, K. M. O'Brien, R. N. West, H. H. Wang, K. D. Carlson, and J. M. Williams *Physica C*, vol. **221**, p. 399, 1994.
- [51] U. Geiser, A. M. Kini, H. H. Wang, M. A. Beno, and J. M. Williams *Acta Cryst. C*, vol. **47**, p. 190, 1991.
- [52] U. Geiser, A. J. Schultz, H. H. Wang, D. M. Watkins, D. L. Stupka, J. M. Williams, J. E. Schirber, D. L. Overmyer, D. Jung, J. J. Novoa, and M.-H. Whangbo *Physica C*, vol. **174**, p. 475, 1991.
- [53] W. Y. Ching, Y.-N. Xu, Y. C. Jean, and Y. Lou *Phys. Rev. B*, vol. **55**, p. 2780, 1997.
- [54] A. J. Schultz, M. A. Beno, U. Geiser, H. H. Wang, A. M. Kini, J. M. Williams, and M.-H. Whangbo *J. Solid State Chem.*, vol. **94**, p. 352, 1991.

- [55] Y. Nogami, J. P. Pouget, H. Ito, T. Ishiguro, and G. Saito *Solid State Commun.*, vol. **89**, p. 113, 1994.
- [56] P. Wzietek, H. Mayaffre, D. Jérôme, and S. Brazovskii *J. Phys. I France*, vol. **6**, p. 2011, 1996.
- [57] M. Kund, H. Müller, W. Biberacher, K. Andres, and G. Saito *Physica B*, vol. **191**, p. 274, 1993.
- [58] Y. Watanabe, H. Sato, T. Sasaki, and N. Toyota *J. Phys. Soc. Jpn.*, vol. **60**, p. 3608, 1991.
- [59] G. Saito, H. Yamochi, T. Nakamura, T. Komatsu, T. Ishiguro, Y. Nogami, Y. Ito, H. Mori, K. Oshima, M. Nakashima, S. Uchida, H. Takagi, S. Kagoshima, and T. Osada *Synth. Met.*, vol. **41-43**, p. 1993, 1991.
- [60] M. A. Tanatar, T. Ishiguro, T. Kondo, and G. Saito *Phys. Rev. B*, vol. **59**, p. 3841, 1999.
- [61] S. Ravy, R. Moret, and J. P. Pouget *Phys. Rev. B*, vol. **38**, p. 4469, 1988.
- [62] T. Mori, A. Kobayashi, Y. Sasaki, H. Kobayashi, G. Saito, and H. Inokuchi *Chem. Lett.*, vol. **1984**, p. 957, 1984.
- [63] M.-H. Whangbo, J. M. Williams, P. C. W. Leung, M. A. Beno, T. J. Emge, H. H. Wang, K. D. Carlson, and G. W. Crabtree *J. Am. Chem. Soc.*, vol. **107**, p. 5815, 1985.
- [64] M.-H. Whangbo, J. M. Williams, A. J. Schultz, T. J. Emge, and M. A. Beno *J. Am. Chem. Soc.*, vol. **109**, p. 90, 1987.
- [65] A. J. Schultz, H. H. Wang, J. M. Williams, L. W. Finger, R. M. Hazen, C. Rovira, and M.-H. Whangbo *Physica C*, vol. **234**, p. 300, 1994.
- [66] J. Wosnitza, *Fermi Surface of Low-Dimensional Organic Metals and Superconductors*. Springer-Verlag, 1996.
- [67] Y. Yamauchi, M. V. Kartsovnik, T. Ishiguro, M. Kubota, and G. Saito *J. Phys. Soc. Jpn.*, vol. **65**, p. 354, 1996.
- [68] M. V. Kartsovnik, G. Y. Logvenov, W. Biberacher, T. Ishiguro, P. Christ, K. Andres, E. Steep, A. G. M. Jansen, N. D. Kushch, and H. Müller *Synth. Met.*, vol. **86**, p. 2061, 1997.
- [69] J. Caulfield, W. Lubczynski, F. L. Pratt, J. Singleton, D. Y. K. Ko, W. Hayes, M. Kurmoo, and P. Day *J. Phys.: Condens. Matter*, vol. **6**, p. 2911, 1994.
- [70] H. Weiss, M. V. Kartsovnik, W. Biberacher, E. Balthes, A. G. M. Jansen, and N. D. Kushch *Phys. Rev. B*, vol. **60**, p. R16 259, 1999.

- [71] H. Weiss, M. V. Kartsovnik, W. Biberacher, E. Steep, A. G. M. Jansen, and N. D. Kushch *JETP Lett.*, vol. **66**, p. 190, 1997.
- [72] C. H. Mielke, N. Harrison, D. G. Rickel, A. H. Lacerda, R. M. Vestal, and L. K. Montgomery *Phys. Rev. B*, vol. **56**, p. 4309, 1997.
- [73] T. Sasaki, H. Sato, and N. Toyota *Solid State Commun.*, vol. **76**, p. 507, 1990.
- [74] R. P. Shibaeva *et al.* Institute for Chemical Physics Research, Chernogolovka. private communication.
- [75] K. Yamaji *J. Phys. Soc. Jpn.*, vol. **58**, p. 1520, 1989.
- [76] T. Komatsu, N. Matsukawa, T. Inoue, and G. Saito *J. Phys. Soc. Japan*, vol. **65**, p. 1340, 1996.
- [77] A. Fortunelli and A. Painelli *J. Chem. Phys.*, vol. **106**, p. 8051, 1997.
- [78] J. Wosnitza, G. W. Crabtree, H. H. Wang, K. D. Carlson, M. D. Vashon, and J. M. Williams *Phys. Rev. Lett.*, vol. **67**, p. 263, 1991.
- [79] J. Wosnitza, G. W. Crabtree, H. H. Wang, U. Geiser, J. M. Williams, and K. D. Carlson *Phys. Rev. B*, vol. **45**, p. 3018, 1992.
- [80] J. Wosnitza *Int. J. Mod. Phys. B*, vol. **7**, p. 2707, 1993.
- [81] H. Weiss, M. V. Kartsovnik, W. Biberacher, E. Steep, E. Balthes, A. G. M. Jansen, K. Andres, and N. D. Kushch *Phys. Rev. B*, vol. **59**, p. 12 370, 1999.
- [82] F. A. Meyer, E. Steep, W. Biberacher, P. Christ, A. Lerf, A. G. M. Jansen, W. Joss, P. Wyder, and K. Andres *Europhys. Lett.*, vol. **32**, p. 681, 1995.
- [83] K. D. Carlson, U. Geiser, A. M. Kini, H. H. Wang, L. K. Montgomery, W. K. Kwok, M. A. Beno, J. M. Williams, C. S. Cariss, G. W. Crabtree, M.-H. Whangbo, and M. Evain *Inorg. Chem.*, vol. **27**, p. 965, 1988.
- [84] T. Sugano, G. Saito, and M. Kinoshita *Phys. Rev. B*, vol. **35**, p. 6554, 1987.
- [85] E. L. Venturini, L. J. Azevedo, J. E. Schirber, J. M. Williams, and H. H. Wang *Phys. Rev. B*, vol. **32**, p. 2819, 1985.
- [86] T. Nakamura, T. Nobutoki, T. T. G. Saito, H. Mori, and T. Mori *J. Phys. Soc. Japan*, vol. **63**, p. 4110, 1994.
- [87] J. M. Williams, J. R. Ferraro, R. J. Thorn, K. D. Carlson, U. Geiser, H. H. Wang, A. M. Kini, and M.-H. Whangbo, *Organic Superconductors*. Prentice Hall, Englewood Cliffs, NJ, 1992.
- [88] B. Andracka, J. S. Kim, G. R. Stewart, K. D. Carlson, H. H. Wang, and J. M. Williams *Phys. Rev. B*, vol. **40**, p. 11345, 1989.

- [89] B. Andraka, C. S. Jee, J. S. Kim, G. R. Stewart, K. D. Carlson, H. H. Wang, A. V. S. Crouch, A. M. Kini, and J. M. Williams *Solid State Commun.*, vol. **79**, p. 57, 1991.
- [90] H. Weiss, M. V. Kartsovnik, W. Biberacher, E. Balthes, A. G. M. Jansen, and N. D. Kushch to be published in *Synth. Met.*
- [91] M. V. Kartsovnik unpublished.
- [92] A. Kawamoto, K. Miyagawa, and K. Kanoda *Phys. Rev. B*, vol. **55**, p. 14 140, 1997.
- [93] H. Taniguchi, A. Kawamoto, Y. Nakazawa, and K. Kanoda *Synth. Met.*, vol. **103**, p. 2250, 1999.
- [94] X. Su, F. Zuo, J. Schlueter, A. Kini, and J. Williams *Phys. Rev. B*, vol. **58**, p. R2944, 98.
- [95] T. Doi, K. Oshima, H. Maeda, H. Yamazaki, H. Maruyama, H. Kimura, M. Fujita, H. Mori, S. Tanaka, H. Yamochi, and G. Saito *Physica C*, vol. **185-189**, p. 2671, 1991.
- [96] X. Su, F. Zuo, J. A. Schlueter, M. E. Kelly, and J. M. Williams *Solid State Commun.*, vol. **107**, p. 731, 1998.
- [97] T. F. Stalcup, J. S. Brooks, and R. C. Haddon *Phys. Rev. B*, vol. **60**, p. 9309, 1999.
- [98] L. K. Montgomery, R. M. Vestal, K. P. Starkey, B. W. Fraveland, M. J. Samide, D. G. Peters, C. H. Mielke, and J. D. Thompson *Synth. Met.*, vol. **103**, p. 1878, 1999.
- [99] T. Ishiguro, H. Ito, Y. Yamauchi, E. Omichi, M. Kubota, H. Yamochi, G. Saito, M. V. Kartsovnik, M. A. Tanatar, Y. V. Sushko, and G. Y. Logvenov *Synth. Met.*, vol. **85**, p. 1471, 1997.
- [100] J. Singleton, F. L. Pratt, M. Doporto, J. Caulfield, W. Hayes, I. Deckers, G. Pitsi, F. Herlach, T. J. B. M. Janssen, J. A. A. J. Perenboom, M. Kurmoo, and P. Day *Synth. Met.*, vol. **55-57**, p. 2198, 1993.
- [101] M. V. Kartsovnik private communication.
- [102] M. Schiller, W. Schmidt, E. Balthes, D. Schweitzer, H.-J. Koo, M. H. Whangbo, I. Heinen, T. Klaus, P. Kircher, and W. Strunz *Europhys. Lett.*, vol. **51**, p. 82, 2000.
- [103] G. Visentini, A. Painelli, A. Girlando, and A. Fortunelli *Europhys. Lett.*, vol. **42**, p. 467, 1998.
- [104] K. Kanoda *Physica C*, vol. **282-287**, p. 299, 1997.

- [105] H. Mayaffre, P. Wzietek, C. Lenoir, D. Jérôme, and P. Batail *Europhys. Lett.*, vol. **28**, p. 205, 1994.
- [106] H. Weiss, M. V. Kartsovnik, W. Biberacher, E. Steep, E. Balthes, A. G. M. Jansen, and N. D. Kushch *Synth. Met.*, vol. **103**, p. 1998, 1999.
- [107] M. V. Kartsovnik, V. N. Laukhin, and S. I. Pesotskii *Sov. J. Low Temp. Phys.*, vol. **18**, p. 13, 1992.
- [108] T. Terashima, S. Uji, H. Aoki, M. Tamura, M. Kinoshita, and M. Tokumoto *Solid State Commun.*, vol. **91**, p. 595, 1994.
- [109] E. Ohmichi, H. Ito, T. Ishiguro, G. Saito, and T. Komatsu *Phys. Rev. B*, vol. **57**, p. 7481, 1998.
- [110] B. Z. Narymbetov, N. D. Kushch, L. V. Zorina, S. S. Khasanov, R. P. Shibaeva, T. G. Togonidze, A. E. Kovalev, M. V. Kartsovnik, L. I. Buravov, E. B. Yagubskii, E. Canadell, A. Kobayashi, and H. Kobayashi *Eur. Phys. J. B*, vol. **5**, p. 179, 1998.
- [111] A. B. Pippard, *Magnetoresistance in Metals*. Cambridge University Press, New York, 1989.
- [112] D. Chasseau, J. Gaultier, M. Rahal, L. Ducasse, M. Kurmoo, and P. Day *Synth. Met.*, vol. **41-43**, p. 2039, 1991.
- [113] S. Hill, J. Singleton, F. L. Pratt, M. Doporto, W. Hayes, T. J. B. M. Janssen, J. A. A. J. Perenboom, M. Kurmoo, and P. Day *Synth. Met.*, vol. **55-57**, p. 2566, 1993.
- [114] T. Burgin, T. Miebach, J. C. Huffmann, L. K. Montgomery, J. A. Paradis, C. Rovira, M.-H. Whangbo, S. N. Magonov, S. I. Khan, C. E. Strouse, D. L. Overmyer, and J. E. Schirber *J. Mater. Chem.*, vol. **5**, p. 1659, 1995.
- [115] R. P. Shibaeva, S. S. Khasanov, N. D. Kushch, E. B. Yagubskii, K. Boubekeur, P. Batail, and E. Canadell in *Supramolecular Engineering of Synthetic Metallic Materials: Conductors and Magnets* (J. Veciana, C. Rovira, and D. Amabilino, eds.), vol. **518**, (Dordrecht, Holland), p. 493, NATO ASI Series Kluwer Acad. Publ., Series C, 1998.
- [116] E. Gmelin, A. Simon, W. Brämer, and R. Villar *J. Chem. Phys.*, vol. **76**, p. 6256, 1982.
- [117] T. P. Martin, H.-J. Stolz, G. Ebbinghaus, and A. Simon *J. Chem. Phys.*, vol. **70**, p. 1096, 1979.
- [118] G. Metsch, W. Bauhofer, and A. Simon *Z. Naturforsch.*, vol. **40a**, p. 303, 1985.
- [119] G. Ebbinghaus and A. Simon *J. Chem. Phys.*, vol. **43**, p. 117, 1979.

- [120] M. G. Burt and V. Heine *J. Phys. C*, vol. **11**, p. 961, 1978.
- [121] P. E. Rauch and A. Simon *Angew. Chem. Int. Ed. Engl.*, vol. **31**, p. 1519, 1992.
- [122] G. J. Snyder and A. Simon *Angew. Chem. Int. Ed. Engl.*, vol. **33**, p. 689, 1994.
- [123] G. J. Snyder and A. Simon *Z. Naturforsch. B*, vol. **49B**, p. 189, 1994.
- [124] G. J. Snyder and A. Simon *J. Chem. Soc. Dalton Trans.*, p. 1159, 1994.
- [125] G. J. Snyder and A. Simon *J. Am. Chem. Soc.*, vol. **117**, p. 1996, 1995.
- [126] U. Steinbrenner and A. Simon *Angew. Chem. Int. Ed. Engl.*, vol. **35**, p. 552, 1996.
- [127] A. Simon and U. Steinbrenner *J. Chem. Soc. Faraday Trans.*, vol. **92**, p. 2117, 1996.
- [128] U. Steinbrenner and A. Simon *Z. Kristallogr.*, vol. **212**, p. 428, 1997.
- [129] U. Steinbrenner, P. Adler, W. Hölle, and A. Simon *J. Phys. Chem. Solids*, vol. **59**, p. 1527, 1998.
- [130] H. Weiss, G. V. Vajenine, U. Steinbrenner, A. Simon, E. Balthes, and P. Wyder *Phys. Rev. B*. in press.
- [131] U. Steinbrenner *Thesis, Universität Stuttgart*, 1997.
- [132] O. K. Andersen and O. Jepsen *Phys. Rev. Lett.*, vol. **53**, p. 2571, 1984.
- [133] K. H. Weyrich *Phys. Rev. B*, vol. **37**, p. 10 269, 1988.
- [134] J. Wills unpublished.
- [135] S. Y. Savrasov *Phys. Rev. B*, vol. **54**, p. 16 470, 1996.

Acknowledgments

I am grateful to Prof. Peter Wyder for accepting me as a Ph.D. student at the High Magnetic Field Laboratory in Grenoble and for giving me the opportunity to carry out the present work in a free and pleasant atmosphere.

I would like to gratefully acknowledge the cooperation of Prof. Günter Schatz and Prof. Heinz Dehnen who readily agreed to act as my examiners.

Of all the people who have assisted me in the course of this thesis I am first and foremost indebted to my unofficial supervisors Mark Kartsovník and Werner Biberacher at the Walther-Meißner-Institut in Garching. They did a great deal of work behind the scenes in giving competent advice as experienced experimentalists and experts in the field of organic metals - at all times!

I remain grateful to Prof. Arndt Simon and Grigori Vajenine at the Max-Planck-Institut in Stuttgart for their collaboration and interest in my experimental work, as well as for their great effort in providing a theoretical background.

Eduard Balthes, Eckhard Steep, and Louis Jansen are thanked for general advice, assistance with experimental set-ups, relevant discussions, and comments to the manuscript.

I wish to thank all my other colleagues in the lab, Ph.D. and diploma students, scientists, technicians, secretaries, and colleagues in the workshop for their help and for creating a nice atmosphere.

Credit for this work must of course be shared with those who provided the principal items of the experiments, i.e., high quality samples. Many thanks to Natasha Kushch and Ulrich Steinbrenner for the synthesis of the κ -(BEDT-TTF)₂Cu[N(CN)₂]Br and the NaBa₃N crystals, respectively.

I would like to thank Anja for the past years that would not have been that great and eventful without her.

My parents have always encouraged me and guided me to independence, never trying to limit my aspirations. I am grateful to them for their unfailing support and faith in me over the years.

Lebenslauf

Herbert Dieter Weiß
geboren am 26. August 1971 in München

1978 - 1982	Besuch der Grundschule in München
1982 - 1991	Besuch des Theodolinden-Gymnasiums in München, Abschluß mit dem Abitur
1991 - 1992	Zivildienst, Sanitätsdienst beim Bayerischen Roten Kreuz in München
1992 - 1997	Studium der Technischen Physik an der Technischen Universität München
Frühjahr 1995	10-wöchiges Industriepraktikum bei CORYS in Grenoble, Frankreich
1996 - 1997	Diplomarbeit am Walther-Meißner-Institut für Tieftemperaturforschung, München, angefertigt am Hochfeld-Magnetlabor in Grenoble, Frankreich
1998 - 2000	Promotion am Hochfeld-Magnetlabor in Grenoble, Frankreich